Title
Quantum Simulation of the Bose-Hubbard Model with Ultracold Atoms in Triangular Optical Superlattices

Author
Barter, Thomas Hamish

Publication Date
2018

Peer reviewed|Thesis/dissertation

Quantum Simulation of the Bose-Hubbard Model with Ultracold Atoms in Triangular Optical Superlattices

by

Thomas Hamish Barter

A dissertation submitted in partial satisfaction of the

requirements for the degree of

Doctor of Philosophy

in

Physics

in the

Graduate Division

of the

University of California, Berkeley

Committee in charge:

Professor Dan M. Stamper-Kurn, Chair
Professor Norman Yao
Professor Laura Waller

Fall 2018

Quantum Simulation of the Bose-Hubbard Model with Ultracold Atoms in Triangular Optical Superlattices

Abstract

Quantum Simulation of the Bose-Hubbard Model with Ultracold Atoms in Triangular Optical Superlattices

by

Thomas Hamish Barter

Doctor of Philosophy in Physics

University of California, Berkeley

Professor Dan M. Stamper-Kurn, Chair

Quantum simulation is the study of one quantum mechanical system via analog with another. In this thesis we explore a simple model of interacting bosons on a lattice, known as the Bose-Hubbard model, by experimental investigation of ultracold rubidium atoms in an optical lattice made from laser light. We describe the construction and stabilization of an optical superlattice with threefold symmetry, and its use in studying the Bose-Hubbard model on triangular and trimerized kagome lattices. We study the short range phase coherence of a Mott insulator on the triangular lattice, and develop a scheme to mitigate out-of-equilibrium effects arising from the state preparation. We show the first experimental realization of an optical trimerized kagome lattice for cold atoms, and discuss experiments characterizing this lattice. Finally, we provide evidence for a Mott insulating state with fractional average particle number per site with measurements of the nearest-neighbor phase coherence of strongly interacting atoms in the trimerized kagome lattice.

To my family

Contents

List of Figures

List of Tables

Acknowledgments

The work done in this thesis was by no means done alone . To the many people who set me along this course, supported me along the way and helped me finish, thank you.

To Claire Thomas and Zephy Leung, who fought alongside me in the trenches of E5 for so long, thank you, this would not have been possible without either of you. Thank you to the many people who joined E5 along the way, and the rest of the ultracold group at Berkeley.

I owe particular thanks to my advisor Dan Stamper-Kurn, for taking me on as a graduate student and for supporting me over these many years. Perhaps Dan's greatest contribution is an incredible education in what it means to think and analyze problems as a physicist. Every meeting, and every chat was an opportunity to learn and improve.

To Norm Yao, thank you for the many late night chats about science that were exactly what I came to grad school for. To the many other members of the physics community at Berkeley, from the faculty that have guided me to my fellow students, thank you for making this an incredible environment to learn in.

To all my friends, near or far, thank you for your friendship and companionship over these challenging years.

To my family back home in New Zealand, thank you for your never-ending support while I've been half a world away.

Finally, to my partner Sydney. Your belief in me never faltered and gave me the strength to finish.

Chapter 1

Introduction

1.1 Quantum simulation

> "Nature isn't classical, dammit, and if you want to make a simulation of nature, you'd better make it quantum mechanical and by golly it's a wonderful problem, because it doesn't look so easy." - Richard Feynman, 1981 [19].

This thesis is focused on quantum simulation: the study of an unexplored system, governed by the rules of quantum mechanics, via analog to another quantum mechanical system which we can precisely control and measure. This challenging task, requiring the engineering of systems at the quantum level comes as a resolution to existing problems. Many physical systems studied in laboratories can only be measured in limited ways, leaving us with an incomplete understanding of their physics. However, the classical simulation of quantum systems can be extremely challenging, if not impossible.

To understand the challenge of describing quantum mechanical systems with classical information, we will consider how much information is required just to write down the state of a very general quantum system. As physicists, we describe many systems of interest in terms of well understood elementary units. One of the most powerful of these elementary units is a spin$-\frac{1}{2}$ particles, such as an electron, and so a very general description of a interacting quantum system is that of N interacting spin$-\frac{1}{2}$ particles.

Each of these particles is described as a superposition of two possible states, either spin up or spin down. Thus a general quantum state of N spins can be written as a superposition of all possible up or down configurations.

Combinatorically there are 2^N such configurations of the N spins, and so a classical description requires storing 2^N coefficients. To comprehend the scale of a classical description of a quantum mechanical system, examine how much data is required to store 2^N coefficients describing $N = 30$, 100 and 300 spins, shown in figure 1.1.

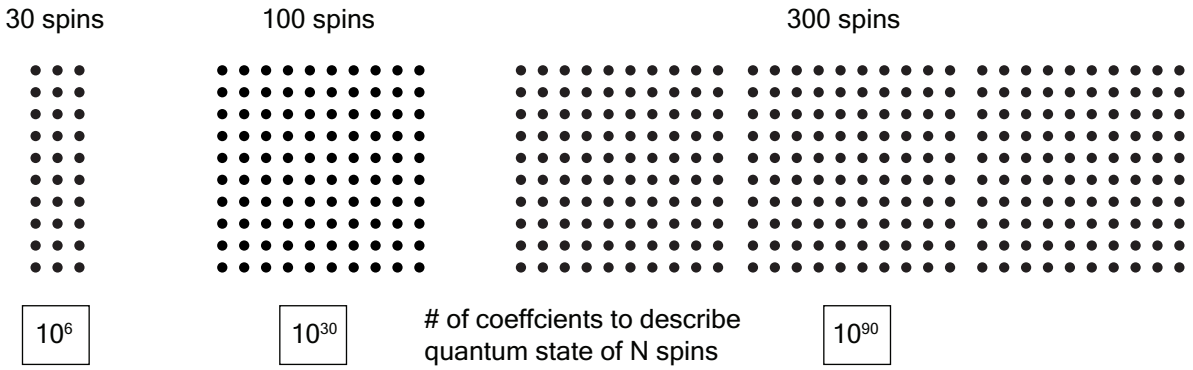

Figure 1.1: Comparison of the number of spins and how many classical numbers are required to describe their quantum state.

For 30 spins, 2^{30} is about a million numbers. Assuming 32 bits per number for floating point precision, storing these coefficients requires 4 GB of memory, a completely reasonable task with today's technology. However, for 100 spins $2^{100} \approx 10^{30}$. At the same precision this requires approximately 10^{30} bytes of data, more than a billion times the estimated worldwide storage capability in 2018 of 663 exabytes [37]. At 300 spins, we require the ability to store 10^{90} numbers, more than 10 billion times the number atoms in the observable universe. Just increasing the size of a quantum system by a factor of 10 transforms a completely feasible classical description into absurdity.

Whilst the idea of building quantum systems to mimic other systems has its roots in Richard Feynman's 1981 lecture, "Simulating physics with computers" [19], only relatively recently has this idea become feasible. Building a simulator requires not only precise control over individual quantum systems, but also over the interactions among the individual systems. Furthermore, these systems must be well isolated from their environment to prevent the loss of fragile quantum information.

We describe a quantum mechanical system of interest by its Hamiltonian, and the two broad classes of quantum simulation, digital and analog, correspond to different ways of representing this Hamiltonian.

In digital quantum simulation, the system is typically mapped onto a number of spin-1/2 particles. The Hamiltonian is then broken up into many small pieces, and represented as a set of elementary operations on these spins. This is simply a different way of saying that digital quantum simulation is a quantum algorithm run on a quantum computer. Digital quantum simulation has the advantage that many different Hamiltonians can be simulated on the same device using different algorithms [23]. However, practical implementation of quantum systems always suffers from errors, which as of 2018 is an unsolved problem. The presence of errors currently limits digital quantum simulation to a system size that can be simulated classically [23].

In analog quantum simulation, we directly engineer the interactions between quantum particles so that their Hamiltonian can be mapped to a system of interest. Whilst errors are

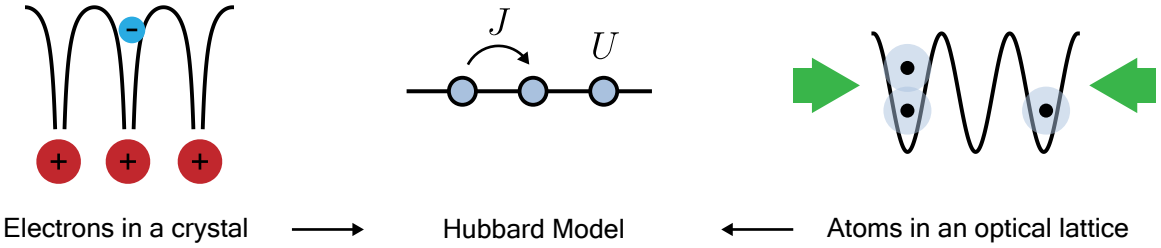

Figure 1.2: The Hubbard model is a simplified model of electrons in a crystal. Ultracold atoms in an optical lattice are a quantum simulator of the Hubbard model.

not so detrimental to analog simulation, this method requires the construction of different devices for different Hamiltonians [23]. In this thesis we will describe an analog quantum simulation, in which a gas of extremely cold atoms subject to standing waves of laser light forms an analog for interacting electrons in a crystal.

1.2 Optical lattices and the Bose-Hubbard model

A simple, but surprisingly rich model of interacting, mobile electrons in a crystal structure is known as the Hubbard model [34]. All of the details of the atoms that form the crystal are abstracted away, leaving only a lattice of sites where the atoms once were. Instead of solving the complex motion of the electrons through the potential formed by the atoms, the Hubbard model simply describes tunneling of the electrons from site-to-site with an energy J. Even the long-range Coulomb potential of the electrons is drastically simplified: electron do not interact with each other unless on the same site, captured by an interaction energy U.

Despite the drastic simplifications made in the Hubbard model, it captures an amazing range of physics. When the interactions are strong relative to the tunneling, this model describes an interaction driven insulator [41]. When there are equal numbers of spin up and down particles, it describes an anti-ferromagnetic state [63]. The Hubbard model is even believed to describe the physics of high temperature superconductors [47].

Having identified the system that we wish to simulate, we explain how ultracold atoms barely 100 nanokelvin above absolute zero can play the role of the electrons, and how standing waves of light create a crystal structure.

Alkali atoms like rubidium, our atom of choice in the lab, have only one valence electron. These atoms thus have a relatively simple electronic structure, and at low density only absorb and emit light at two very specific wavelengths. For rubidium, these are regions of the electromagnetic spectrum 10^{-5} nm wide at 780 nm and 795 nm [62]. Far away from these atomic resonances, light is rarely absorbed by rubidium. However, the quantum mechanical process of virtually absorbing and emitting a photon creates a tiny potential for the atoms,

with a spatial profile proportional to the intensity of the light [31]. This process is very similar to the mechanism behind optical tweezers.

Thus if these atoms are subjected to a standing wave of off-resonant light, made by reflecting a laser beam back upon itself, they experience a periodic potential. However, this potential is incredibly weak. In units of temperature, the depth of this potential is only a few millikelvin. What we mean by stating a potential depth as temperature, is that a rubidium atom can mostly ignore this potential unless it is about as cold as the potential is deep.

To create our quantum simulator, we need atoms not only cold enough that they are held by these weak potentials, but even cold enough that they occupy only a single quantum state in the well formed by each minimum of the periodic potential. Once we cool the atoms to hundreds of nanokelvin, which more than satisfies this condition, they behave much like our model of the electron [38]. The minima of the optical lattice (a term for the periodic laser potential that evokes the analog to a crystal lattice) give us a set of sites that the atoms tunnel between.

Furthermore, the weak Van der Waals forces between alkali atoms take on a simple description when the atoms are cold, and thus move very slowly [13]. Effectively these atoms only interact when their atomic wavefunctions overlap. In the optical lattice, this means interactions only occur on the same site, precisely as with the Hubbard model.

Thus far we have put together two important ingredients of the Hubbard model, tunneling and interactions, but have neglected one: the spin of the particles. Quantum mechanical particles have a form of angular momentum called spin, which determines if they are fermions or boson. Fermions are particles like electrons, which obey the Pauli exclusion principle and do not occupy identical quantum states. Bosons are particles like photons, which do not obey the Pauli exclusion principle, and can have many particles in a single state, like photons occupying a single mode of a laser.

Atoms have a composite spin, made up from the spin of their constituent protons, neutrons and electrons. If the number of neutrons a particular atomic isotope has is odd, such as ^{40}K with 21 neutrons, then that isotope is a fermion and obeys the Pauli exclusion principle. If the number of neutrons is even, as is the case of ^{87}Rb (50 neutrons), or ^{39}K (20 neutrons), the atomic isotope is a boson. These differences are not often clear at high temperature, but cooled to hundreds of nanokelvin, two different isotopes of the same species behave drastically differently.

Cold fermionic atoms behave exactly like electrons, and in this case a cold atom optical lattice quantum simulator really does simulate a system of interacting electrons. Some very interesting phenomena happen when the atoms are bosons. The Hubbard model of bosons is known as the Bose-Hubbard model [38], and describes striking phenomena such as Bose-Einstein condensation and superfluidity [1]. A Bose-Einstein condensate is a macroscopic occupation of a single quantum state, where every atom behaves identically. A weakly interacting Bose-Einstein condensate is a superfluid, which flows without dissipation.

This thesis focuses on the analog quantum simulation of the Bose-Hubbard model. This is not precisely the same model as electrons in a crystal, but is worth simulating nonetheless for two main reasons.

The first reason is that many of the same techniques developed for quantum simulation of the Hubbard model using cold bosonic atoms are equally applicable to cold fermionic atoms. The first optical lattice experiments [30] and many of the subsequent breakthrough advances, such as single site imaging of optical lattices [2] were performed first with bosonic atoms, before application to fermionic atoms [10]. Bosonic systems are often amenable to powerful computational techniques to circumvent the 2^N scaling problem previously discussed [77]. This allows a verification of the techniques used for quantum simulation by bosons before their application to fermions.

But the more important reason to build analog quantum simulators using bosonic atoms is that the Bose-Hubbard model is very interesting in its own right. When the atoms are weakly interacting, they form a superfluid, which not only flows without resistance, but spontaneously breaks the $U(1)$ phase symmetry of the wavefunction. In the strongly interacting limit, the gas forms an insulator with precisely integer numbers of particles per site [30].

In between these two different phases of matter is a quantum phase transition, driven by quantum fluctuations. We will use our quantum simulator of the Bose-Hubbard model to study this phase transition, and these quantum fluctuations over this thesis.

1.3 The triangular optical superlattice

The Bose-Hubbard model has been studied extensively with systems of ultracold atoms in optical lattices [7]. What is unique about the work done in our lab, and presented in this thesis, is the lattice structure we create to study the Bose-Hubbard model. As the potential experienced by the atoms is proportional to the intensity of the light used to make the lattice, different intensity patterns yield different lattice structures. We have built a highly configurable apparatus that creates complex two dimensional optical lattices by interfering three laser beams of one wavelength , and another three beams of a second wavelength, twice the magnitude of the first.

This yields Bose-Hubbard models on a range of lattices, shown in figure 1.3. We can generate familiar lattices such as the triangular or honeycomb lattice, as well as more exotic lattices such as the kagome lattice and its trimerized variant. Throughout this thesis we will explore the Bose-Hubbard model in many of these different geometries, all created by a single versatile quantum simulator.

1.4 This thesis

- In chapter 2 we formally derive the Bose-Hubbard model from a quantum mechanical description of cold bosonic atoms in periodic potentials formed from light. We give a theoretical description of the triangular optical superlattice potential, and show how it arises from two triangular optical lattices, one with twice the spacing of the other.

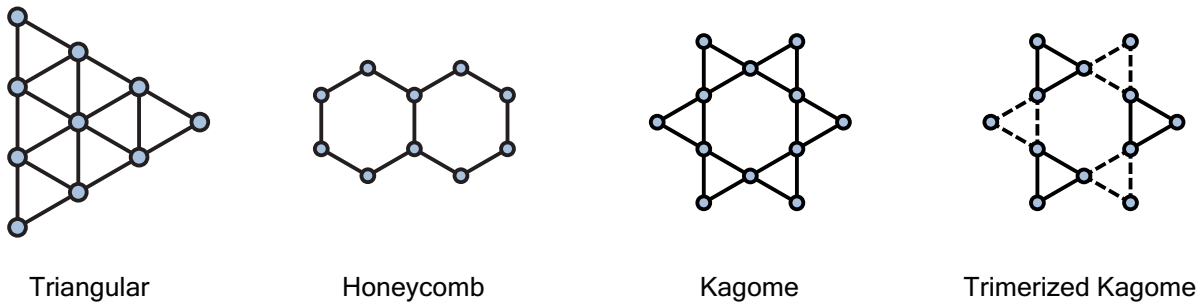

Figure 1.3: The quantum simulation we describe in this thesis can realize the Bose-Hubbard model on the triangular, honeycomb, kagome, trimerized-kagome lattice structures and more.

Finally, we show the superlattice is used to study the Bose-Hubbard model in all of the geometries in figure 1.3 and more.

- In chapter 3 we describe the experimental apparatus and overview the methods we use to produce ultracold gases of ^{87}Rb. We discuss the experimental implementation of the triangular optical superlattice, explore some of its non-ideal properties and explain our methods of aligning, balancing and calibrating our lattices.

- In chapter 4 we describe the electrical and optical feedback system that stabilizes the relative displacement of the two triangular optical lattices. We explain the fundamental mechanisms behind this scheme and compare to existing superlattice schemes. We introduce the optical phase-locked loop used in the stabilization feedback, describe its implementation and examine its performance.

- In chapter 5 we discuss the effects of quantum fluctuations on a Mott insulator in a triangular optical lattice. We demonstrate how to measure the short range phase coherence induced by these correlated fluctuations, and compare theory and experimental results. We discover an inconsistency between experiment and theory, explore its possible causes and attribute it to an out-of-equilibrium effect. We demonstrate a scheme to correct this inconsistency, and show final measurements of the phase coherence of a Mott insulator in a triangular optical lattice.

- In chapter 6 we study a new type of Mott insulating state existing in a trimerized Kagome lattice. Instead of integer filling per site, this fractional Mott insulating state has a fractional filling per site. We measure the short range phase coherence of this state and show how the results provide evidence for this new state. Finally we implement a new technique to demonstrate the asymmetry of this short range phase coherence.

1.5 A history of this experiment

I joined E5, as our experimental apparatus is known, as a rotation student in the spring semester of 2012. Post-doc Gyu-Boong Jo, senior graduate student Jennie Guzman, and junior graduate student Claire Thomas had recently converted the apparatus from a spinor Bose-Einstein condensate (BEC) experiment, to a kagome optical lattice experiment. While they were hard at work studying the superfluid-to-Mott insulator transition, I worked on the side building a new external cavity laser. The superfluid-to-Mott insulator transition experiment turned out to be ill-fated, as inconsistencies led to the data being thrown away.

Over the summer Jennie stepped out of the lab, and I joined the lab full time. Through that summer and the following fall semester the lab was led by Gyu-Boong, who was hunting for a method to prepare cold atoms in the 'flat-band' of the kagome lattice. We tried the lattice shaking technique, and to populate the band in a metastable manner, but to no avail. At the end of the year, Gyu-Boong stepped out of the lab to write faculty applications. That semester began the tenure of Claire and I as co-leaders of the lab. I worked on purchasing a new laser system for cooling potassium and we both struggled with laser problems. We replaced the old repump laser twice, eventually moving towards DFB technology which was extremely stable. At some point in the semester, we lost the ability to make a magneto-optical trap, the first stage of cooling the atoms. After an exhaustive search for the reason behind this, we concluded that the rubidium source in the oven had run out and would need replacing.

Replacing the rubidium source turned out to be a pivotal moment in my PhD. The Viton gate valve between the oven and the ultra-high vacuum (UHV) main chamber failed as we brought the oven to atmospheric pressure with nitrogen. As soon as we opened the oven to replace the rubidium, the main chamber was contaminated by room air and all of the water it carriers. This meant that the main chamber would have to be 'baked', where we raise the entire chamber to over 150° C to pump out all of the water. Unfortunately baking the entire main chamber required stripping all of the optics off, which prompted a major redesign of the lattice and trapping optics.

The road back to a working BEC machine was a long one, punctuated by a number of setbacks. It took us a number of bakeouts to achieve ultra-high vacuum, as our particular design of titanium sublimation pump was prone to breaking filaments. We had to replace the filaments a couple of times, each time requiring we vent the chamber and then bake it out. That summer, during one of these bakeouts, the lab flooded when a contractor in a nearby room triggered a fire sprinkler. Claire's heroics saved the majority of our electronics from getting wet, but the subsequent power shutdown turned off the turbopumps. Shutting down the turbopumps incorrectly may have contaminated the main chamber with oil vapor from the roughing pumps, but we soon achieved UHV, proving this was not the case.

We were then joined by Vincent Klinkhamer from the Jochim group in Heidelberg. That fall we made the bold decision to lift the entire vacuum chamber by 6 inches. 8 or so of us lifted the chamber with only the use of metal cross beams while I raised the height of all the supports. Somehow, this didn't result in a vacuum leak.

We soon recovered the magneto-optical trap, and Claire stepped out of the lab for a few months to re-analyse the superfluid-to-Mott insulator data. I re-optimized the magnetic transport and microwave evaporation, while Vincent designed a set of PCB coils to precisely control the magnetic field environment of the atoms.

Claire rejoined us in 2014 to design and build the 1064 nm optics for optical trapping and one of the optical lattices. We began optically trapping the atoms, and Vincent returned to Heidelberg. We slowly made our way to BEC by implementing a new optical evaporation technique until late in 2014, we tried an absurdly long evaporation and produced our first semi-condensed gas. Not long after, we had a working machine producing reliable pure Bose condensates.

In 2015 we continued rebuilding the optical lattice. I designed and built the 532 nm optics while Claire designed a new intensity stabilization system. We were joined in the lab by a new graduate student Zephy Leung, and another student from Heidelberg, Severin Daiss.

During our efforts to calibrate our new 1064 nm honeycomb lattice we noticed that a strange time-of-flight pattern. Briefly pulsing on this lattice caused threefold symmetric, not sixfold symmetric diffraction. This was an interesting observation, as it looked similar to diffraction patterns seen in another group using honeycomb lattices claiming to see a 'twisted superfluid state'. We soon realized our threefold symmetry was due to a vector stark shift from the in-plane polarized 1064 nm lattice. I took the data for this paper, and Claire wrote the paper up, finally being published in PRA [68].

In the fall of 2015 I began my major technical contribution to the apparatus: designing and building the system that stabilizes the relative displacement of the 532 nm and 1064 nm triangular lattices. This is discussed in chapter 4. This system required a lot of learning, as we moved from a piezo based path length feedback to an optical phase-locked loop design. Our initial design was complicated, with phase-locked loops on both radio-frequency and optical paths. We abandoned this design as it generated a lot of noise, and following a useful comment by Daniel Grief, then at Harvard, we moved to a function-generated based voltage controlled oscillator design. We were soon joined by Masayuki Okano from the Takahashi Lab in Kyoto

When we tested the feedback system for the first time with the atoms in early 2016, it worked. We thus returned to the superfluid-to-Mott insulator transition in the kagome lattice, and were joined by Luca Bayha from the Jochim group. We took the superfluid-to-Mott insulator data, and analyzed the data. We found that a mean-field theory prediction held, concerning a comparison of the superfluid-to-Mott insulator transition in the triangular and kagome lattice. Claire stepped out of the lab for the last time to write up this paper, and her thesis, bringing our long tenure as co-leaders of the lab to a close. This work was published in PRL [67].

In early 2017, we sat down for a planning meeting to discuss new directions for the experiment. I took this opportunity to calculate all of the different configurations of our optical superlattice, a project that had been on my mind for some time and is shown in chapter 2. We discovered a combination of polarizations and displacement that produce a

bond modulated version of the kagome lattice known as a trimerized kagome lattice. This lattice had been discussed in the literature but never realized, with one proposal suggesting the formation of a Mott insulator in this lattice with fraction particle number per site. We thus created this lattice in the lab.

We soon discovered than in our implementation of the trimerized kagome the energies of the sites were linearly sensitive to the relative displacement of the 532 nm and 1064 nm lattice. We thus had to substantially improve our displacement stabilization system, and come up with new techniques to improve the collinearity of the 532 nm and 1064 nm beams. We created this lattice, started studying the fractional Mott insulator, and began collaborating with a new faculty member Norman Yao, and Maxwell Bloch, who was working at a nearby quantum start up and considering graduate school.

In early 2018 we discovered a problem. We were studying the fractional Mott insulator via its short range phase coherence, and contrasting it to the same measurement in a regular Mott insulator in a triangular lattice. The measured coherence of the Mott insulator in the triangular was too large, and comparison to simple theory suggested a filling of 6 atoms per site in the lattice, much more than our expected value of 1 on average.

We went through our procedures and analysis with a fine-toothed comb and found no significant problems. We measured the number of atoms per site, and found it was only about 1. Eventually we realized that loading the lattice depth increased the interaction energy, making the gas want to expand. Something was preventing this gas expanding, and so the gas was out of equilibrium. We solved this by simplifying our potentials, building a new beam path and control system to keep the gas in equilibrium, and our results started to make sense. We went back to the trimerized kagome lattice, and Zephy and I took final data for this work. I now leave the experiment in Zephy's extremely capable hands, and I'm sure we will hear great things from him in the future.

Chapter 2

Theory

2.1 Derivation of the Bose-Hubbard model

In the introduction we explained how cold bosonic atoms in an optical lattice act as a quantum simulator for the Bose-Hubbard model. In this chapter, we explain this abstraction in greater detail, starting with a description of cold bosonic atoms and their interactions. We introduce a simple optical lattice potential, and show that under certain assumptions, the description of cold atoms in this potential simplifies to the Bose-Hubbard model. Finally, we will explore the more complex potentials studied in this thesis.

Cold bosonic atoms

We describe cold bosonic ^{87}Rb atoms by a spinless quantum field operator $\Psi(\boldsymbol{r})$ with bosonic commutation relations $[\Psi(\boldsymbol{r}), \Psi^\dagger(\boldsymbol{r}')] = \delta(\boldsymbol{r} - \boldsymbol{r}')$. The many-body Hamiltonian describing an interacting system of bosonic atoms is given by [12]

$$\begin{aligned} H = &\int d\boldsymbol{r}\, \Psi^\dagger(\boldsymbol{r}) \left(-\frac{\hbar^2}{2m_{Rb}} \nabla^2 + V(\boldsymbol{r}) \right) \Psi(\boldsymbol{r}) \\ &+ \frac{1}{2} \int d\boldsymbol{r} \int d\boldsymbol{r}'\, \Psi^\dagger(\boldsymbol{r}) \Psi^\dagger(\boldsymbol{r}') U(\boldsymbol{r} - \boldsymbol{r}') \Psi(\boldsymbol{r}') \Psi(\boldsymbol{r}), \end{aligned} \tag{2.1}$$

where m_{Rb} is the mass of a ^{87}Rb atom, $V(\boldsymbol{r})$ describes an external potential, and $U(\boldsymbol{r} - \boldsymbol{r}')$ the interparticle interaction potential. In the partial-wave formulation of interparticle scattering, an incoming particle scatters into outgoing spherical waves of angular momentum l [13]. For low energy collisions between cold ^{87}Rb atoms, which primarily interact via a $U(\boldsymbol{r}) \propto \boldsymbol{r}^{-6}$ van der Waals potential, only the s-wave ($l = 0$) partial waves contribute [13]. For even lower energy collisions, the collision process is independent of the incoming energy. Thus the interaction potential can be replaced by a contact interaction given by

$$U(\boldsymbol{r} - \boldsymbol{r}') = g\delta(\boldsymbol{r} - \boldsymbol{r}') \tag{2.2}$$

where $g = 4\pi\hbar^2 a_s/m_{Rb}$, and a_s is the s-wave scattering length [12]. The Bose-Einstein condensates that we produce in the lab are typically cold enough (< 200 nK) that their kinetic energy satisfies the requirement for this simple interaction when weakly confined [76]. When strongly confined however, such as in an optical lattice, the atoms have substantially more kinetic energy than that of a free particle at the same temperature, and as such care has to be taken when considering their scattering properties.

The optical lattice

To understand how a standing wave of light creates a so-called optical lattice for alkali atoms such as ^{87}Rb, we treat each atom as a simple two level system, with a single ground state and excited state separated by energy $\hbar\omega_0$. This two level atom interacts with dipole radiation of frequency ω. When the detuning $\Delta = \omega_0 - \omega$ is much larger than the natural linewidth of the transition Γ, excitation to the excited state can be neglected, and the light simply causes a shift in the ground state energy proportional to the intensity $I(\boldsymbol{r})$ [31]:

$$\Delta E(\boldsymbol{r}) = V(\boldsymbol{r}) = \frac{3\pi c^2}{2\omega_0^3}\frac{\Gamma}{\Delta} I(\boldsymbol{r}). \tag{2.3}$$

We interpret this energy shift $\Delta E(\boldsymbol{r})$ as a spatially varying potential $V(\boldsymbol{r})$ for the atoms, the sign of which depends on the detuning Δ. Thus if we can create a spatially varying intensity $I(\boldsymbol{r})$ in the lab with far detuned light, we will realize a spatially varying potential $V(\boldsymbol{r})$.

We use the relationship between intensity and atomic potential to create the optical lattice. We first consider a simple one dimensional optical lattice, formed by a monochromatic plane-wave laser beam reflected back upon itself. The spatially varying intensity is given by

$$I(\boldsymbol{r}) = I_0 |e^{i\boldsymbol{k}\cdot\boldsymbol{r}} + e^{-i\boldsymbol{k}\cdot\boldsymbol{r}}|^2 = 2I_0\left(1 + \cos(2\boldsymbol{k}\cdot\boldsymbol{r})\right) \tag{2.4}$$

where $\boldsymbol{k}$ is the wavevector of the incoming beam, and I_0 the intensity. Using the relationship between intensity and potential (equation 2.3), we find the potential

$$V(\boldsymbol{r}) = \frac{3\pi c^2}{\omega_0^3}\frac{\Gamma}{\Delta} I_0\left(1 + \cos(2\boldsymbol{k}\cdot\boldsymbol{r})\right) = \tfrac{1}{2} V_0\left(1 + \cos(2\boldsymbol{k}\cdot\boldsymbol{r})\right) \tag{2.5}$$

where V_0 is defined as the peak-to-peak lattice depth.

Wannier functions

To transform the problem of many interacting atoms in a periodic potential to the Bose-Hubbard model, we first consider a single particle and exploit the translational symmetry of the periodic potential. The wavefunction $\phi_{\boldsymbol{q}}^n(\boldsymbol{r})$ of a single particle in the periodic optical lattice potential $V(\boldsymbol{r})$ is described by the time-independent Schrödinger equation:

$$\left(-\frac{\hbar^2}{2m_{Rb}}\nabla^2 + V(\boldsymbol{r})\right)\phi_{\boldsymbol{q}}^n(\boldsymbol{r}) = E_{\boldsymbol{q}}^n \phi_{\boldsymbol{q}}^n(\boldsymbol{r}), \tag{2.6}$$

where $\boldsymbol{q}$ is known as the quasimomentum [28]. The eigenenergies of this equation $E^n_{\boldsymbol{q}}$ are separated into continuous bands, where n is the band index. The collection of energies $E^n_{\boldsymbol{q}}$ for all n and q is known as the band structure. Bloch's theorem tells us that the wavefunction of a particle in a periodic potential is also periodic, and takes the form [28]

$$\phi^n_{\boldsymbol{q}}(\boldsymbol{r}) = e^{i\boldsymbol{q}\cdot\boldsymbol{r}} u^n_{\boldsymbol{q}}(\boldsymbol{r}). \tag{2.7}$$

Expressing the potential $V(\boldsymbol{r})$ and these functions $u^n_{\boldsymbol{q}}(\boldsymbol{r})$ as a Fourier series in $e^{i2\boldsymbol{k}\cdot\boldsymbol{r}}$ allows us to solve the Schrödinger equation for the band structure $E^n_{\boldsymbol{q}}$. An example of this band structure calculation in 1D is given in [28], and in 2D in Claire Thomas's thesis for the case of the triangular, honeycomb and kagome optical lattices [66]. Here we will focus on using the periodic wavefunctions $\phi^n_{\boldsymbol{q}}(\boldsymbol{r})$ to construct a localized basis for the atoms in our many-body Hamiltonian equation 2.1. The Wannier functions are a set of maximally localized wavefunctions [75], defined as:

$$w_n(\boldsymbol{r}) = \frac{1}{\sqrt{L}} \sum_q e^{-i\boldsymbol{q}\cdot\boldsymbol{r}} \phi^n_{\boldsymbol{q}}(\boldsymbol{r}). \tag{2.8}$$

The Wannier function can be approximated by the eigenfunctions of the harmonic oscillator Hamiltonian, obtained by expanding the potential around the minima of the optical lattice. These eigenfunctions provide a good intuition for the Wannier functions $w_n(\boldsymbol{r})$; for example, the lowest band Wannier function is approximately the Gaussian ground harmonic oscillator eigenfunction. This is a well localized function, that becomes further localized as the curvature at the lattice minima increases. Caution should be used in overlap calculations using this approximation, as the harmonic oscillator eigenfunctions overestimate the long range tails of the Wannier functions [28].

The Bose-Hubbard model

The Bose-Hubbard model will be described by an approximately Gaussian lowest band Wannier function at each site of the optical lattice [38]. To show this, we express the bosonic field operator $\Psi(\boldsymbol{r})$ in terms of the Wannier functions,

$$\Psi(\boldsymbol{r}) = \sum_{i,n} w_n(\boldsymbol{r} - \boldsymbol{r}_i) b_{n,i} \tag{2.9}$$

where $b_{n,i}$ annihilates a particle in the nth-band Wannier function at site i. We obtain the Bose-Hubbard model with the assumptions of low energy and strong localization [11].

Ground-band approximation

In the first of these approximations, we assume only the ground band is occupied, and thus we ignore all of the higher band Wannier functions. The bosonic field operator is thus

$$\Psi(\boldsymbol{r}) = \sum_i w_0(\boldsymbol{r} - \boldsymbol{r}_i) b_i. \tag{2.10}$$

This assumption is approximately equivalent to assuming only the lowest harmonic oscillator state at each minimum is occupied. We are justified in making the ground-band approximation when the temperature of the system, and the expectation value of the interaction term of equation 2.1, is smaller than the gap between the ground band and first excited band [11].

Tight-binding approximation

Having made the ground band approximation, the first term of the many-body Hamiltonian of equation 2.1 is given by,

$$H_1 = \sum_{i,j} \int d\boldsymbol{r}\, w_0^*(\boldsymbol{r} - \boldsymbol{r}_i) \left(-\frac{\hbar^2}{2m}\nabla^2 + V(\boldsymbol{r}) \right) w_0(\boldsymbol{r} - \boldsymbol{r}_j)\, b_i^\dagger b_j. \tag{2.11}$$

Given the localized nature of the Wannier functions, we rearrange this equation as a series of terms corresponding to tunneling between sites at increasing distances m:

$$H_1 = -\sum_i J_0 b_i^\dagger b_i - \sum_{i,j=i\pm1} J_1 b_i^\dagger b_j - \sum_{i,j=i\pm2} J_2 b_i^\dagger b_j - \sum_{i,j=i\pm3} J_3 b_i^\dagger b_j \ldots \tag{2.12}$$

where the tunneling energies J_m are given by

$$J_m = \int d\boldsymbol{r}\, w_0^*(\boldsymbol{r}) \left(-\frac{\hbar^2}{2m}\nabla^2 + V(\boldsymbol{r}) \right) w_0(\boldsymbol{r} - \boldsymbol{r}_m). \tag{2.13}$$

We typically treat the first term of the expansion in H_1 as an offset and ignore it, unless it is slowly varying over the optical lattice, in which case we treat it in section 2.1. As the lattice depth increases, the Wannier functions $w_0(\boldsymbol{r})$ are increasingly localized on a single site, and the tunneling elements J_m diminish rapidly for larger m. When the lattice depth is sufficiently large to neglect all of the terms except J_1, H_1 takes the form of the of the first term of the Bose-Hubbard Hamiltonian,

$$H_1 = -J \sum_{\langle i,j \rangle} b_i^\dagger b_j \tag{2.14}$$

where we have written $J = J_1$, and the sum is over nearest-neighbor lattice sites.

Hubbard interaction approximation

Under the ground-band approximation, the second term of the many-body Hamiltonian equation 2.1 is given by,

$$H_2 = \tfrac{1}{2} U_{ijkl} \sum_{i,j,k,l} b_i^\dagger b_j^\dagger b_k b_l \tag{2.15}$$

where the interaction energies U_{ijkl} are given by

$$U_{ijkl} = g \int d\boldsymbol{r}\, w_0^*(\boldsymbol{r} - \boldsymbol{r}_i) w_0^*(\boldsymbol{r} - \boldsymbol{r}_j) w_0^*(\boldsymbol{r} - \boldsymbol{r}_k) w_0(\boldsymbol{r} - \boldsymbol{r}_l). \tag{2.16}$$

Under the assumption that the Wannier functions are strongly localized, the sum in H_2 is dominated by terms of the form U_{iiii}, where all Wannier functions are from the same site. Dropping all other terms, and identifying $U_{iiii} = U$ yields the second term of the Hubbard model:

$$H_2 = \tfrac{1}{2} U \sum_i b_i^\dagger b_i^\dagger b_i b_i = \tfrac{1}{2} U \sum_i n_i(n_i + 1) \tag{2.17}$$

where $n_i = b_i^\dagger b_i$ is the number operator.

Validity of the Bose-Hubbard model

In practice we numerically calculate all of the terms J_m and H_{ijkl} up to some order for a specific lattice, and choose a minimum lattice depth such that we are justified in the tight-binding and Hubbard interaction approximations. In our group these calculations are performed using the MATLAB package "Wannier states for optical lattices", produced by the Jaksch group at Oxford [40].

These calculations are shown for the triangular, honeycomb and kagome optical lattices in section 2.6.2 of Claire Thomas's thesis [66], and for the trimerized kagome lattice in chapter 6.

Harmonic trapping

One key difference between ultracold atoms in optical lattices and the ideal Bose-Hubbard model is the presence of an overall trapping potential $V_{ext}(\boldsymbol{r})$. The potential is required to confine the atoms, and in the case of this experiment, takes the harmonic form

$$V_{ext}(\boldsymbol{r}) = \tfrac{1}{2} m\omega_x^2 \boldsymbol{x}^2 + \tfrac{1}{2} m\omega_y^2 \boldsymbol{y}^2 + \tfrac{1}{2} m\omega_z^2 \boldsymbol{z}^2 \tag{2.18}$$

where ω_x, ω_y and ω_z are the trap frequencies in the x, y and z directions. We take this spatially varying potential into account by working in the grand canonical ensemble with a spatially varying chemical potential,

$$\mu(\boldsymbol{r}) = \mu_0 - V_{ext}(\boldsymbol{r}), \tag{2.19}$$

where μ_0 is the chemical potential in the center of the trap. The Bose-Hubbard model with a spatially varying chemical potential is less general than the original Bose-Hubbard model, so we make the local density approximation to recover the generality. In this approximation, we assume the state of the system at any given point in space is the same as that of an infinite system with the same chemical potential [73]. This is only a reasonable approximation

if the chemical potential is varying sufficiently slowly in space relative to the sinusoidal optical lattice potential. Thus we recover the generality of the Bose-Hubbard model, but are constrained to interrogate this model across a range of chemical potentials at once. Th external confinement potential will play an important role in chapter 5.

Thomas-Fermi profile

The spatially varying chemical potential $\mu(\boldsymbol{r})$ leads to a spatially dependent density. When the gas is weakly interacting and the chemical potential is negligible, the density of the gas $n(\boldsymbol{r})$ is described by the famous Thomas-Fermi profile:

$$n(\boldsymbol{r}) = n_0 \left(1 - \left(\frac{\boldsymbol{x}}{R_{TF,x}}\right)^2 + \left(\frac{\boldsymbol{y}}{R_{TF,y}}\right)^2 + \left(\frac{\boldsymbol{z}}{R_{TF,z}}\right)^2\right), \tag{2.20}$$

where $R_{TF,i} = \sqrt{\frac{2\mu_0}{m\omega_i^2}}$ is the Thomas-Fermi radius in dimension i where the density goes to zero, and the central density $n_0 = \mu_0/U$. The central chemical potential μ_0 is calculated from the constraint that the total number of atoms N is the integral of the density $n(\boldsymbol{r})$ over all space: $N = \int d^3\boldsymbol{r}\, n(\boldsymbol{r})$. For a harmonically trapped superfluid in three dimensions in an optical lattice, the central chemical potential is

$$\mu_0 = m_{Rb}^{3/5} \left(\frac{15}{16\pi\sqrt{2}} V_{cell} NU\right)^{2/5} \bar{\omega}^{6/5}, \tag{2.21}$$

where V_{cell} is the volume of the unit cell of the lattice, and $\bar{\omega} = (\omega_x\omega_y\omega_z)^{1/3}$.

2.2 Triangular lattice

The rest of this chapter will be focused on the specific optical lattice structures discussed in this thesis. We will introduce the triangular optical lattice, formed by the interference of three plane waves. We will then show how two triangular optical lattices, one formed from 532 nm light and the other 1064 nm light, create an optical superlattice. Finally we will explore the many configurations of this superlattice.

We consider the interference of three plane-wave, monochromatic laser beams of wavelength λ at 120° to each other in a single plane. These beams, labeled beam 1, 2 and 3, have the respective wavevectors:

$$\boldsymbol{k}_1 = k \begin{pmatrix} \frac{\sqrt{3}}{2} \\ -\frac{1}{2} \\ 0 \end{pmatrix} \qquad \boldsymbol{k}_2 = k \begin{pmatrix} 0 \\ 1 \\ 0 \end{pmatrix} \qquad \boldsymbol{k}_3 = k \begin{pmatrix} -\frac{\sqrt{3}}{2} \\ -\frac{1}{2} \\ 0 \end{pmatrix} \tag{2.22}$$

We consider two cases: one when the polarizations of these three beams lie in-plane, with polarization vectors given by

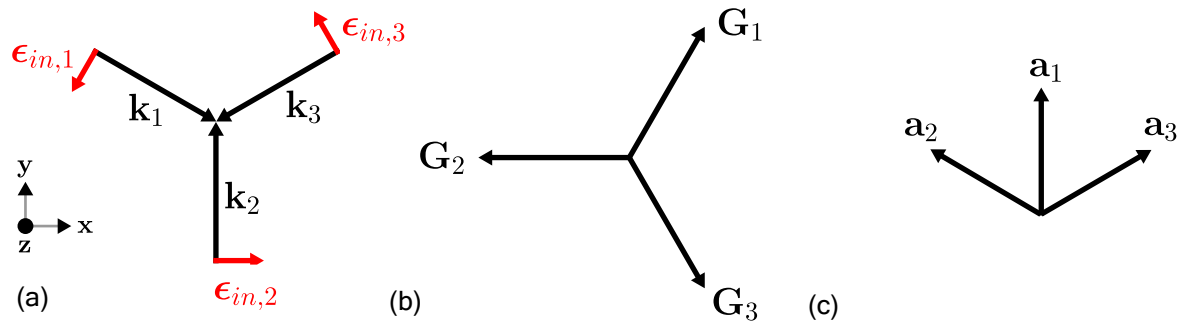

Figure 2.1: Definition of vectors used in this thesis. (a) Wavevectors and polarization vectors of the three interfering laser beams. (b) Reciprocal lattice vectors defined from the wavevectors. (c) Lattice translation vectors.

$$\boldsymbol{\epsilon}_{in,1} = \begin{pmatrix} -\frac{1}{2} \\ \frac{\sqrt{3}}{2} \\ 0 \end{pmatrix} \qquad \boldsymbol{\epsilon}_{in,2} = \begin{pmatrix} 1 \\ 0 \\ 0 \end{pmatrix} \qquad \boldsymbol{\epsilon}_{in,3} = \begin{pmatrix} -\frac{1}{2} \\ \frac{\sqrt{3}}{2} \\ 0 \end{pmatrix} \tag{2.23}$$

and the second with the polarization is out-of-plane,

$$\boldsymbol{\epsilon}_{out,1} = \boldsymbol{\epsilon}_{out,2} = \boldsymbol{\epsilon}_{out,3} = \begin{pmatrix} 0 \\ 0 \\ 1 \end{pmatrix}. \tag{2.24}$$

The wavevectors and in-plane polarization vectors are shown in figure 2.1(a). We will show how these two different polarizations yield two different potentials for cold atoms. Light far detuned from an atomic resonance creates a potential for alkali atoms proportional to the intensity of the light. The spatially varying intensity that results from the interference of these three beams can be written as

$$I(\boldsymbol{r}) \propto \left| \sum_{i=1}^{3} E_i e^{i\boldsymbol{k}_i \cdot \boldsymbol{r} + \phi_i} \boldsymbol{\epsilon}_i \right|^2, \tag{2.25}$$

where E_i is the electric field strength of beam i and ϕ_i the phase. Let us assume that the electric field strengths of the three beams are all equal, and all of the phases are set to zero. The potentials formed by the in-plane polarized and out-of-plane polarized beams can be written in terms of the reciprocal lattice vectors, $\boldsymbol{G}_1$ and $\boldsymbol{G}_2$ and the conveniently defined vector $\boldsymbol{G}_3 = -\boldsymbol{G}_1 - \boldsymbol{G}_2$:

$$\boldsymbol{G}_1 = \boldsymbol{k}_2 - \boldsymbol{k}_3 \qquad \boldsymbol{G}_2 = \boldsymbol{k}_3 - \boldsymbol{k}_1 \qquad \boldsymbol{G}_3 = \boldsymbol{k}_1 - \boldsymbol{k}_2. \tag{2.26}$$

The potential corresponding to in-plane polarization is given by,

$$V_{in}(\boldsymbol{r}) = \tfrac{2}{9}V_{in,0}\left(3 - \cos(\boldsymbol{G}_1 \cdot \boldsymbol{r}) - \cos(\boldsymbol{G}_2 \cdot \boldsymbol{r}) - \cos(\boldsymbol{G}_3 \cdot \boldsymbol{r})\right), \tag{2.27}$$

where $V_{in,0}$ is the peak-to-peak lattice depth, the sign of which depends on the detuning of the laser wavelength λ from atomic resonance. The potential corresponding to out-of-plane polarization is given by

$$V_{out}(\boldsymbol{r}) = \tfrac{1}{9}V_{out,0}\left(3 + 2\cos(\boldsymbol{G}_1 \cdot \boldsymbol{r}) + 2\cos(\boldsymbol{G}_2 \cdot \boldsymbol{r}) + 2\cos(\boldsymbol{G}_3 \cdot \boldsymbol{r})\right), \tag{2.28}$$

where again $V_{out,0}$ is the peak-to-peak lattice depth. In this thesis, triangular optical lattices will be formed from both 532 nm and 1064 nm light, blue detuned and red detuned respectively from the D2 atomic resonance of ^{87}Rb at 780 nm [62]. The spatially vary components of equations 2.27 and 2.28 can be combined into a general statement of the potential (equation 2.29) where the sign of the the peak-to-peak lattice depth V_0 depends on the detuning and polarization as shown in table 2.1:

$$V(\boldsymbol{r}) = \frac{2}{9}V_0\left[\cos(\boldsymbol{G}_1 \cdot \boldsymbol{r}) + \cos(\boldsymbol{G}_2 \cdot \boldsymbol{r}) + \cos(\boldsymbol{G}_3 \cdot \boldsymbol{r})\right] \tag{2.29}$$

Wavelength	Polarization in-plane	Polarization out-of plane
532 nm	$V_0 < 0$	$V_0 > 0$
1064 nm	$V_0 > 0$	$V_0 < 0$

Table 2.1: Table of the sign of the coefficient V_0 in equation 2.29.

A comparison of in-plane and out-of-plane polarized potentials for $\lambda = 532$ nm is shown in figure 2.2. For in-plane polarized light, the 532 nm potential forms a triangular lattice of potential minima, whereas for out-of-plane polarized light, it forms a honeycomb lattice of potential minima.

The in-plane and out-of-plane polarized potentials formed by $\lambda = 1064$ nm are shown in figure 2.3. Opposite to the case of 532 nm light, for 1064 nm light the in-plane polarized light forms a honeycomb lattice of potential minima, whilst the out-of-plane polarization forms a triangular lattice of potential minima.

With these lattices of minima, we are able to define a lattice spacing $a = \frac{2}{3}\lambda$, the lattice vectors $\boldsymbol{a}_1$ and $\boldsymbol{a}_2$, as well as the convenient-to-define vector $\boldsymbol{a}_3$:

$$\boldsymbol{a}_1 = a\begin{pmatrix} 0 \\ 1 \end{pmatrix} \qquad \boldsymbol{a}_2 = a\begin{pmatrix} -\sqrt{3}/2 \\ 1/2 \end{pmatrix} \qquad \boldsymbol{a}_3 = a\begin{pmatrix} \sqrt{3}/2 \\ 1/2 \end{pmatrix} \tag{2.30}$$

These lattice vectors translate between minima in the triangular lattices. The honeycomb lattices have two sets of inequivalent minima, and the same lattice vectors translate between

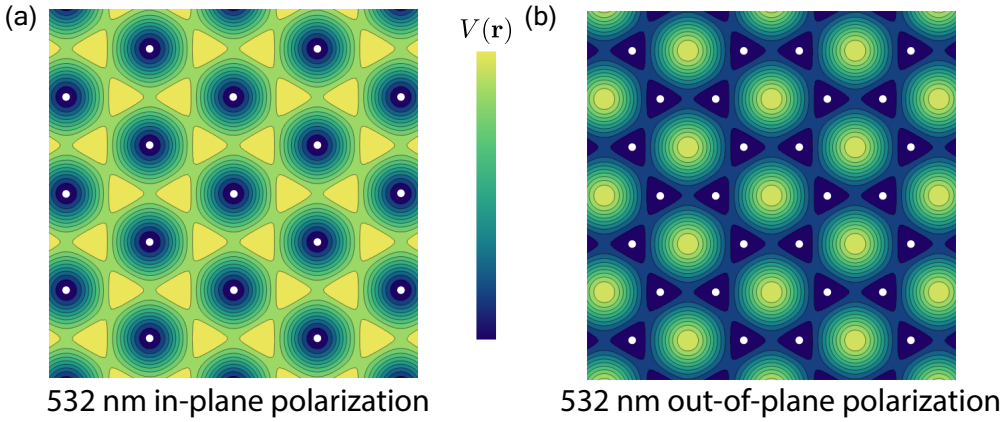

Figure 2.2: The in-plane polarized and out-of-plane polarized 532 nm potentials. White dots mark the positions of the minima

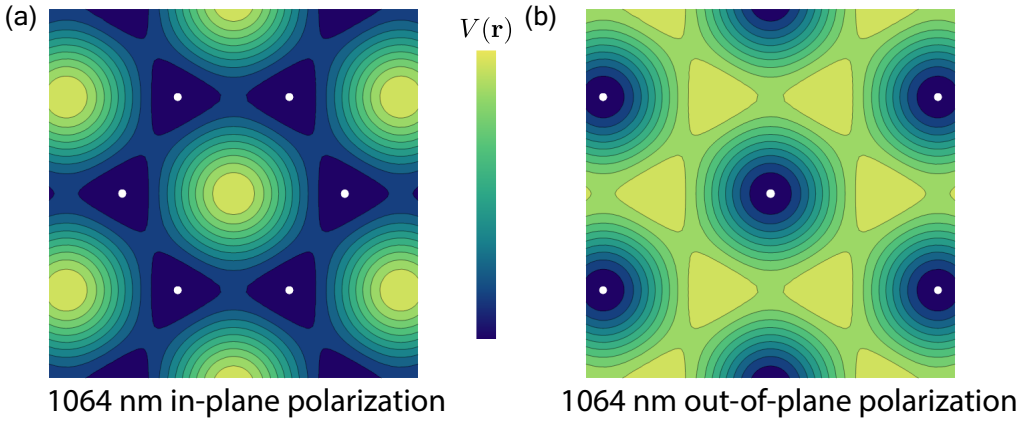

Figure 2.3: The in-plane polarized and out-of-plane polarized 1064 nm potentials. White dots mark the positions of the minima.

these sets. The lattice spacing a allows us to define the recoil energy E_r, a characteristic energy scale given by

$$E_r = \frac{\hbar^2}{2m_{Rb}} \left(\frac{\pi}{a}\right)^2, \tag{2.31}$$

where m_{Rb} is the mass of ^{87}Rb. These lattice spacings and recoil energies are summarized in table 2.2.

Wavelength	Lattice Spacing a	E_r/h
532 nm	355 nm	4.5 kHz
1064 nm	710 nm	1.1 kHz

Table 2.2: Lattice spacing, and recoil energy E_r for 532 nm and 1064 nm triangular lattices.

2.3 Triangular optical superlattice

Now we turn to the combination of the 532 nm and 1064 nm lattices. We no longer assume the phases ϕ_i are zero for the 1064 nm lattice; the 1064 nm lattice can be displaced from the origin by $\boldsymbol{\delta}$ as $V(\boldsymbol{r}-\boldsymbol{\delta})$. The relative displacement of the two triangular optical lattices is an important topic of this thesis. We will discuss the consequences of this displacement momentarily, and later we devote an entire chapter to its control and stabilization.

There are an infinite number of different configurations of this optical superlattice. We have the choice of in-plane or out-of-plane polarization for each of the 532 nm and 1064 nm lattices, and a continuous choice of displacement $\boldsymbol{\delta}$. We limit our choices of the relative displacement to $\boldsymbol{\delta} = 0$, or $\boldsymbol{\delta} = a\left(\frac{1}{2\sqrt{3}}, 0\right)$, as both of these choices yield optical lattices with threefold symmetry. In this section we plot the 8 different potentials that arise from the different combinations of the polarization and displacement, examine the structure of their local minima, and comment on the realized lattice structures. All of the potentials are plotted as

$$V(\boldsymbol{r}) = V_{532}(\boldsymbol{r}) + 0.5V_{1064}(\boldsymbol{r}-\boldsymbol{\delta}) \tag{2.32}$$

where $V_{532}(\boldsymbol{r})$ and $V_{1064}(\boldsymbol{r})$ are defined in terms of the reciprocal lattice vectors $\boldsymbol{G}_i$ for $\lambda = 1064$ nm:

$$V_{532}(\boldsymbol{r}) = \begin{cases} \frac{2}{9}|V_{532}|\left(3 - \cos(2\boldsymbol{G}_1\cdot\boldsymbol{r}) - \cos(2\boldsymbol{G}_2\cdot\boldsymbol{r}) - \cos(2\boldsymbol{G}_3\cdot\boldsymbol{r})\right) & \epsilon \text{ in-plane} \\ \frac{1}{9}|V_{532}|\left(3 + 2\cos(2\boldsymbol{G}_1\cdot\boldsymbol{r}) + 2\cos(2\boldsymbol{G}_2\cdot\boldsymbol{r}) + 2\cos(2\boldsymbol{G}_3\cdot\boldsymbol{r})\right) & \epsilon \text{ out-of-plane} \end{cases} \tag{2.33}$$

$$V_{1064}(\boldsymbol{r}) = \begin{cases} -\frac{2}{9}|V_{1064}|\left(3 - \cos(2\boldsymbol{G}_1\cdot\boldsymbol{r}) - \cos(2\boldsymbol{G}_2\cdot\boldsymbol{r}) - \cos(2\boldsymbol{G}_3\cdot\boldsymbol{r})\right) & \epsilon \text{ in-plane} \\ -\frac{1}{9}|V_{1064}|\left(3 + 2\cos(2\boldsymbol{G}_1\cdot\boldsymbol{r}) + 2\cos(2\boldsymbol{G}_2\cdot\boldsymbol{r}) + 2\cos(2\boldsymbol{G}_3\cdot\boldsymbol{r})\right) & \epsilon \text{ out-of-plane.} \end{cases} \tag{2.34}$$

and V_{532} and V_{1064} are peak-to-peak lattice depths set to one. In all of the upcoming figures we plot the potential in part (a), identifying the position of the local minima with white dots. In part (b) we plot only the local minima, with a color indication the value of the potential $V(\boldsymbol{r})$ at a given local minima.

532 nm in-plane polarization

The 532 nm in-plane polarized lattice forms a triangular lattice of minima, with a potential barrier of $\frac{8}{9}V_{532}$ between the sites. With the prefactor of 0.5 in front of the 1064 nm lattice all of the superlattices with in-plane polarization are just modifications of a triangular lattice, with energy offsets and different potential barriers.

1064 nm in-plane polarization, $\delta = 0$

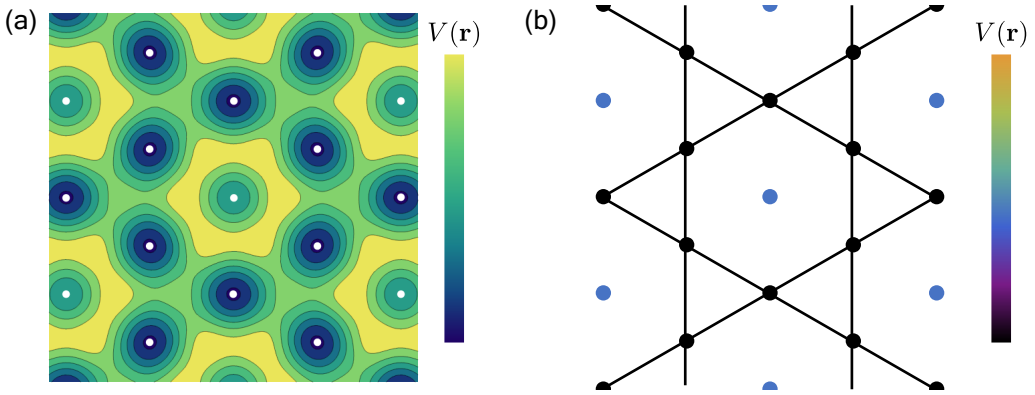

Figure 2.4: Potential (a) and local minima (b) of the kagome lattice. One site in four (blue dots) is detuned by the 1064 nm lattice, leaving resonant tunneling (black lines) between three sites (black dots). The optical superlattice discussed in this chapter was originally built to be the first realization of the kagome lattice [39]. There has long been interest in the kagome lattice because of its connection with spin frustration, a connection discussed in chapter 6. We performed a quantitative test of mean-field theory by comparing the superfluid-to-Mott insulator transition in triangular and kagome optical lattices [67].

1064 nm in-plane polarization, $\boldsymbol{\delta} = a\left(\frac{1}{2\sqrt{3}}, 0\right)$

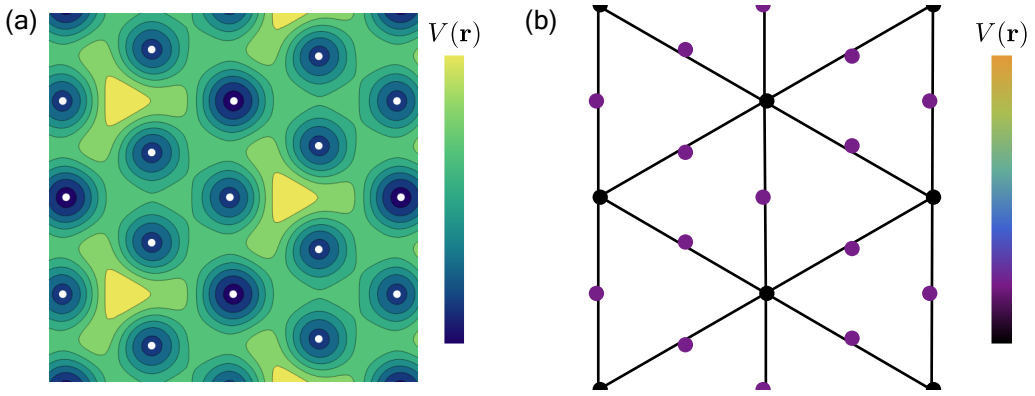

Figure 2.5: Potential (a) and local minima (b) of a triangular lattice. The global minima (black dots) are spaced apart by two sites of the original 532 nm triangular lattice. Tunneling between global minima (black lines) occurs as a second-order process via multiple detuned sites (purple dots).

1064 nm out-of-plane polarization, $\boldsymbol{\delta} = 0$

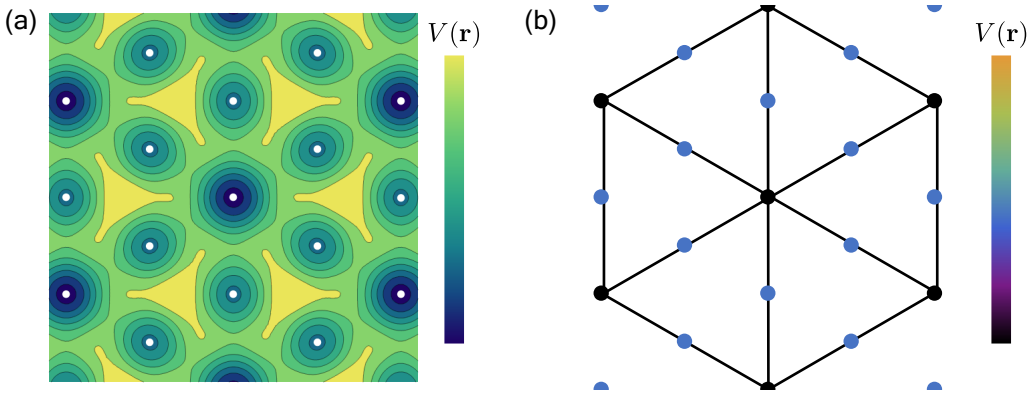

Figure 2.6: Potential (a) and local minima (b) of a triangular lattice. The global minima (black dots) are spaced apart by two sites of the original 532 nm triangular lattice. Tunneling between global minima (black lines) occurs as a second-order process via an detuned sites (blue dots).

1064 nm out-of-plane polarization, $\boldsymbol{\delta} = a\left(\frac{1}{2\sqrt{3}}, 0\right)$

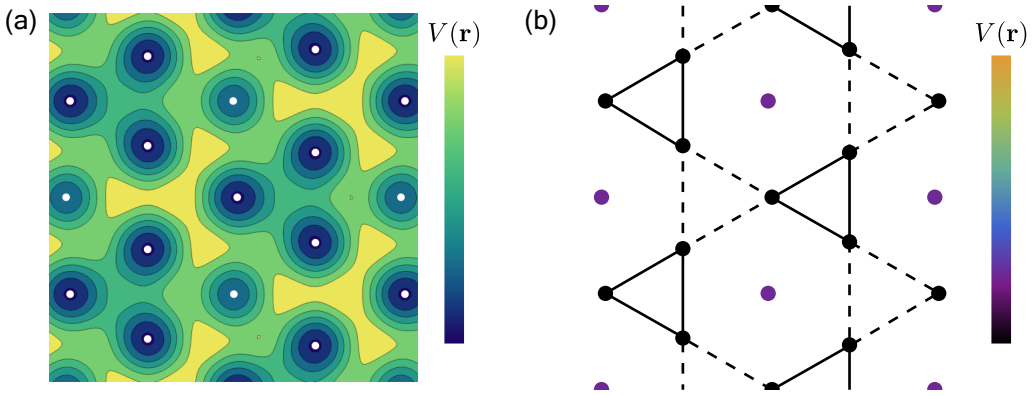

Figure 2.7: Potential (a) and local minima (b) of a trimerized kagome lattice. The 1064 nm lattice minima reduce the energy of three sites (black dots), leaving a detuned fourth site (purple dots). Strong tunneling occurs along solid black lines, whilst weak tunneling occurs along dashed lines. Chapter 6 is focused entirely on the experimental study of a new type of Mott insulating state on the trimerized kagome lattice with fractional filling per site.

532 nm out-of-plane polarization

The 532 nm out-of-plane polarized potential forms a honeycomb lattice of minima, with potential barriers between sites of only $\frac{1}{9}V_{532}$. With the prefactor of 0.5 in front of the 1064 nm lattice some of the superlattices with out-of-plane 532 nm polarization inherit this underlying structure, whilst some others do not have the same set of minima.

1064 nm in-plane polarization, $\boldsymbol{\delta = 0}$

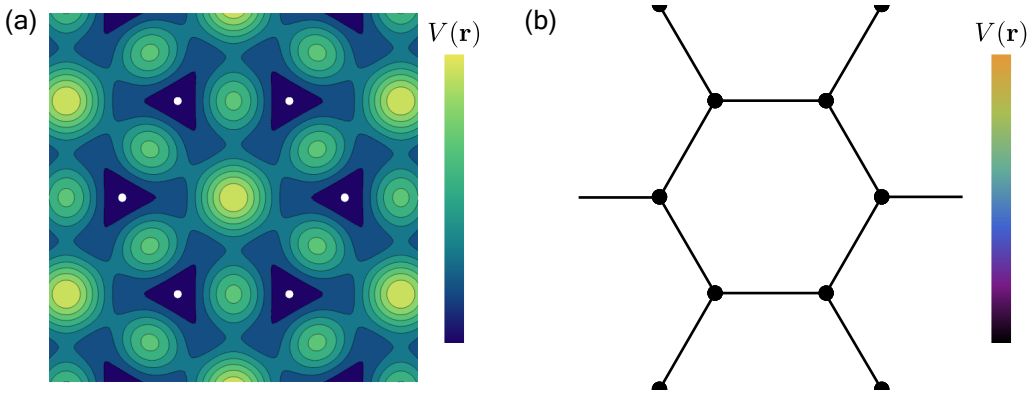

Figure 2.8: Potential (a) and local minima (b) of a honeycomb lattice. The minima (black dots) are spaced apart by more than 1 site of the original 532 nm honeycomb lattice. Some of the minima have disappeared. This combination of lattices is plotted with a 1064 nm prefactor of 0.6 to ensure the minima occur with moderate curvature.

1064 nm in-plane polarization, $\boldsymbol{\delta} = a\left(\frac{1}{2\sqrt{3}}, 0\right)$

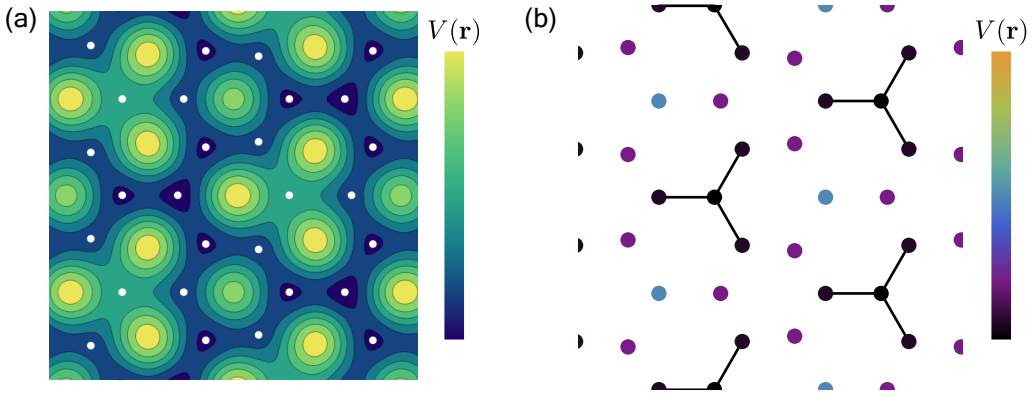

Figure 2.9: Potential (a) and local minima (b) of an unknown lattice. Four minima closely spaced in energy (black dots) are connected by close-to resonant tunneling (black lines). Tunneling between sets of four minima (not shown) occurs as a second-order process via detuned states (purple dots).

1064 nm out-of-plane polarization, $\boldsymbol{\delta = 0}$

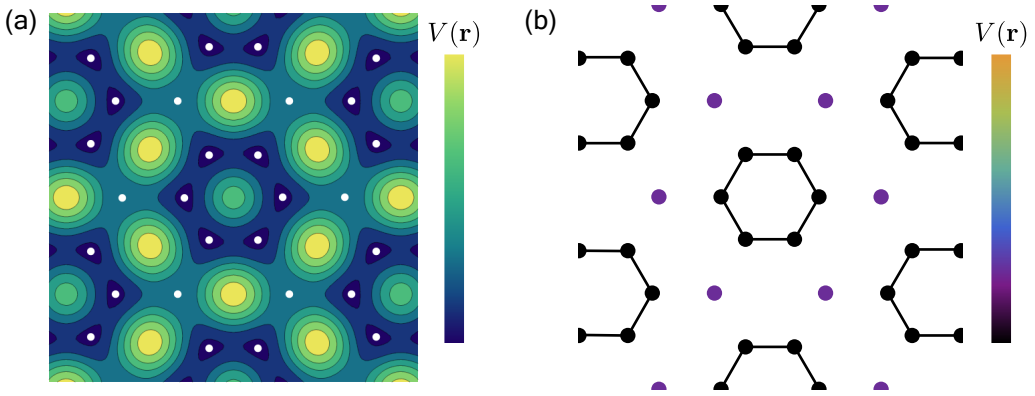

Figure 2.10: Potential (a) and local minima (b) of a lattice of hexagonal plaquettes. Strong tunneling (black lines) occurs between global minima (black dots). Tunneling between hexagons (not shown) occurs as a second order process through detuned sites (purple dots).

1064 nm out-of-plane polarization, $\boldsymbol{\delta = a\left(\frac{1}{2\sqrt{3}}, 0\right)}$

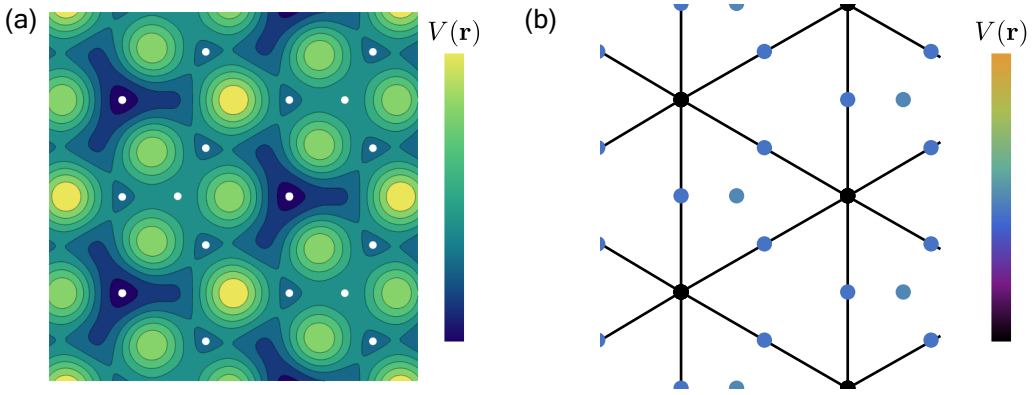

Figure 2.11: Potential (a) and local minima (b) of a triangular lattice. The minima are spaced apart by by more than 1 site of the original 532 nm honeycomb lattice. Tunneling between minima (black lines) occurs as a second-order process via detuned state (blue dots).

Chapter 3

A quantum simulator in practice

In the previous chapter we explained how idealized cold atoms and plane-wave optical lattices can be abstracted to the Bose-Hubbard model. In this chapter we describe a real experimental apparatus and the various steps that we take in order to justify our theoretical simplifications. We will briefly overview the techniques we use to make a Bose-Einstein condensate, the source of our cold atoms. Much of this information has been covered by previous members of this experiment, and their works will be referenced as appropriate.

To understand the simplifications made in the optical superlattice, we consider the individual terms that make up the expressions for the potentials in chapter 2, and explain how each polarization, wavevector and intensity need to be manipulated to realize our idealized potentials.

3.1 Cold atoms

Countless papers have been published, and two Nobel prizes awarded on the topic of cooling a dilute gas of alkali atoms from above room temperature to quantum degeneracy. As a result, we will just briefly overview the techniques used in this thesis and point to other works for greater detail.

The source of atoms

Our atoms begin within a glass ampule of high purity solid rubidium (5g prescored ampule from ESPI metals) that is placed in a cup inside the oven section of our vacuum chamber. The glass is broken under vacuum, and we heat the cup to 120° C to increase the vapor pressure of rubidium.

A small hole in the oven forms a collimated jet of atoms directed into the ultra-high vacuum region of our chamber. For details of the design of the oven, see Chapter 2 of Jennie Guzman's thesis [32]. For a comprehensive guide to replacing the rubidium in the oven, see Appendix D of Claire Thomas's thesis [66].

Zeeman slowing

The atoms leave the oven with a mean velocity around 300 m/s. We use the Zeeman slowing technique [55] with an increasing field slower to reduce their mean velocity, whereby the atoms are decelerated by the absorption of light red detuned from the $|F = 2, m_F = 2\rangle \rightarrow |F' = 3, m'_F = 3\rangle$ transition on the D2 line. A second frequency of light (repump) is used to pump atoms out of the $F = 1$ manifold.

A carefully designed magnetic field compensates for the change in Doppler shift as the atoms are decelerated. For details of this design, see Jennie Guzman's thesis [32].

Magneto-optical trap

The atoms are trapped and cooled by a magneto-optical trap (MOT) [70] formed by three pairs of counterpropagating laser beams, red detuned from the same transition as the Zeeman slower, and a pair of anti-Helmholtz electromagnet coils. We load the MOT from the Zeeman slower for 20 s.

Compressed MOT

After the MOT has loaded, the density is compressed to reduce the final temperature in the magnetic trap. The cooling light of the MOT is brought closer to resonance, and the power in the repump is cut for 20 ms. This is not exactly the implementation of the CMOT technique as described in the literature [54] as we do not increase the magnetic field gradient, and this should be addressed in the future.

Magnetic trapping and transport

The atoms are then captured in a quadrupole magnetic field, and magnetically transported into a glass cell [29]. In the CMOT phase the repump power is cut, causing the atoms to be pumped into the $F = 1$ manifold. A quadrupole magnetic field is then quickly turned on to a field gradient of 40 G/cm using the same coils as the magneto-optical trap. A moderate fraction of the atoms are thus trapped in the $|F = 1, m_F = -1\rangle$ state. Note: the rapid switch on of this magnetic field as described in Jennie Guzman's thesis is no longer used.

An additional three sets of overlapping quadrupole coils are sequentially magnetized, moving the field zero and thus the atoms into the glass cell in 6 s. This technique results in less than 20% atom loss. See Jennie Guzman's thesis for design details of these coils [32].

Microwave evaporation

The atoms undergo forced evaporation by selectively removing atoms from the magnetic trap via a microwave transition between the $|1, -1\rangle$ and $|2, 2\rangle$ hyperfine states. Once the magnetic transport of atoms into the glass cell is complete, the magnetic field gradient in the final pair of anti-Helmholtz coils is ramped to 120 G/cm. The increase in magnetic

field gradient compresses and heats the atoms, increasing the collision rate for more efficient evaporation. It is possible to increase this magnetic field gradient even more in the future by increasing the current run through these anti-Helmholtz coils, as they only reach a steady state temperature of 40° C.

We begin the evaporation with the microwave frequency well below the hyperfine transition, and slowly sweep it closer to resonance over 10 s. This selectively removes the hottest atoms, which cools the gas upon rethermalization. We note that the microwave evaporation as performed is relatively inefficient. The relatively low magnetic field gradient of 120 G/cm compared to experiments at Berkeley (175 G/cm)[48], Maryland (160 G/cm)[46] and Munich (240 G/cm) [45] could explain this inefficiency. We have seen increases in the efficiency of the evaporation at higher magnetic field gradients.

These microwave tones at ~ 6.8 GHz are generated by mixing a fixed frequency 7.0 GHz microwave oscillator (Luff Research PLDRO-700-10) with a programmable radio-frequency source (IFR 2023A) at ~ 200 MHz. These two tones are mixed on a +13 dBm mixer (Mini Circuits ZX05-153MH+) which produces tones at 6.8, 7.0 and 7.2 GHz. All off these tones are amplified by a +35 dB gain, +39 dBm output microwave amplifier (Miteq AMF-4B-06400720-50-39P), before being delivered to a helical antennae designed for 6.8 GHz.

The ~ 200 MHz RF signal can be switched on or off (Mini Circuits ZYSWA-2-50DR), but the microwave frequency signals can not be. Thus we can completely extinguish resonant microwave radiation at 6.8 GHz, but a 7.0 GHz tone is always present. This tone should be sufficiently off resonant from the hyperfine transition as to not affect the atoms, but this has not been systematically investigated.

Hybrid magnetic and optical trap

The gas is then loaded into a hybrid-optical magnetic trap before further evaporation [46]. A dipole trap is formed by a 43 μm waist, 6 W, 1064 nm beam. This beam is turned on 3 seconds before the end of microwave evaporation, and is located approximately a beam waist below the magnetic field zero.

The magnetic field gradient is lowered to 30 G/cm in the vertical direction over 1.5s , precisely canceling the potential gradient due to gravity for the $|1, -1\rangle$ atoms. This loads the atoms into a hybrid trap, where the dipole trap provides radial curvature, and the curvature of the magnetic field in the plane of the dipole trap provides axial confinement.

Evaporation is forced by lowering the dipole trap power, while at the same time the power in a second dipole trap is ramped on. After 2.5 seconds of optical evaporation, the depths provided by each arm of a crossed-dipole trap are approximately equal, and the curvature due to the magnetic field zero is decreased by increasing a vertical magnetic bias field over 0.5 s. Further evaporation occurs in the crossed-dipole trap for another 1.5 s.

When the lattice optics were rebuilt, we also redesigned the optical dipole traps. This experiment used to produce a BEC in a highly asymmetric 'surfboard trap' [32], formed by a 1064 nm wavelength beam focused to a waist of 10 μm $\times$ 100 μm. At 5 W initial power this produced a 300 μK deep trap, with sufficient axial trapping frequency for reasonably

efficient evaporation. The advantage of being able to produce a BEC with a single optical trap had the downside of a tight final vertical trap frequency of 350 Hz. The tight vertical trapping frequency resulted in a high density of atoms in the optical lattice. We chose this hybrid crossed dipole trap as it permitted very low vertical trap frequencies and thus atomic densities, as the potential due to gravity is canceled by the magnetic field.

Tilt evaporation

Optical evaporation is not particularly efficient, as decreasing the depth of the trap for evaporation typically reduces the trapping frequency, reducing the collision rate. We finish the evaporation to degeneracy with a more efficient technique: tilting the trap with a magnetic field gradient and keeping the trap frequencies approximately constant [35]. We introduce a gradient by decreasing the gravity compensating magnetic field gradient from 30 G/cm to 20 G/cm over 3 s. At the end of this sequence we produce a Bose-Einstein condensate of 1.5×10^5 atoms. To load optical lattices at low density, we increase the magnetic field back to 30 G/cm over 1 s, and reduce the crossed dipole strength. This relaxation is not particularly efficient, as it causes some degree of heating and subsequent evaporation.

Final result

Ultimately we produce a Bose-Einstein condensate 5×10^4 ^{87}Rb atoms in the $|F = 1, m_F = -1\rangle$ state. The thermal fraction is typically undetectable, and the final trap frequencies are $\omega_x = 2\pi \cdot 34$ Hz, $\omega_y = 2\pi \cdot 64$ Hz and $\omega_z = 2\pi \cdot 49$ Hz.

3.2 Triangular optical superlattice

Many details of our triangular optical superlattice are easy to write down in theory, but far more challenging to realize in practice. For example, in theory we can can simply impose a relationship between two wavevectors as,

$$\boldsymbol{k}_{532} = 2\boldsymbol{k}_{1064}. \tag{3.1}$$

In practice this will never precisely be true; we will ensure the magnitude and co-linearity of these two beams are correct to some tolerance. In this section we will systematically examine the assumptions we have made in writing down the potentials of the previous chapter, and describe the techniques we use to realize these assumptions within tolerance. We begin with a general expression for the potential formed by a superlattice consisting of 3 beams of 532 nm light and three beams of 1064 nm light:

$$V(\boldsymbol{r}) = |\sum_{i=1}^{3} \sqrt{V_{532,i}(\boldsymbol{r})} e^{i\boldsymbol{k}_{532,i}\cdot\boldsymbol{r}+\phi_{532,i}} \boldsymbol{\epsilon}_{532,i}|^2 + |\sum_{i=1}^{3} \sqrt{V_{1064,i}(\boldsymbol{r})} e^{i\boldsymbol{k}_{1064,i}\cdot\boldsymbol{r}+\phi_{1064,i}} \boldsymbol{\epsilon}_{1064,i}|^2. \tag{3.2}$$

Each beam has spatial profile $V_i(\boldsymbol{r})$, wavevector $\boldsymbol{k}_i$, phase ϕ_i and polarization $\boldsymbol{\epsilon}_i$. We consider these different parameters in a systematic way, and examine the techniques use to achieve the simpler potentials of the previous chapter.

We explore the tolerances of our most sensitive lattice geometry, the trimerized kagome lattice, in chapter 6. For the trimerized kagome lattice, we require that the minima of the 1064 nm lattice is correct to within 1 nm.

Polarization

The polarization of the lattice beams are set by polarizing beamsplitters (Advanced Thin Films, model number PBS1005-SBB), and a λ at 532 nm, $\lambda/2$ at 1064 nm waveplate (Newlight WPD02-H1064-F532-UM) just before the focusing lenses on each path. The polarization into the waveplate can be treated as purely horizontal as the extinction ratio of the beamsplitter is 2000:1. However, as the waveplate is multi-order, the retardance may not exactly be $\lambda/2$.

In the kagome lattice configuration, the waveplate gives no rotation and we can entirely ignore polarization impurities. In the trimerized kagome lattice configuration, the waveplate rotates the 1064 nm light to vertical. Using a temporary polarizer before the glass cell we measure an average extinction ratio of 500:1 for the 1064 nm light, and thus treat the polarization as pure.

Spatial profile

We break down the problem of the spatial profile $V_i(\boldsymbol{r})$ into two components: the shape of the spatial profile, and where it is centered in space. We focus on the shape in this section, then the alignment in later sections.

We want the spatial profile of the beams to be much larger than the extent of the atoms so that we can ignore the changing lattice depth, far from the beam center. We also want all three of the beams to be the same size, so that when the intensities at the center of the gas are equal they are also equal at the edge of the gas. When the beam sizes are different, balancing the intensities at the center of the gas results in incomplete interference at the edge of the gas. This leads to extra curvature or anti-curvature in the potential.

As described in Claire Thomas's thesis, the spatial profile of the 1064 beams us determined by the optical fiber they are coupled into, the fiber outcoupler, and the final focusing

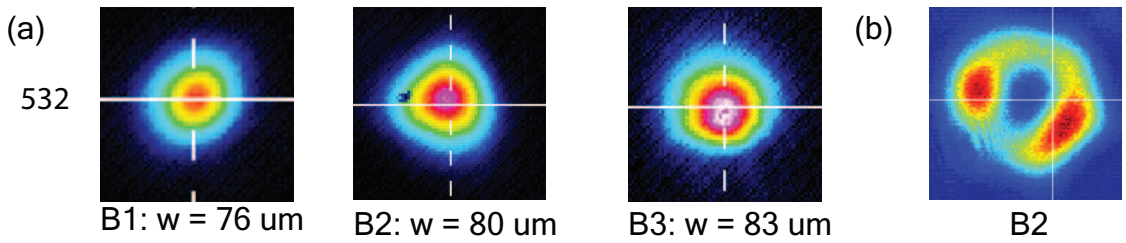

Figure 3.1: Images of the spatial intensity profile of 532 nm B1, B2 and B3 taken at the focus. (a) Beam profiles immediately after second replacement of beamsplitters. The three beams have approximately Gaussian modes, and the beam waists are equal to within 10%. (b) Strongly distorted beam profile of B2 before the second replacement of beamsplitters.

optics [66]. The measured beam profiles at the focus are highly Gaussian, and agree in size to within 10%.

The 532 nm beams however, have been historically more challenging to produce with a consistent Gaussian mode. We have noticed a long term damage mechanism to a number of brands of polarization beamsplitters that produces a distinctly non-Gaussian mode, seen in figure 3.1(b). The measurement of the beam intensity at the focus of the optical lattice shows a clear depletion in the central region of the beam.

We have clearly identified the beamsplitters responsible for the non-Gaussian beam mode. The first beamsplitter responsible was directly after the Verdi, controlling the power into the three lattice beams. It was exposed to 18 W of 532 nm wavelength light at a 2 mm diameter and an intensity of 600 W/cm^2. This beamsplitter was exposed to the 532 nm light from morning till evening most days for three years. We began leaving the Verdi on permanently in late 2017, and the deterioration in beam quality happened a few months later. After replacing this beamsplitter we recovered Gaussian beam modes.

The replacement beamsplitter was also replaced six months later, along with the beamsplitters use to divide the 532 nm light into three beams. The replacement beamsplitter had been exposed to 600 W/cm^2 continuously for six months, whereas the dividing beamsplitters had been exposed to 1200 W/cm^2 - 600 W/cm^2 daily for three years, and continuously for the last six months. The damage to all of these beamsplitters is responsible for the non-Gaussian beam profile in 3.1(b), and it required the replacement of all three beamsplitters to produce the Gaussian profiles seen in 3.1(a). We have seen improvements in beam quality by simply rotating optics in their mounts, but we have not recovered fully Gaussian beams without completely replacing the optics.

If we replace the beamsplitters, we create approximately Gaussian beams with focused waists that agree to within 10%, as seen in 3.1(a). The remaining variation in the beam size can be compensated for with a variation of the power in each beam, so that the intensity in the center is identical. This does mean that the interference will not be complete over the entire beam profile, which leads to extra curvature in the potential.

k-vectors

In the triangular optical superlattice the lattice sites are approximately defined by the minima of the 532 nm lattice, and the 1064 nm lattice modifies the energy and tunneling strengths of these sites. If the wavevectors of the 532 nm light and 1064 nm light along direction i do not satisfy

$$\boldsymbol{k}_{532,i} = 2\boldsymbol{k}_{1064,i}, \tag{3.3}$$

the relative position of the 1064 minima or maxima varies with respect to the 532 nm over the lattice, introducing inhomogeneities to the Bose-Hubbard model. We break down this requirement into a magnitude requirement, and a co-linearity requirement.

Magnitude

We find a requirement on the relative magnitudes of the 532 nm and 1064 nm wavevectors by assuming their relative position is correct at the center of the atomic gas and calculating the relative displacement at the edge of the gas defined by the Thomas-Fermi radius R_{TF}. The relative displacement at the edge is

$$\begin{aligned}\delta x &= \frac{R_{TF}}{a_{1064}}(2a_{532} - a_{1064}) \\ &= R_{TF}\left(\frac{2a_{532}}{a_{1064}} - 1\right),\end{aligned} \tag{3.4}$$

where a_{532} and a_{1064} are the lattice spacings of the 532 nm and 1064 nm lattices respectively. Converting this to the fractional deviation $2|k_{1064}|/|k_{532}| - 1$ of the wavevectors, we require

$$\left(\frac{2|k_{1064}|}{|k_{532}|} - 1\right) < \frac{\delta x}{R_{TF}}. \tag{3.5}$$

We typically measure the magnitude of the wavevectors in frequency, so we require

$$\left(\frac{2f_{1064}}{f_{532}} - 1\right) < \frac{\delta x}{R_{TF}}. \tag{3.6}$$

For a 1 nm displacement, we require less than a 10^{-4} fractional deviation of $2 \cdot a_{532}$ and a_{1064}. Whilst our 532 nm and 1064 nm lasers are not referenced in any manner, they approximately satisfy this requirement as shown in table 3.1.

Date	f_{1064}	f_{532}	Fractional deviation
8/8/18	281.633985 THz	563.204126 THz	2×10^{-4}

Table 3.1: Representative 1064 nm and 532 nm laser frequencies and calculated fractional deviation.

Angle

If $\boldsymbol{k}_{532}$ and $\boldsymbol{k}_{1064}$ are not collinear, there is another inhomogeneity due to the rotation of the two underlying lattices. A small in-plane angle between the beams θ gives a transverse displacement of the 1064 minima/maxima at the edge of the lattice, again given by R_{TF}. This displacement is approximately

$$\begin{aligned} \delta y &\approx \theta \left(\frac{R_{TF}}{a_{1064}} \right) a_{1064} \\ &= \theta R_{TF}. \end{aligned} \tag{3.7}$$

Thus for a given displacement δy, we require the relative angle θ between the beams to satisfy:

$$\theta < \frac{\delta y}{R_{TF}}. \tag{3.8}$$

For a δy =1 nm displacement, we require less than a 10^{-4} angular deviation.

Collinearity technique

The $\theta < 10^{-4}$ angular deviation condition derived in the previous section, requires the beams to be overlapped to within 25 μm at both ends of a 250 mm distance. We achieve this by placing a mirror after the optical lattice focusing lens and mounting a CCD camera on rails. This allows us to measure the central position of the Gaussian waist of both the 532 nm and 1064 nm beams, at the focal plane and close to the lens. We iteratively align these beams to each other, and calculate the angular deviation θ as:

$$\theta = \frac{\sqrt{\Delta X_{Focal}^2 + \Delta X_{Lens}^2}}{L}. \tag{3.9}$$

Results from a recent alignment are given in table 3.2, showing that we almost satisfy the requirement $\theta < 10^{-4}$. An advantage of this technique is that the 532 nm and 1064 nm beams are well overlapped at the focal plane, and as such they can be aligned to the atoms together.

Date	ΔX Focal Plane (average)	ΔX Lens (average)	θ (average)
08/25/18	2.4 um	21 um	1×10^{-4}

Table 3.2: Representative results of the iterative alignment of the 532 nm and 1064 nm beams. ΔX is the difference between the fitted Gaussian centers of the 1064 nm beam, either in the focal plane, or at the lens. An average over all three pairs of beams is quoted.

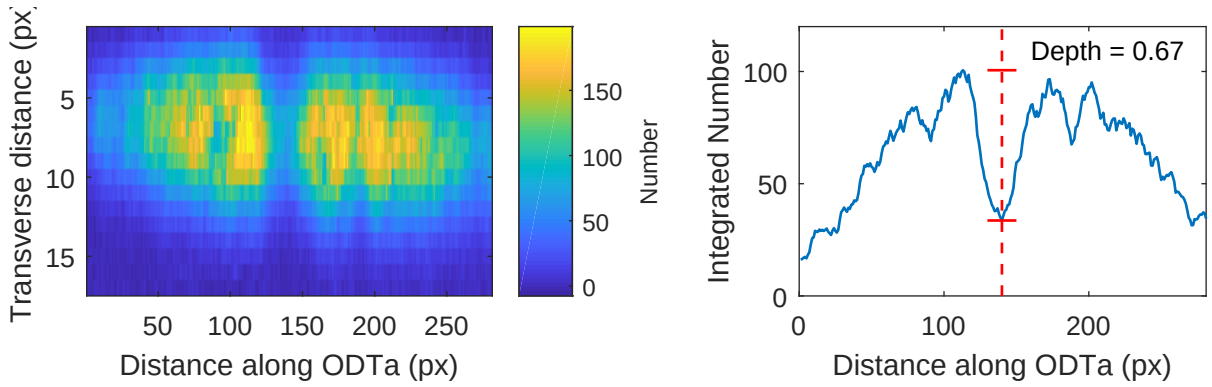

Figure 3.2: *In-situ* density distributions obtained using the 'cut' technique. (a) The in-situ density distribution of a thermal gas in a single optical dipole trap traveling horizontally. A vertical stripe of lower density shows the presence of the repulsive 532 nm beam. (b) Averaged density distribution of (a). Averaging is done along the vertical direction. We use the depth of the density decrease to optimize the out-of-plane alignment of the 532 nm beams.

Overlap

As the collinearity technique precisely aligns the 532 nm and 1064 nm beams to each other in the focal plane to within a few microns, we only have to align the co-propagating beams to the atoms. To find the position of the 532 nm beams, we stop evaporation in the crossed dipole trap with a large number of atoms, and relax the gas into a single dipole trap. Turning on the repulsive 532 nm light causes a local decrease in the *in-situ* density, as seen in figure 3.2(a). We align the in-plane position of the the repulsive potential to the position of the Bose-Einstein condensate obtained from *in-situ* imaging. The vertical position of the beams is aligned by maximizing the depth of the density displacement, as shown in figure 3.2(b).

3.3 Beam balancing

Once all of the beams are aligned to the atoms, we balance the single beam potential depths $V_{532,i}$ to create a symmetric lattice. With no imperfections in the system, we would simply set the power in the beams to be equal. However, due to finite levels of misalignment and different sizes of the beams we use the atoms to balance the relative potential depths.

If our time-of-flight measurements are a faithful representation of the momentum distribution, then the size of the diffraction peaks of a superfluid released from an optical lattice are proportional to the Fourier transform of the Wannier function $|\tilde{w}(\boldsymbol{k})|^2$ at the reciprocal lattice vectors $\boldsymbol{G}_i$. By balancing the populations in the momentum peaks we symmetrize the Wannier function $w(\boldsymbol{k})$, and thus ensuring the curvature in each potential well of the lattice is symmetric. In principle, this makes the potential depths symmetric.

We load an atomic superfluid into either of the 532 nm or 1064 nm lattices, either in-plane or out-of-plane polarization, and make measurements of the first order diffraction peaks in time-of-flight. We adjust the relative power in one beam until two sets of peak have equal number, then adjust the power in a third until all three sets of peaks have equal population. An example of this procedure is shown in detail in section 3.3.

Theoretical description

To examine this procedure in greater depth, we calculate the dependence of the population of the first order momentum peaks $P_{\boldsymbol{G}_i}$ on the imbalance of the single beam potential depths $V_{532,i}$. Following the argument in chapter 5, the momentum distribution of a triangular lattice, is simply a set of delta functions at the reciprocal lattice vectors,

$$n(\boldsymbol{k}) = N \sum_{\boldsymbol{G}_i} n_{\boldsymbol{G}_i} \delta(\boldsymbol{k} - \boldsymbol{G}_i) \tag{3.10}$$

with weights

$$n_{\boldsymbol{G}_i} = |\tilde{w}(\boldsymbol{G}_i)|^2. \tag{3.11}$$

This applies to both the 532 nm lattice and the 1064 nm lattice for appropriate choices of the reciprocal lattice vectors $\boldsymbol{G}_i$. The populations we measure are simply $N|\tilde{w}(\boldsymbol{G}_i)|^2$, effectively sampling the Fourier transform of the Wannier function at $\boldsymbol{G}_i$. We make the Gaussian approximation of the Wannier function, and assume the curvature is diagonal in the x and y axes. The Wannier function $w(\boldsymbol{r})$ thus takes the form:

$$w(\boldsymbol{r}) = \frac{1}{\pi^{1/2}\sqrt{a_x a_y}} e^{-\frac{(x-x_0)^2}{2a_x^2} - \frac{(y-y0)^2}{2a_y^2}} \tag{3.12}$$

where $a_i = \sqrt{h/m\omega_i}$ are the harmonic oscillator lengths in x and y. Taking the Fourier transform as defined in section 5.1 gives us

$$|\tilde{w}(\boldsymbol{k})|^2 = \frac{2}{\pi^{1/2}} \sqrt{a_x a_y} e^{-a_x^2 k_x^2} e^{-a_y^2 k_y^2}. \tag{3.13}$$

This form allows us to calculate the strength of the Wannier function at $\boldsymbol{G}_1 = G(\frac{1}{2}, \frac{\sqrt{3}}{2})$ and $\boldsymbol{G}_2 = G(-1, 0)$:

$$P_{\boldsymbol{G}_1} = N|\tilde{w}(\boldsymbol{G}_1)|^2. = N \frac{\sqrt{a_x a_y}}{\pi^{1/2}} e^{-\frac{a_x^2 G^2}{4} - \frac{3G^2 a_y^2}{4}} \tag{3.14}$$

$$P_{\boldsymbol{G}_2} = N|\tilde{w}(\boldsymbol{G}_2)|^2. = N \frac{\sqrt{a_x a_y}}{\pi^{1/2}} e^{-G^2 a_x^2} \tag{3.15}$$

Therefore the population ratio $P_{\boldsymbol{G}_1}/P_{\boldsymbol{G}_2}$ is

$$\frac{P_{\boldsymbol{G}_1}}{P_{\boldsymbol{G}_2}} = \exp\left(3G^2 a_x^2 \left(\frac{a_x^2 - a_y^2}{a_x^2}\right)\right). \tag{3.16}$$

Assuming the single beam potential depths in beams 1 and 3 (V_1 and V_3 respectively) are equal, and different from that of beam 2 (V_2) allows us to write an explicit form of the potential:

$$\begin{aligned} V(\boldsymbol{r}) = &-\sqrt{V_1}\sqrt{V_2}\cos\left(\frac{\sqrt{3}x}{2} - \frac{3y}{2}\right) - \sqrt{V_1}\sqrt{V_2}\cos\left(\frac{\sqrt{3}x}{2} + \frac{3y}{2}\right). \\ &- V_1\cos\left(\sqrt{3}x\right) + 2V_1 + V_2 \end{aligned} \tag{3.17}$$

Evaluating the x and y curvatures of this potential allow us to calculate the following terms:

$$(a_x^2 - a_y^2)/a_x^2 = 1 - \sqrt{\frac{2}{3}\sqrt{\frac{V_1}{V_2}} + \frac{1}{3}} \tag{3.18}$$

$$\begin{aligned} a_x^2 &= \frac{h}{\sqrt{G^2 m(3V_1 + \frac{3}{2}\sqrt{V_2}\sqrt{V_1})}} \\ &\approx \frac{h}{G\sqrt{mV_{532}}}. \end{aligned} \tag{3.19}$$

where we have assumed $V_1 \approx V_2$ for calculating the prefactor a_x^2. Note that $V_{532} = \frac{9}{2}V_1$ in this assumption. Expressing the lattice depth in terms of the recoil energy $V_{532} = sE_r$ we derive a final expression for the relative momentum space population:

$$\frac{P_{\boldsymbol{G}_1}}{P_{\boldsymbol{G}_2}} = \exp\left(\frac{2\sqrt{6}\pi}{\sqrt{s}}\left(1 - \sqrt{\frac{2}{3}\sqrt{\frac{V_1}{V_2}} + \frac{1}{3}}\right)\right). \tag{3.20}$$

Note that as the lattice depth s increases, the sensitivity of the calibration decreases. However increasing the lattice depth does increase the population in $P_{\boldsymbol{G}}$, which increases the accuracy of the measurement $\frac{P_{\boldsymbol{G}_1}}{P_{\boldsymbol{G}_2}}$. To estimate the sensitivity of this measurement, we let $\frac{V_1}{V_2} = 1 + \Delta_V$ and $\frac{P_{\boldsymbol{G}_1}}{P_{\boldsymbol{G}_2}} = 1 + \Delta_P$, and find

$$\Delta_V = \frac{\sqrt{6}\sqrt{s}}{2\pi}\Delta_P. \tag{3.21}$$

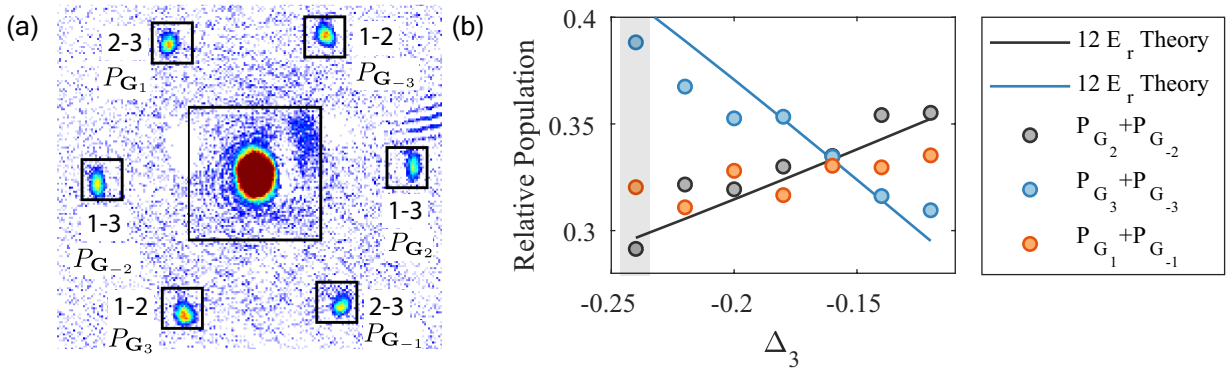

Figure 3.3: Details of the beam balancing procedure. (a) A time-of-flight image of a superfluid loaded into an imbalanced 532 nm triangular lattice, for $\Delta_3 = -0.24$. The first order momentum peaks $P_{\boldsymbol{G}_i}$ are labeled by their reciprocal lattice vector $\boldsymbol{G}_i$ and the pair of beams $m - n$, for which $|\boldsymbol{G}_i| = |\boldsymbol{k}_m - \boldsymbol{k}_n|$. (b) The extracted relative populations of the superfluid (circles) as Δ_3 is scanned and the theoretical populations calculated with equations 3.24 and 3.25.

In practice, we tend to balance the lattice around $V_{532} = 50$ kHz $= 11\, E_r$. A typical value of Δ_P is 2/30, which gives a typical error of

$$\Delta_V = 0.09. \tag{3.22}$$

This method isn't particularly precise, and it relies on a number of assumptions. As explained further in section 5.1, the time-of-flight density pattern of a superfluid is not necessarily representative of the momentum distribution. Interaction effects are not negligible, and the far-field time for a fully coherent 10 μm wide cloud is 130 ms. As we typically use a time of flight of 16 - 30 ms, we never reach the true far field limit.

Calibration example

We test the previous section's theoretical calculation of the population imbalance by comparing it to the outcome of our experimental beam balancing procedure. In the lab, the single beam potential depth of beam 3 (V_3) is set relative to beam 2

$$V_3 = V_2 10^{2.5(\Delta_{3,0} - \Delta_3)}, \tag{3.23}$$

where Δ_3 is a control parameter, and $\Delta_{3,0}$ is the value of Δ_3 that sets $V_3 = V_2$. In principle $\Delta_{3,0} = 0$, but different beam sizes and calibrations of the control parameters require us to find $\Delta_{3,0}$ experimentally. If $V_2 = V_1$, i.e. beam 1 and beam 2 are already balanced, then adapting equation 3.20 tells us the population in the following first order momentum peaks,

$$P_{\boldsymbol{G}_3} = \left(1 + 2\exp\left(-\frac{2\sqrt{6}\pi}{\sqrt{s}}\left(1 - \sqrt{\frac{2}{3}\sqrt{\frac{V_3}{V_2}} + \frac{1}{3}}\right)\right)\right)^{-1} \tag{3.24}$$

and

$$P_{\boldsymbol{G}_2} = \left(\exp\left(\frac{2\sqrt{6}\pi}{\sqrt{s}}\left(1 - \sqrt{\frac{2}{3}\sqrt{\frac{V_3}{V_2}} + \frac{1}{3}}\right)\right) + 2\right)^{-1}. \tag{3.25}$$

These theoretical momentum space populations are compared to those extracted from time-of-flight images in figure 3.3(b), over a range of Δ_3 for an assumed optical lattice depth of 60 kHz (12 E_r). The slope of the theoretical curves are approximately consistent with the data if we choose $\Delta_{3,bal} = -0.16$.

Alternative: 1D lattice calibration

The three beam method we use for producing a triangular optical lattice also produces three pairs of one dimensional optical lattices. If the polarization is in-plane, the 1D lattices take the form

$$V_{1D,in}(\boldsymbol{r}) = 2 - \cos(\boldsymbol{G}_i \cdot \boldsymbol{r}). \tag{3.26}$$

If the polarization is out of plane, the lattice potential is

$$V_{1D,out}(\boldsymbol{r}) = 2 - 2\cos(\boldsymbol{G}_i \cdot \boldsymbol{r}). \tag{3.27}$$

Each of the pairs of optical lattices can be calibrated using amplitude modulation spectroscopy, described in section 3.4. In the thesis of C. Becker [4], this is argued to be a more reliable technique than the balancing the diffraction pattern, due to the precision of the lattice calibration measurements.

It must be noted however, when the polarization of the lattice light is in-plane, as is the case for the 532 nm triangular lattice, the potential is not zero at the minima of the 1D optical lattice. As a result, there is a substantial anti-curvature in the transverse direction that could displace the atoms from the maximum beam intensity, leading to a miscalibration.

Mott insulator coherence

Throughout chapter 5, we detail measurements of the phase coherence of a Mott insulator via the sinusoidal modulation of the Wannier function. Deep in the Mott insulating regime, we fit the time-of-flight image with the functional form

$$n(\boldsymbol{k}) = N|\tilde{w}(\boldsymbol{k})|^2(1 + \alpha_1\cos(\boldsymbol{k}\cdot\boldsymbol{a}_1) + \alpha_2\cos(\boldsymbol{k}\cdot\boldsymbol{a}_2) + \alpha_2\cos(\boldsymbol{k}\cdot\boldsymbol{a}_3)), \tag{3.28}$$

where $|\tilde{w}(\boldsymbol{k})|^2$ is a Gaussian function, $\boldsymbol{a}_1$ and $\boldsymbol{a}_2$ are the lattice vectors and $\boldsymbol{a}_3 = \boldsymbol{a}_1 - \boldsymbol{a}_2$. When the lattice is not symmetric, these coherences α_i as defined in section 5.1, take the form

$$\alpha_i = 4(n+1)U/J_i, \tag{3.29}$$

where J_i is the tunneling element in the direction , U is the interaction strength and n is the number of particles per site. In equilibrium, the ratio $\alpha_1/\alpha_2 = J_2/J_1$, and so balancing the measurements of the nearest-neighbor coherence α in effect balances the tunneling elements J.

In principle this is a powerful method as it directly calibrates the symmetry at the level of the Bose-Hubbard model, not its underlying optical lattice. Given the approximately exponential dependence of the tunneling elements on the lattice depth, this in principle is a more precise calibration method. However, it assumes an equilibrium Mott insulator state, which we know we have trouble producing. The out of equilibrium behavior we see in the Mott insulating state may or may not be relevant to the validity of this technique. A detailed experimental comparison with the first beam balancing technique is thus required. For experiments in the Mott insulating phase, such as in chapter 5 and 6, we used this coherence balancing method.

3.4 Lattice depth calibration

The depths of the 532 nm and 1064 nm lattices are calibrated via amplitude modulation spectroscopy of a superfluid. In this section we will give a brief overview of this technique, refer the reader to Claire Thomas's thesis for a detailed discussion, and point out some complications we have found with this method.

Overview

The amplitude modulation spectroscopy is performed after alignment and balancing of the beams. Thus the lattice is symmetric, but with an unknown amplitude.

As with the beam balancing technique, we load a Bose-Einstein condensate into either a 532 nm or 1064 nm triangular optical lattice. This is either done in the presence of another optical lattice, propagating out of plane, or a simple confining dipole potential. This out of plane or vertical lattice increases the density, making the gas strongly interacting. These interactions provide a significant complication of this calibration procedure, which is discussed in the next section. If we do calibrate the optical lattice depth in the presence of strong interactions, we do so at low enough depth to ensure the gas is in the superfluid region of the Bose-Hubbard phase diagram.

Amplitude modulation of the lattice is performed by simultaneously modulating the power of all three lattice beams at frequency ω. In practice we do this by modulating the

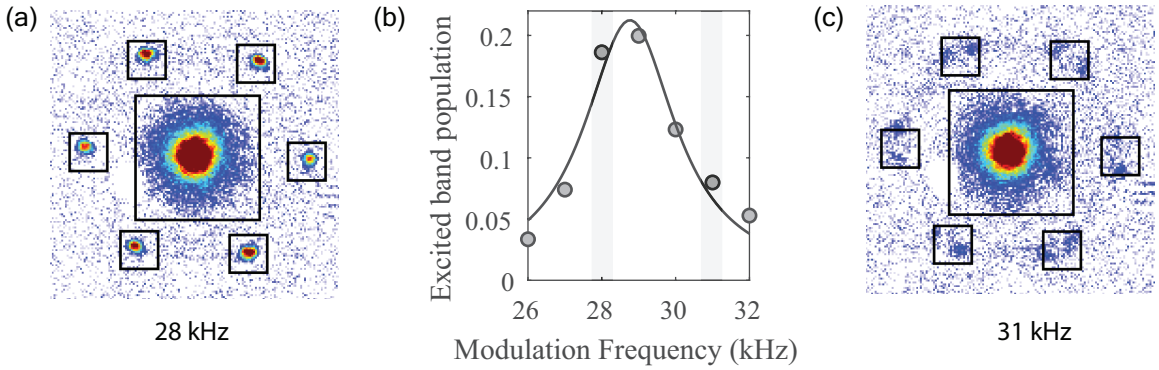

Figure 3.4: Details of the lattice depth calibration procedure. (a) Band-mapping image of the resonant amplitude modulation at 28 kHz of a strongly interacting superfluid. Coherent peaks at the reciprocal lattice vectors correspond to $\boldsymbol{q} = 0$ atoms in the 4th excited band. (b) Extracted 4th band population as the amplitude modulation frequency is changed (circles). A resonance frequency of 28.8 kHz is extracted, corresponding to a lattice depth of 51.6 kHz. Note that data points at higher frequencies generally exhibit higher population than those at lower frequency. (c) Response at 31 kHz. Sharp diffraction peaks are not seen at the reciprocal lattice vectors, but instead two weak peaks appear at either side of the reciprocal lattice vectors. Faint lines connect the reciprocal lattice vectors. These atoms are evidence of a $\boldsymbol{q} \neq 0$ response.

gain of an exponential amplifier that drives the acousto-optic modulators that set the power in the beams. We avoid large modulation amplitudes to prevent distortion of the signal.

In quasi-momentum space, the superfluid initially occupies the $\boldsymbol{q} = 0$ state of the ground band. The amplitude modulation is an even parity perturbation of the lattice, so it only couples the $\boldsymbol{q} = 0$ ground band state to $\boldsymbol{q} = 0$ excited band states with even parity. This coupling is resonant when the drive frequency $h\omega$ is equal to the energy spacing between the ground band and the excited band $\boldsymbol{q} = 0$ states.

The modulation is simply turned on for a period of time $t = 1$ ms at a particular frequency ω, after which we perform the band mapping technique, which maps quasi-momenta to real momenta [28]. We perform spectroscopy on the fourth band, for which the $\boldsymbol{q} = 0$ points map to the first order reciprocal lattice vectors $\boldsymbol{G}_i$ under band mapping. The band structure of the triangular lattice is shown in figure 2.2 of Claire Thomas's thesis, and shows the ground to 4th bands. As the $\boldsymbol{q} = 0$ state of the ground band just maps to $\boldsymbol{k} = 0$, this gives us a background free measurement. A time-of-flight image of the band mapping of this resonant excitation is shown in figure 3.4.

Band structure calculations allow us to connect the resonance frequency of the fourth band to the total lattice depth, thus giving us a calibration of the lattice depth [21]. Details on how the band structure calculations are performed, and an examination of the consistency of calibrations are in Claire Thomas's thesis, section 2.5.2 [66].

Vertical lattice challenges

In section 5.6, we describe a simplification of the trapping potentials that confine our atoms. Instead of two dipole traps, a magnetic gradient, and a vertical lattice, we simply load atoms into a one-dimensional optical lattice propagating orthogonal to the plane of the optical lattice.

The optical lattice depth calibrations is more reliable when measured under identical confinement conditions of the atoms as they experience in the full superlattice. As a result we calibrate the optical lattice depth in the presence of this vertical lattice, which substantially increases the role of atomic interactions.

We must precisely choose the lattice depth at which to calibrate due to two competing constraints. For the 532 nm triangular lattice, the lattice depth V_{532} must be above 40 kHz to perform an accurate calibration. Below 40 kHz, the ground band to fourth band excitation frequency is insensitive to the lattice depth. We must also keep the lattice depth sufficiently low to minimize the effect of the Mott insulating transition. For a central filling of $n = 1$, the entire gas is Mott insulating at $V_{532} = 70$ kHz. Whilst this appears to give us substantial range of acceptable lattice depths for calibration, the long range coherence of the gas is completely lost at 70 kHz. Thus even at 40 kHz the interactions are relevant, causing the gas to broaden from $\boldsymbol{q} = 0$ in momentum space.

Amplitude modulation thus drives resonances at multiple values of $\boldsymbol{q}$, simultaneously broadening the resonance, and depleting the $\boldsymbol{q} = 0$ signal. For the ground to fourth excited band, these extra resonances occur at higher frequencies, as seen in 3.4(b). The measured excited state population is higher for frequencies above the resonance than below, and a number of atoms can be seen away from the reciprocal lattice vectors for modulation at 31 kHz, shown in 3.4(c).

Finally, the interaction energy of the initial and final states are not exactly the same, shifting the overall resonance. For weak pulses exciting only a small fraction of atoms to the excited band, the relevant comparison is the interaction of two ground band atoms, and a ground and excited band atom.The interaction energy of one excited state atom and one ground state atom U_{ge} is defined by

$$U_{ge} = \int |w_g(\boldsymbol{r})|^2 |w_e(\boldsymbol{r})|^2 d\boldsymbol{r} \tag{3.30}$$

for the ground state and excited state Wannier functions, $w_g(\boldsymbol{r})$ and $w_e(\boldsymbol{r})$ respectively. It is not clear whether this leads to an overestimate or underestimate of the resonance, but it certainly causes a density dependent shift, which further broadens the response.

Calibrating the triangular lattice depths in the presence of the vertical lattice requires further understanding. It should be noted that the modulation responses of gases prepared in a vertical lattice or in a simple dipole trap are reasonably similar, and the effect of the interactions on the lattice depth represents less than a 10% error.

Chapter 4

Phase stabilization

This chapter details the experimental scheme to stabilize and control the relative displacement of the individual triangular lattices that make up the optical superlattice. This stabilization scheme is a critical component of our apparatus: its successful implementation allows us to realize unique optical lattice geometries such as the trimerized kagome lattice. However, realizing such exotic geometries introduces new mechanisms for noise to couple into the atomic system. Thus it is critical that the stabilization system does not introduce too much extra noise, otherwise it will obscure the ground state Bose-Hubbard physics that we are trying to study.

In the first section of this chapter we explain the fundamental mechanism used to stabilize the relative displacement of the optical lattices: enforcing boundary conditions of the electric field with feedback. We will explain the similarities between our scheme and the optical superlattice experiments elsewhere in the community. We will also explain how we control the relative displacement arbitrarily, and we will explore some failure mechanisms of our scheme.

The feedback used to enforce boundary conditions will involve the implementation of an optical phase-locked loop (PLL). We will briefly overview the theory of phase-locked loops, before explaining how our optical and electrical hardware makes up the three essential components of a PLL: a phase detector, a voltage controlled oscillator (VCO) and a loop filter.

Finally we examine the effectiveness of this scheme.

4.1 Enforcing boundary conditions

The optical superlattice is formed by two independent triangular optical lattices, one from the interference of 532 nm light, and the other by 1064 nm light. In the lab frame the potentials experienced by the atoms are given by

$$V(\boldsymbol{r}) = V_{532}(\boldsymbol{r} - \boldsymbol{\delta}_{532}) + V_{1064}(\boldsymbol{r} - \boldsymbol{\delta}_{1064}), \tag{4.1}$$

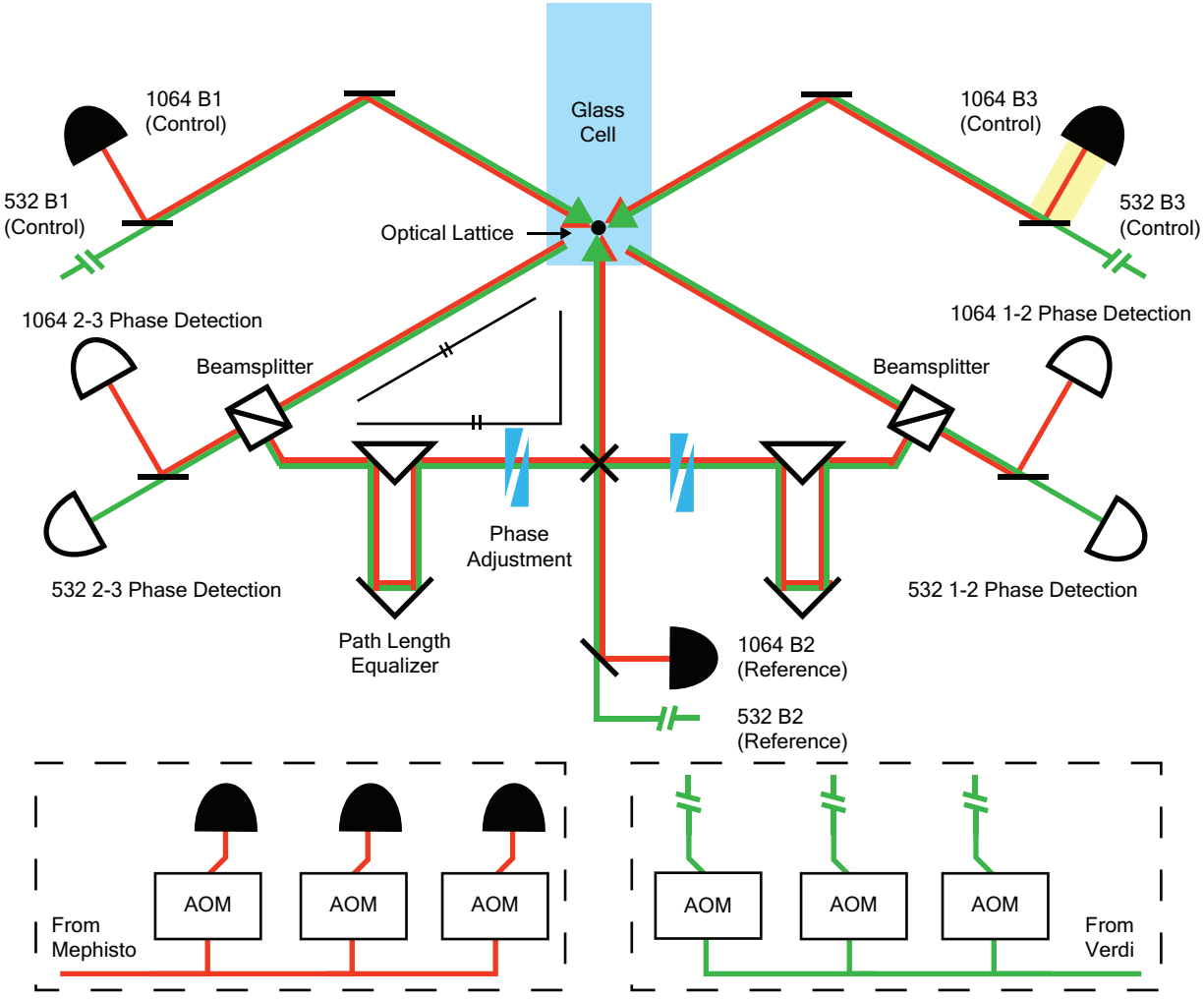

Figure 4.1: Overview schematic of the optical lattice and stabilization scheme. Three 532 nm wavelength beams (green) are derived from a Coherent Verdi (right inset), before passing through acousto-optic modulators (AOM) and are free space coupled towards the optical lattice. Three 1064 nm wavelength beams (red) are derived from a Coherent Mephisto (left inset), before passing through AOMs, and fiber coupled. The optical lattice is formed by the intersection of the six beams in the glass cell. B1 and B3 pass through the optical lattice and are interfered on beamsplitters with light sampled from B2. The 1064 nm interference signal is split from the 532 signal, before both are detected on photodetectors. The yellow highlight shows a region where path length changes cause relative displacement without feedback. The marked black lines show two path lengths that must be approximately equal.

where $V_{532}(\boldsymbol{r})$ and $V_{1064}(\boldsymbol{r})$ are the in-plane polarized or out-of-plane polarized potentials described in chapter 2. $\boldsymbol{\delta}_{532}$ and $\boldsymbol{\delta}_{1064}$ are displacements of these lattices with respect to a reference point in the lab. We note that displacing both of these lattices together does not change the geometry experienced by the atoms so we consider a reference frame in which the 532 nm potential minima are fixed, for which the potential takes the form

$$V(\boldsymbol{r}) = V_{532}(\boldsymbol{r}) + V_{1064}(\boldsymbol{r} - \boldsymbol{\delta}) \tag{4.2}$$

where $\boldsymbol{\delta} = \boldsymbol{\delta}_{532} - \boldsymbol{\delta}_{1064}$. Our goal is to control these two displacements $\boldsymbol{\delta}_{532}$ and $\boldsymbol{\delta}_{1064}$ such that $\boldsymbol{\delta} = 0$ or $a\left(\frac{1}{2\sqrt{3}}, 0\right)$, realizing the potentials described in chapter 2. In this section we will show how applying boundary condition of the electric field to both the 1064 nm and 532 nm light at the same point in space allows us to ensure a stable, and controllable relative displacement of the two triangular potentials.

To see how the relative displacement of the two triangular lattices is initially uncontrolled, consider a schematic of how the lattices are formed in figure 4.1. The optical lattice is formed by the intersection of three pairs of beams at 120° in the glass cell, with 532 nm and 1064 nm light making up each pair. The three beams of each wavelength, labeled B1, B2 and B3, are derived from the same laser source, but the 532 nm and 1064 nm sources are independent of each other, with $\lambda_{1064} \approx 2\lambda_{532.}$.

Consider a change in length of 1064 nm B3 path before it is combined with 532 nm B3, as highlighted in yellow. Perhaps this is due to a vibration of a mirror, or a thermal drift of the optical fiber length. This changes the phase of the 1064 nm B3, which displaces the 1064 nm triangular lattice. As the 532 nm lattice is not displaced, there is a relative displacement between the lattices and the underlying geometry changes. However if the path length changes occurs after the 1064 nm B3 is combined with 532 nm B3, in a non-dispersive way, both lattices are displaced by equal amounts, which causes no change in the geometry.

Having recognized that common mode path length changes do not change the geometry, we describe our stabilization scheme. After B1 and B3 pass through the optical lattice they are interfered with light picked off from B2, as shown in figure 4.1, and the relative phase detected on a photodiode. By applying feedback to the frequency or phase of B1 532 nm, we can enforce a boundary condition at the beamsplitter on which they are combined: that the intensity is maximum, and the beams are in phase. We apply the same phase relationship between B1 and B2 1064 nm. If the path length from the beamsplitter to the optical lattice along B1 and B2 are common for both colors of light, the phase relationship between the beams at the optical lattice is the same as the phase relationship at the beamsplitter.

By applying similar feedback to B3 1064 nm and B3 532 nm, we fix the four free phases in the intensity pattern of the optical superlattice, and such stabilize the relative displacement of the two triangular lattices.

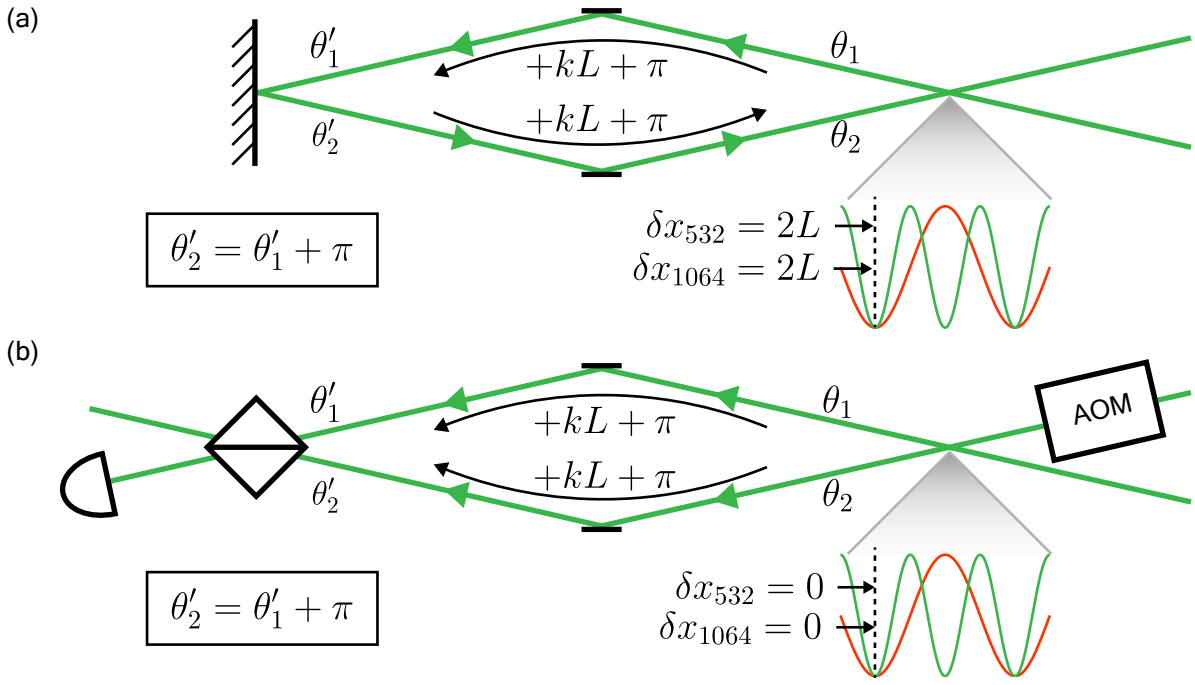

Figure 4.2: Comparison of retroreflection and feedback schemes. (a) A deformation of the traditional retroreflection superlattice scheme. The mirror on the left enforces a relationship between the phase of the incoming and outgoing beams. The propagation phases (black arrows) relate the phases at the mirror to those at the optical lattice. The relative displacement of the optical lattice potentials is shown. A change in the path length L shifts both lattices by equal amounts. (b) A single arm of our phase stabilization scheme. The relative phase at the beamsplitter is detected on a photodiode, and feedback to an AOM enforces a phase relationship. The phases at the optical lattice are related to the phases at the beamsplitter by propagation and reflection (black arrows). The relative displacement of the optical lattice potentials is shown. A change in the path length does not change the relative displacement.

Single arm interferometer

In our stabilization scheme detailed above there are two identical interferometers, one which fixes the B1-B2 phases for both wavelengths, and one which fixes B3-B2 phases. As these are simply copies of each of each other, we focus on one to compare it to existing optical superlattice experiments.

In cold atom optical superlattice experiments at Munich, MIT and more [72, 44], an optical superlattice is formed by retroreflecting light of wavelengths λ and 2λ. In figure 4.2(a), we show an almost identical scheme, where a superlattice is formed by reflecting a beam off three mirrors before interference with itself. This is simply a slight deformation of the retroreflection superlattice schemes, which will allow us to see the similarities between

our scheme, and the retroreflection scheme.

The phase relationship between the left propagating 532 nm beam, and the right propagating beam is fixed by the reflection at the leftmost mirror. The intensity must go to zero, so the phase of the left propagating beam θ_1' and the right propagating beam θ_2' at the mirror satisfy $\theta_2' = \theta_1' + \pi$. The phase of the two beams at the interference point θ_1 and θ_2 are simply related to those at the boundary θ_1' and θ_2' by propagation through length L and another reflection, giving us

$$\theta_2 = \theta_1 + 2kL + 3\pi. \tag{4.3}$$

This is equally true for the 1064 nm beam. If we calculate the locations of the minima of each lattice, relative to where they would occur if $L = 0$, we see that the shift is the same for both lattices,

$$\delta_{532} = 2L \tag{4.4}$$

$$\delta_{1064} = 2L. \tag{4.5}$$

Thus even if the distance to the mirror L drifts, the relative displacement of the two optical lattices is fixed.

Our feedback scheme works in a similar manner. Just as with the mirror in the previous scheme, a boundary condition is enforced at the beamsplitter in figure 4.2(b), where the two beams are interfered. Our feedback typically maximizes the intensity of the electric field, setting the relative phase between the beam 1 and beam 2 after the beamsplitter to zero. However one of the beams picks up a π phase shift from reflection off the beamsplitter, giving us the phase relationship before the beamsplitter $\theta_2' = \theta_1' + \pi$. Again, the phases at the optical lattice θ_1 and θ_2 are simply related to the phases θ_1' and θ_2' before the beamsplitter by propagation and reflection, noting the different direction of beam propagation. At the optical lattice we have the fixed phase relationship:

$$\theta_2 = \theta_1 + \pi, \tag{4.6}$$

which is independent of the path length L. As this relationship is true for both wavelengths, the relative displacement is fixed.

Ultimately, these two schemes work in similar manner: a phase relationship is enforced somewhere in space, either by a mirror or feedback. Common mode propagation of the two wavelengths thus relates the phases of the interfering beams to those where the phase relationship is established, producing an optical lattice geometry that is independent of the propagation length L.

Deviations from ideal implementation

To examine how this scheme for stabilizing the relative displacement of the two triangular lattices might work in practice, let us separate the problems into two types: imperfections in

setting the relative phase at the beamsplitter, and deviations of the relative phase between the beamsplitter and optical lattice. The subject of the rest of this chapter will be the phase-locked loop implementation to address this first imperfection, but in this section we will address the second imperfection.

Wavelength and path-length difference

The two lasers that produce our 532 nm and 1064 nm beams, a Coherent V18 Verdi and a Coherent Mephisto MOPA respectively, do not have a fixed phase or frequency relationship to each other. The phase relationship is unimportant as the two wavelengths never interfere, so we consider the effect of a change in frequency of one laser by Δf.

We also assume that path lengths, shown as black lines in figure 4.1 between the beamsplitter and optical lattice are not equal, and have a difference ΔL. The change in frequency results in a phase shift between the two interfering beams $\phi = \theta_1 - \theta_2$ at the optical lattice of

$$\phi = \frac{2\pi}{c}\Delta L \Delta f. \tag{4.7}$$

In the triangular lattice configuration, a phase shift of ϕ displaces the lattice by

$$|\delta| = \frac{\phi}{2\pi}\frac{2\lambda}{3}, \tag{4.8}$$

where λ is the wavelength of the relevant lattice. Thus the frequency shift of the source laser Δf displaces the lattice it produces by an amount

$$|\delta| = \tfrac{2}{3}\lambda\frac{\Delta f}{(c/\Delta L)}. \tag{4.9}$$

When $\Delta L = 0$ the interferometer satisfies the 'white light condition', where the position of the minima are independent of the wavelength, as seen by the fact that $|\delta| = 0$. We note however that this condition occurs only at one point in space, not over the entire optical lattice, so the collinearity and wavelength requirements described in chapter 2 are still required. In figure 4.1 we demonstrate which path lengths must be the same as black lines. To balance the path lengths, we place knife-edge right-angle mirrors, and retroreflecting mirrors in the path of the pickoff paths from B2 (labeled path length equalizer in figure 4.1). These are currently adjusted by eye to minimize the path length difference, and so we conservatively estimate the difference $\Delta L = 3$ cm. The effect of this path length difference is shown in table 4.1.

$c/\Delta L$	$\Delta\dot{f}_{1064}$	$\lvert\dot{\delta}_{1064}\rvert$	$\Delta\dot{f}_{532}$	$\lvert\dot{\delta}_{532}\rvert$
10 GHz	$<$ 10 MHz/hr	$<$0.4 nm/hr	100 MHz/ hr	3.5 nm /hr

Table 4.1: Estimated drift rates of the 1064 nm ($\Delta\dot{f}_{1064}$) and 532 nm ($\Delta\dot{f}_{532}$) laser frequencies and the corresponding relative displacement drift rates of the 1064 nm ($|\dot{\delta}_{1064}|$) and 532 nm ($|\dot{\delta}_{532}|$) triangular lattices .

Clearly the large drift rate of the 532 nm source is a problem, suggesting a drift in the geometry of 1 nm every 20 minutes. This is consistent with our observation that superlattice requires very regular realignment of the relative displacement.

Vibrations and path length changes

Vibrations and path length drifts greater than a few nanometers are unavoidable in our optics. However by examining where a change in path length occurs, and for which wavelengths, we can understand the effect of these phase shifts on our lattice geometry. Path length changes occur in one of two positions: upstream of the optical lattice, or between the optical lattice and beamsplitter. Path length changes are also of two types, common mode shifts that change the path length equally for both wavelengths, or dispersive shifts that change the path length differently for the two wavelengths.

	Upstream of Lattice	Between Lattice and Beamsplitter
Common Mode	Both lattices returned by feedback	Lattices drift together
Dispersive	Both lattices returned by feedback	Lattices drift apart

Table 4.2: Comparison of different types of path length changes, and their effect on the stabilized lattice. Dispersive shifts between the lattice and beamsplitter cause a change in lattice geometry, all other drifts do not.

The effects of these path length changes are summarized in table 4.2. All of the path length changes upstream of the optical lattice are canceled by feedback, dispersive or not. Common mode path length changes between the beamsplitter and optical lattice move the absolute position, but leave the geometry unchanged. We do note that heating of the atoms may be caused by this type of absolute motion.

The worst type of shift are dispersive shifts between the optical lattice and beamsplitter, as these distort the geometry. To minimize dispersive shifts we try to place as few

transmissive optics between the beamsplitter and optical lattice as possible. The refractive index of most common optics is temperature dependent, and so changes in the temperature induce dispersive phase shifts. Even the dispersion of the air changes with temperature and atmospheric pressure.

Dispersion of Air

We estimate the effect of a varying temperature or pressure of air on the relative displacement δ of the two triangular optical lattices. The dependence of the index of refraction n of air on temperature, atmospheric pressure and relative humidity can be calculated with a modified version of Edlén equation for the dispersion of air at standard temperature and pressure [6]. The explicit dependence of the refractive index on these parameters is complicated and so will not be quoted here. Instead we refer the reader to a useful calculator maintained by NIST [61].

We calculate the refractive index of air for 532 nm (n_{532}) and 1064 nm (n_{532}) at 20 °C , 101.325 kPa and 50% relative humidity, as shown in table 4.3. These same quantities were then calculated under the same conditions, except for an increase in the temperature by 1 °C or a decrease in the pressure of 1 kPa. This level of temperature change does occasionally occur in our temperature controlled lab, and a 1 kPa = 10 mbar atmospheric pressure change corresponds to a moderate low pressure weather system. As the change in the difference in refractive indices $n_{532} - n_{1064}$ occurs along both paths between the optical lattice and beamsplitters, the change in relative displacement of the optical lattices δ, only depends on the path length difference ΔL as

$$\delta = (n_{532} - n_{1064})\Delta L. \tag{4.10}$$

Treating the $20°C$, 101.325 kPa case as a reference, we find the relative displacement due to a 1 °C change in temperature for an estimated $\Delta L = 3$ cm path length difference to be $\delta = 0.42$ nm. For a change of 1 kPa, the relative displacement is 50 nm. It must be noted that our superlattice implementation scheme is much less sensitive to these type of temperature and pressure changes than the retroreflection implementation. Our path length difference is $\Delta L = 3$ cm, whereas in retroreflected superlattices ΔL is twice the distance between the optical lattice and the retroreflection mirror, often as much as 1 m. We conclude that temperature shifts of 1 °C are not particularly significant to the stability of the lattice geometry, but pressure changes of 1 kPa, or even 0.1 kPa are. Further reductions in the path length difference would reduce this sensitivity further.

Temperature (°C)	Pressure (kPa)	$n_{532} - 1$	$n_{1064} - 1$	$n_{532} - n_{1064}$ (μm/m)	$\lvert\delta x\rvert$ (nm)
20	101.325	2.73028×10^{-4}	2.68867×10^{-4}	4.161	0
21	101.325	2.7207×10^{-4}	2.67923×10^{-4}	4.147	0.42
20	100.325	2.68691×10^{-4}	2.66209×10^{-4}	2.482	50

Table 4.3: Refractive indices of air at 532 nm (n_{532}) and 1064 nm (n_{1064}), calculated with [61]. The dependence of the refractive indices of air on temperature and pressure near 20 °C and 101.325 kPa is shown. The difference in refractive indices is quoted in μm/m for convenient path length difference calculations. Displacement of the two triangular optical lattices is shown relative to 20° and 101.325 kPa for a path length difference of $\Delta L = 3$ cm.

Control

There is one exception to our aversion to dispersive optics: a pair of glass wedges that we use to control the relative phase between the optical lattice and the beamsplitter. An actuator pushes one wedge with respect to another, providing a variable thickness dispersive piece of glass, without any displacement of the beams. The exact details of this control are given in Claire Thomas's thesis, but experimentally we find a 0.8 mm displacement of the wedges shifts the relative phase of the 532 nm and 1064 nm lattices by a full period.

4.2 Phase-locked loops

Throughout the rest of this chapter, we will describe the electro-optical system that enforces the zero phase difference at the beamsplitters. Whilst we detect the relative phase of two beams, we will feed back to the frequency one of the beams. This type of feedback is known as a phase-locked loop, which is a common component of many radio-frequency devices. To utilize some of the existing understanding about PLLs, we introduce a small amount of feedback theory to point to key results that guide the construction of our system.

Feedback theory

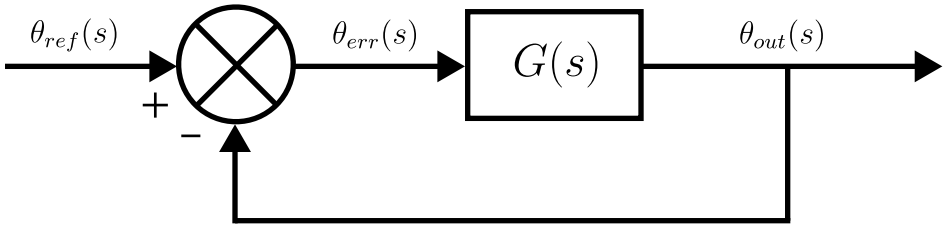

Figure 4.3: Block diagram of a general feedback loop. The filter $G(s)$ relates the difference between the reference phase $\theta_{ref}(s)$ and the output phase $\theta_{out}(s)$ to the output phase $\theta_{out}(s)$.

We examine the problem of controlling and stabilizing the relative phase of the two laser beams through the framework of linear time invariant feedback [3]. In this approach, we think of the electric and optical components of our feedback system as a filter $G(s)$ that relates the phase of a reference beam $\theta_{ref}(s)$ to the phase of a beam under control $\theta_{out}(s)$, by acting on their phase difference $\theta_{err}(s) = \theta_{ref}(s) - \theta_{out}(s)$. This is drawn schematically in figure 4.3. As is typical in control theory these variables and filters are formulated in the Laplace domain, where $\theta(s) = \int \theta(t)e^{-st}dt$. We recover our familiar frequency domain picture simply by the substitution $s \to i\omega$. Our goal is to design $G(s)$ to minimize the phase error $\theta_{err}(s)$, which is given in terms of the reference phase as

$$\theta_{err} = \frac{1}{1 + G(s)}\theta_{ref}. \tag{4.11}$$

If the phase of the reference beam changes, for example by vibration or drift, then the phase error is the reference phase filtered by $1/(1 + G(s))$. If we want our control beam to accurately track the phase of the reference beam at low frequencies for example, then we want the magnitude of $G(s)$ to be large at low frequencies.

Phase-locked loop

A phase-locked loop is a feedback system, shown in figure 4.4, where $G(s)$ consists of three parts: a phase detector, a loop filter and a voltage controlled oscillator [52]. The phase detector converts the phase difference between the two optical beams to a voltage

$$V_{PD} = K_D\theta_{err}(s), \tag{4.12}$$

with gain K_D. The second section is the loop filter $F(s)$, which is the feedback circuit that we design. The voltage after the loop filter is

$$V_F = F(s)V_{PD}. \tag{4.13}$$

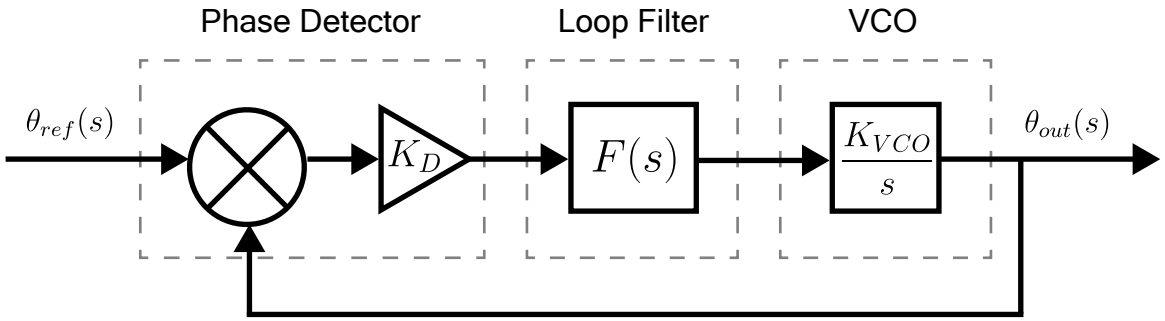

Figure 4.4: Block diagram of a phase-locked loop. The filter $G(s)$ consists of a phase detector, loop filter and voltage controlled oscillator (VCO).

Finally, a voltage controlled oscillator (VCO), converts this voltage into a sinusoidal waveform, which in our case is the optical beam under control. The voltage controls the frequency of the oscillator, not the phase. As the frequency is the derivative of the phase $f(t) = d\theta(t)/dt$, the phase out of the VCO takes the Laplace form

$$\theta_{out}(s) = \frac{K_{VCO}}{s} V_F, \tag{4.14}$$

where K_{VCO} is the VCO gain.

Theoretical results to consider

Steady state limits

We will quote a few theoretical results which are particularly significant to the stabilization of the optical phase. We first use the Final Value Theorem to calculate the steady state error of the system for particular changes of the reference beam. This theorem tells us the steady state error is [22]

$$\lim_{t\to\infty} \theta_{err}(t) = \lim_{s\to 0} s\theta(s). \tag{4.15}$$

If the reference beam undergoes a step change in the phase, represented as $\theta_{ref}(s) = \frac{\Delta\theta}{s}$, the steady state error is

$$\lim_{t\to\infty} \theta_{err}(t) = \lim_{s\to 0} \frac{\Delta}{1 + K_{VCO}K_D F(s)/s}. \tag{4.16}$$

As long as the loop filter $F(s)$ is non-zero as $s \to 0$, then the steady state error is zero. This gives us our first requirement on the loop filter $F(s)$. For example this requirement is easily satisfied by a proportional gain filter $F(s) = K_P$. If the phase of reference beam begins to drift at a constant rate $\Delta\omega$, then $\theta_{ref}(s) = \frac{\Delta\omega^2}{s^2}$, and the steady state error is [22]

$$\lim_{t\to\infty}\theta_{err}(t) = \lim_{s\to 0}\frac{\Delta}{s + K_{VCO}K_D F(s)}. \tag{4.17}$$

For this to be zero, $F(s)$ must scale at least as $\frac{1}{s}$ as $s \to 0$. This gives us a second requirement on the loop filter. Both of these requirements would be satisfied by a proportional-integral controller such as

$$F(s) = K_P + \frac{K_I}{s}. \tag{4.18}$$

Noise

We consider noise $\delta V_F(s)$ entering right before the VCO such that $V_F \to V_F + \delta V_F(s)$, and calculate the response of the system to this noise. This represents electronic noise in the output of the loop filter electronics. The output phase is given by

$$\theta_{out}(s) = \frac{K_{VCO}}{s}V_F = \frac{K_{VCO}}{s}\left(F(s)K_D\theta_{err}(s) + \delta V_F(s)\right). \tag{4.19}$$

We are interested in the response of θ_{out} to $\delta V_F(s)$ and not to $\theta_{in}(s)$, so we let $\theta_{in}(s) = 0$ giving us

$$\theta_{out}(s) = -\frac{K_{VCO}}{s}F(s)K_D\theta_{err}(s) + \frac{K_{VCO}}{s}\delta V_F(s). \tag{4.20}$$

By rearranging this, we find the dependence of $\theta_{out}(s)$ on $\delta V_F(s)$ to be,

$$\frac{\theta_{out}(s)}{\delta V_F(s)} = \frac{K_{VCO}/s}{1 + K_D F(s)K_{VCO}/s} = \frac{K_{VCO}/s}{1 + G(s)}. \tag{4.21}$$

As the overall gain of $G(s)$ is set by stability considerations later on, the only free parameter here is K_{VCO}. Thus, if we increase $K_D F(s)$ and decrease K_{VCO}, keeping $G(s)$ constant, we reduce our sensitivity to this type of noise. If we were also to imagine noise $\delta V_{PD}(s)$ entering right before the loop filter such that $V_{PD} \to V_{PD} + \delta V_{PD}(s)$, we can conduct a similar type of analysis. This noise represents electronic noise on the output of the phase detector electronics, or electronic noise on the input of the loop filter electronics. We find the dependence of $\theta_{out}(s)$ on the noise $\delta V_{PD}(s)$ as

$$\frac{\theta_{out}(s)}{\delta V_{PD}(s)} = \frac{F(s)K_{VCO}/s}{1 + G(s)}. \tag{4.22}$$

Thus maximizing K_{PD} and minimizing $F(s)K_{VCO}$ minimizes the effect of this type of noise. These two results tell us to minimize K_{VCO} and maximize the phase detector gain [15].

4.3 Phase detection

The phase detector consists of two optical beams that are combined on a beamsplitter, and interfered on a photodiode, where we make a lock-in detection of the phase.

The frequencies of interest for phase detection range from DC to 10s of kHz. Unfortunately, this is a frequency range where amplitude noise is present on our optical beams, which can obscure the phase information. To make a measurement of the phase free of amplitude noise, we perform lock-in detection: we modulate the phase of one beam well above the frequencies contaminated by amplitude noise, and then demodulate the electrical signal from the photodiode.

Alternatively, we could have suppressed the amplitude noise by using a balanced homodyne receiver. Splitting the signal with a 50:50 beamsplitter and measuring both output ports with equal gain on a photodetector would allow us to subtract the signals and remove the amplitude noise. This would yield a significantly larger signal, but would have to be balanced manually to avoid issues with autobalance during the lattice loading. Manually balanced homodyne would be subject to drifts.

In this section we will explain our phase detection scheme in detail, and derive an expression for the phase detector gain K_D.

Overview

An overview of the electrical and optical systems that comprise one of the four phase detection systems is shown in figure 4.5, choosing a 532 nm path as an example. The reference beam, B2, is modulated by an electro-optic modulator. This beam is interfered with a small amount of power is picked off B1 or B3 after they have passed through the optical lattice. The two beams are combined on a non-polarizing beamsplitter with their 1064 nm counterparts, aligned to maximize the interference. A dichroic mirror separates the 1064 nm light from the 532 nm light.

The interference signal is detected on a photodetector before the signal is high-pass filtered to remove the amplitude noise contaminated low frequency components. This signal is then amplified by a variable gain amplifier, before being demodulated and low pass filtered to create the final signal V_{PD}.

Calculation of the phase detector gain K_d

Consider the perfect interference of two laser beams of equal carrier frequency ω and power P on a photodetector. The total electric field at the photodiode $E(t)$ is the sum of the electric fields $E_1(t)$ and $E_2(t)$ of the two laser beams. Generally the field of the first laser beam phase may have modulation of frequency ω_M and modulation depth M, taking the form,

$$E_1(t) = E_0 e^{i\omega t + iM\sin(\omega_M t)}. \tag{4.23}$$

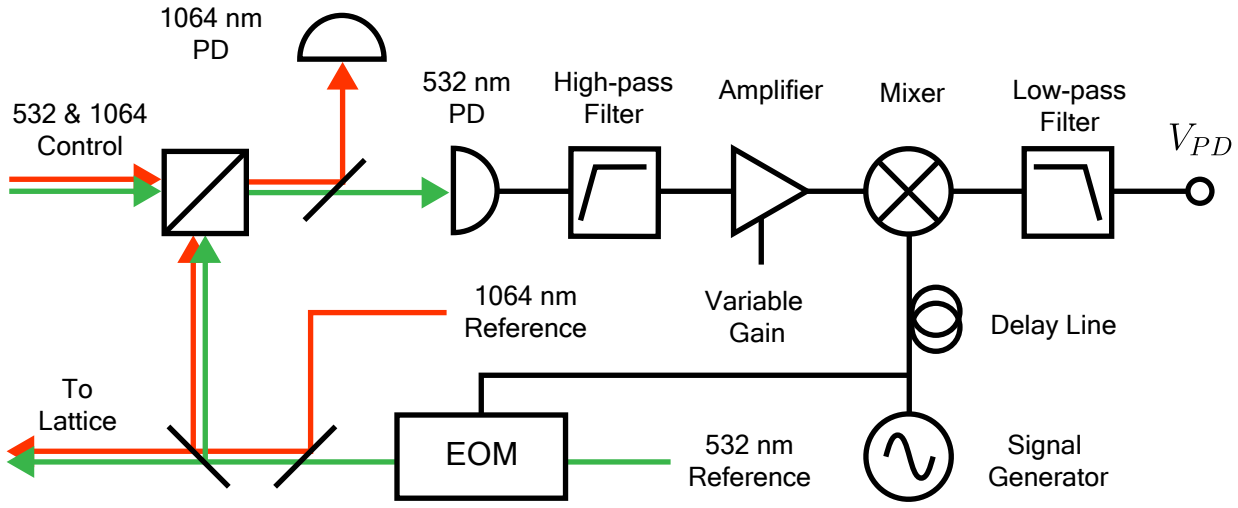

Figure 4.5: An overview of the components of the 532 nm phase detector. An electro-optical modulator (EOM) modulates the reference 532 nm beam. The reference and control beams of both 1064 nm (red) and 532 nm (green) are then combined on a beamsplitter before being detected on separate photodiodes. The electrical signal (black lines) is filtered and amplified before being demodulated. After a low pass filter, a signal is produced proportional to the phase difference (for small phase differences). We note that the stabilization of the 1064 nm light follows a similar scheme, and the components used are not shown in this figure for clarity.

For small modulation depths, this is approximately

$$E_1(t) = E_0 e^{i\omega t} \left(1 + iM \sin(\omega_M t)\right). \tag{4.24}$$

The second electric field has an arbitrary relative phase θ to the first electric field,

$$E_2(t) = E_0 e^{i\omega t + i\theta}. \tag{4.25}$$

The photocurrent on the photodetector is determined by the optical power P incident on the photodiode, and its responsivity R,

$$I = RP_{total} = R|\sqrt{P}\left(1 + iM \sin(\omega_M t)\right) + \sqrt{P}e^{i\theta}|^2. \tag{4.26}$$

We assume the frequency response of the photodiode is flat for the modulation frequencies we consider. After a transimpedance amplifier of gain R_f in V/A, the voltage produced by the photocurrent is given to linear order in the modulation depth M,

$$V = R_f RP\left(2 + 2\cos(\theta) + 2M \sin(\omega_M t)\sin(\theta)\right). \tag{4.27}$$

A high pass filter removes the DC components, after which we apply amplification G_{RF} :

$$V = 2MG_{RF}R_fRP\sin(\omega_M t)\sin(\theta). \tag{4.28}$$

Demodulating this signal by mixing it with $\sin(\omega_M t)$ at the appropriate local oscillator power gives

$$V = MG_{RF}R_fRPG_m\sin(\theta)\left(1-\cos(2\omega_M t)\right). \tag{4.29}$$

where G_m is the conversion gain of the mixer. Low pass filtering once more gives us

$$V = MG_{RF}R_fRPG_m\sin(\theta), \tag{4.30}$$

which for small θ, allows us to derive K_d:

$$K_D = MG_{RF}R_fRPG_m. \tag{4.31}$$

We will not use this equation to calculate the exact phase detector gain; we will just calibrate K_D directly. However, this equation has been useful to understand how to produce a large phase detector gain K_D, to minimize the overall noise. Each of the components in this chain could potentially be improved, and this equation clearly identifies their contribution to the final signal.

Specific components

Electro-optic modulators

An electro-optic modulator is used to phase modulate each of the 1064 nm and 532 nm reference beams (B2). The 532 nm beam is modulated by a non-resonant LINOS phase modulator (LM0202 5W VIS) driven by an SRS function generator (SRS DS350) amplified by a LINOS High Voltage Amplifier (LAV 400). The 1064 nm beam is modulated by a resonant modulator (Newport EO-PM-R-C2), driven by an SRS function generator (DS345). The drive frequencies and modulation depths are shown in table 4.4.

λ	Modulator	V_π	Drive	Modulation Depth	Power loss	Frequency
532 nm	LM0202 5W VIS	175V	$13V_{PP}$	0.1	0.4%	700 kHz
1064 nm	EO-PM-R-C2	24V	$8V_{PP}$	0.3	5%	20 MHz

Table 4.4: Details of the electro-optic modulators used for 532 nm and 1064 reference beams.

Photodetectors

For the 532 nm interference signals, we use Si photodetectors, namely the Thorlabs PDA36a with 10 dB of gain. Stray light is filtered by 532 nm bandpass filters. For the 1064 nm

interference signals, we use two InGaAs photodetectors, the Newport 1811. The beams are focused onto the small detector area, and stray light is filtered by a 1064 nm bandpass filter. For both of these photodetectors, the 3 dB bandwidth is much larger than the relevant modulation frequency. Further details of these photodetectors as relevant to the phase detector gain are shown in table 4.5.

Wavelength	1064 nm	532 nm
Photodetector	Newport 1811	Thorlabs PDA36a (10 dB gain)
Responsivity	0.75 A/W	0.22 A/W
Transimpedance Gain	40 V/mA	0.75 V/mA
Bandwidth	125 MHz	5.5 MHz

Table 4.5: Details of the photodetectors used to detect the 532 nm and 1064 nm interference signals.

High pass filter

The low frequencies are removed with a 300 kHz second-order high-pass filter. This home-made filter has a transmission loss of -1 dB, a 300 kHz -3 dB point, 20 dB/decade falloff for the first decade and 40 dB/decade afterwards. This gives -60 dB at 3 kHz, strongly suppressing the low frequency noise.

Variable gain amplifier

As we load our optical lattice, the optical power varies over many orders of magnitude. Given that we want optimal feedback parameters over the entire loading sequence, it is a problem that the phase detector gain K_D depends linearly on the optical power.

We keep the phase detector gain approximately constant over at least 3 orders of magnitude by applying variable gain amplification of the modulated signal. The optical power is stabilized by an additional feedback loop, with an exponential scaling in power $P(V_{CTRL}) \sim 10^{\alpha_{PD} V_{CTRL}}$, where $\alpha_{PD} = 2.5V^{-1}$ and V_{CTRL} is the control voltage. If we apply variable gain amplification of the following form $G(V) = 10^{-\alpha_{PD} V_{CTRL}}$, the phase detector gain is independent of the optical power. We use an Analog Devices 8330, mounted in the AD8330-EVALZ, which has a gain of the form $10^{\alpha_{VGA} V_{VGA}}$ where $\alpha_{VGA} = 1.67V^{-1}$. In theory, setting the VGA voltage as

$$V_{VGA} = \frac{\alpha_{PD}}{\alpha_{VGA}} V_{CTRL} = 1.5 V_{CTRL} \tag{4.32}$$

should ensure the appropriate scaling. This is not precisely true in practice, and as such the phase detector gain varies by a factor of two over the loading sequence. This is sufficient for our purposes.

Phase detector

In equation 4.27, we demodulate in phase with the detected signal, so we split the signal from the EOM driver at 0° phase. As some delay is accumulated in the EOM itself, we use a delay line to optimally demodulate the signal. We find an optimal delay of 128 ns for the 532 nm path, which is a 0.1π phase shift. For the 1064 nm path we use a 64 ns delay, which is a 2.5π phase shift. The demodulation is done by a Minicircuits ZRPD-1 phase detector.

Low pass filter

The final low pass filter is a Thorlabs EF502, with a 100 kHz bandwidth.

Calibration

In principle the phase detector gain can be calculated from equation 4.31, but in practice the presence of power imbalances and imperfect interference makes this a tedious task. Much better is to simply measure the phase detector gain.

The choice of Keysight function generators for VCOs described in a later section make this an easy task. With the frequency modulation inactive, we simply increase the frequency of the VCO used for feedback by 1 kHz. The phase thus evolves at 1 kHz, which allows us to measure the peak-to-peak voltage directly out of the phase detector. Thus we have

$$K_D = \frac{V_{PP}}{2}. \tag{4.33}$$

This relationship breaks down if any part of the phase detection becomes non-linear, which can easily be seen as deviations from a sinusoidal phase relationship. The exact phase detector gain depends on the final alignment of the beam, and so varies. An example calibration of the phase detector gain is shown in table 4.6.

λ	B1-B2 Error signal	1-2 K_D	B2-B3 Error signal	2-3 K_D
532 nm	0.96 V_{pp}	0.48 V/rad	1.40V_{pp}	0.7 V/rad
1064 nm	1.00 V_{pp}	0.5 V/rad	1.04V_{pp}	0.52 V/rad

Table 4.6: Final phase detector gain settings for data taken August 2018. The peak-peak error signal is measured directly from an oscilloscope.

4.4 Voltage controlled oscillator

In our optical phase-locked loop, the entire VCO system consists of all of the parts required to make a frequency tunable laser beam, shown in figure 4.6. We use an acousto-optic modulator (AOM) to shift the frequency of a laser beam derived from the same source as the reference beam. This AOM is driven by an amplified radio-frequency voltage controlled

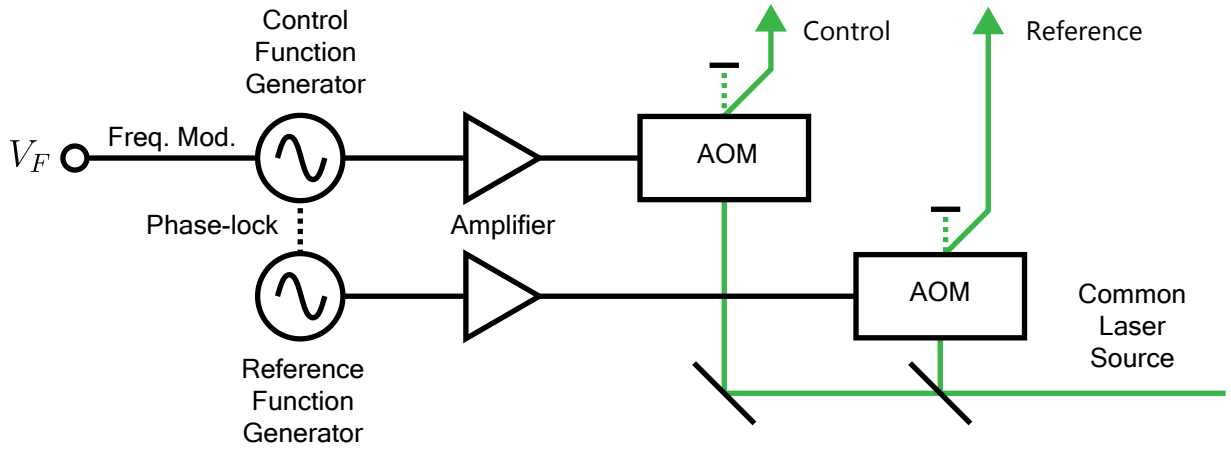

Figure 4.6: An overview of the components of one of the 532 nm voltage controlled oscillators. The control and reference beams (green) are generated by the first-order diffraction of two acousto-optic modulators, and are derived from a common source. The radio-frequency signals that drive the two AOMs come from amplified function generators, with their master oscillators phase-locked. The control function generator is frequency modulated by the output of the loop filter V_F.

oscillator, and the frequency shift of the laser beam is just the frequency of the RF VCO. The frequency of the reference beams are also shifted by AOMs which are driven by RF VCOs that are internally phase referenced to the RF VCOs of the control beams.

By deriving the laser beams from the same source, and driving the acousto-optic modulators with phase-referenced RF VCOs, we prepare the control beams as close to the reference beam in frequency and phase as possible. Drifts of the laser frequency and phase are common to both beams, and relative drifts of the RF VCOs are eliminated by the internal phase lock. As a result, the feedback system only needs to minimize differential phase shifts introduced by the optics. We initially built this system without phase referenced RF VCOs, which introduced a significant amount of extra noise.

Acousto-optic modulators

We use the first order diffraction of an acousto-optic modulator in the single pass configuration for all six beams that make up the optical lattice. Details of the acousto-optic modulators used are given in table 4.7. The frequency response of the acousto-optic modulator depends strongly on the specifics of the implementation, as the angle of the diffracted light changes with frequency. We estimate the bandwidth of the single pass acousto-optic modulator as 1 MHz, with a delay given by the rise time of 200 ns.

	Model	Central Frequency	Rise time
532	Gooch & Housego 3080-292	80 MHz	230 ns
1064	Gooch & Housego 3110-197	110 MHz	200 ns

Table 4.7: Details of the acousto-optic modulators used to shift the frequency of the reference and control beams.

Function generator as VCO

A significant decision in the design of this phase-locked loop was the choice of radio-frequency voltage controlled oscillator. Of particular importance is the choice of the VCO gain K_{VCO}, which involves a trade-off between phase noise and the capture range of the PLL [22]. The capture range is the range of initial frequencies of the reference beam that the control beam can lock on to. As the reference beam has a permanently fixed frequency, the capture range is not an important parameter to us, and as such the lower K_{VCO}, the smaller the phase noise, as we saw in section 4.2.

Having identified K_{VCO} as a critical parameter of the PLL, we choose an RF VCO where K_{VCO} is tunable. We use a frequency modulated function generator (Keysight 33512 A&B) as our VCO, where the widely tunable frequency deviation parameter F_{dev} sets K_{VCO} as

$$K_{VCO} = \frac{2\pi \cdot \text{frequency deviation (Hz)}}{\text{modulation input range (V)}}. \tag{4.34}$$

The frequency deviation can be tuned from 1 uHz to 40 MHz, allowing us to effectively choose an arbitrary K_{VCO}. This freedom inspires us to perform the final tuning of the overall gain of the PLL by simply tuning the frequency deviation. By maximizing the gain of the phase detector and loop filter to fully utilize the input dynamic range of the frequency modulation port, we ensure the phase noise is minimal regardless of the final gain parameters.

By choosing a function generator as an RF VCO we gain an additional benefit: the frequency modulated function generator can easily be referenced to an additional function generator that drives the reference beam. This referencing completely removes relative drifts of the two oscillators, and ensures that a zero input into the control VCO produces zero frequency difference between the oscillators. Another benefit is the ability to apply a controlled frequency difference between the control and reference beams when feedback is turned off.

One downside that must be noted is the extra loop delay that is accumulated by using these function generators as VCOs. The modulation voltage is digitally converted into a frequency modulation, which is estimated by a Keysight engineer to add a $\tau = 4$ μs delay. As a result, we ignore the bandwidth and delay of the AOM and model the entire VCO system as

$$K_{VCO}e^{-\tau s}, \tag{4.35}$$

where the K_{VCO} parameter is determined by the frequency deviation as equation in 4.34.

4.5 Loop filter

The last element to analyze is the loop filter, which is the box of electronics that provides the feedback signal. The design of this filter requires that the overall feedback loop is stable.

Feedback system stability

In our model of negative feedback, perturbations in the system are damped by the feedback process. The output is subtracted from the input before being filtered by the loop, which then produces an output closer to the input than before. However if the phase between the input and the output at a given frequency grows to 180°, the output is effectively added to the input, and a runaway process begins if the gain is larger than 1 at that frequency. To avoid this instability, we require that the magnitude of the open loop gain $|G(i\omega)|$ is less than 1, when the phase $\arg G(i\omega)$ reaches 180° [3]. We characterize how close the system is to this instability, either in phase or gain. The gain margin is how much more proportional gain the system can take before becoming unstable,

$$\text{Gain Margin} = \frac{1}{|G(i\omega_{180})|} \tag{4.36}$$

where ω_{180} is the frequency at which a phase shift of 180 degrees occurs. The phase margin is how much more additional phase can be accumulated at the 0 dB gain frequency ω_{0dB}

$$\text{Phase Margin} = 180° - \arg(G(i\omega_{0dB}). \tag{4.37}$$

Rules of thumb suggest gain margins of at least 2, and phase margins of at least 45° for stable systems [3].

Loop filter conditions

The requirement that our system has no steady state errors either due to a reference phase shift or a continuous drift of the reference phase requires that the loop take the form of a proportional-integral controller:

$$K(s) = K_P + \frac{K_I}{s} \tag{4.38}$$

where K_p is the proportional gain, and K_I is the integral gain. Thus the open loop transfer function of the PLL, including the delay of the VCO is

$$G(s) = K_D(K_P + \frac{K_I}{s})\frac{K_{VCO}}{s}e^{-\tau s}. \tag{4.39}$$

Let us first assume that at high frequency where the delay $e^{-\tau s}$ causes phase accumulation, we can ignore the integrator. Thus at large ω

$$G(i\omega) \approx -iK_P K_P \frac{K_{VCO}}{\omega} e^{-\tau i\omega}. \tag{4.40}$$

The $1/s$ behavior of the VCO gives the system a 90 degree phase shift. Thus the frequency at which the system accumulates a 180 degrees phase shift is given by $\arg(e^{-\tau i\omega_{180}}) = \pi/2$, which yields

$$\omega_{180} = \frac{\pi}{2\tau} = 2\pi \cdot 63\,\text{kHz}. \tag{4.41}$$

For stability we require

$$K_p K_{VCO} < \frac{\omega_{180}}{K_D}. \tag{4.42}$$

In practice, we choose the proportional gain to maximally use the dynamic range of our system, and tune the overall gain with K_{VCO}. As the phase detector maximally produces a 2 V_{pp} signal, and the 33621A allows a maximum 10 V_{pp} input to the frequency modulation port, the maximum proportional gain is 5. In practice we design our system around a maximum proportional gain of 4, which requires

$$K_{VCO} < 2\pi \cdot 16\ \text{kHz}/V \tag{4.43}$$

for stability. In terms of the frequency deviation for a 5V amplitude signal

$$F_{dev} < 78\ \text{kHz}. \tag{4.44}$$

We wish to ignore the integrator at high frequencies, and so we require that the 'corner frequency ω_{PI} at which the loop filter changes from integral to proportional gain is substantially below ω_{180}. Thus we require,

$$\omega_{PI} = \frac{K_I}{K_P} \ll \omega_{PI}. \tag{4.45}$$

Loop filter implementation

The loop filter is implemented as a series of op-amps mounted on a PCB housed in a NIM rack. The PCB is a modification of a standard proportional-integral feedback design by Claire Thomas and Nathan Brahms.

An overview of the circuit is shown in figure 4.34, consisting of three sections. The first section is simply a buffer. The second section provides a fixed proportional gain $k_P = 0.4$ and a variable integral gain $k_I \in \{3\ \text{kHz}, 1\ \text{kHz}, 300\ \text{Hz}, 100\ \text{Hz}\}$. The variable integral gains are accessible via the blue switch on the front panel. A TTL level switch can be used to short the capacitors entirely, providing no integral gain. We keep the integrator off while the optical light level is either off or low to prevent the system from railing. During the first section of the optical lattice loading, proportional gain is sufficient to keep the phase

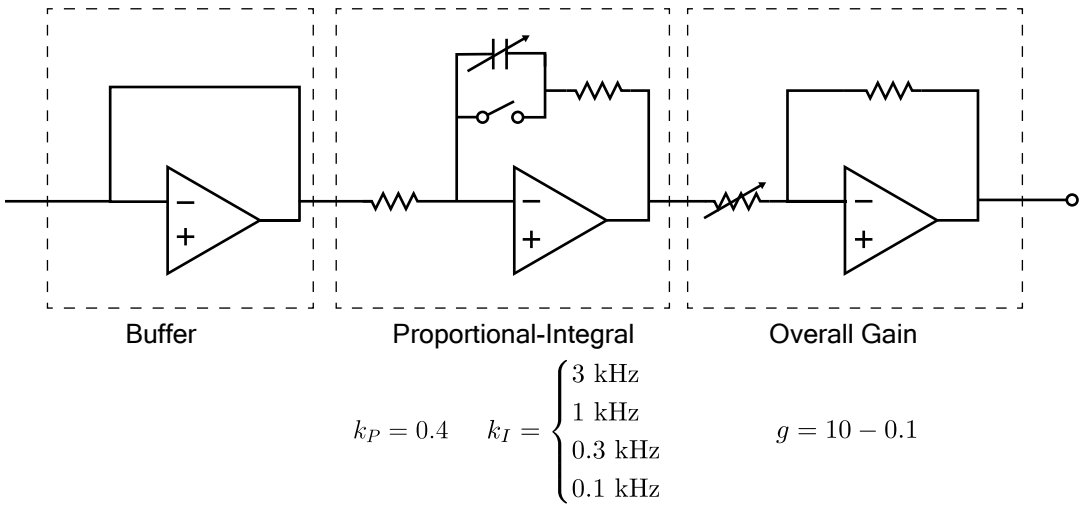

Figure 4.7: A schematic of the loop filter circuit, divided into three stages. A buffer is implemented as an op-amp in the first stage. A proportional-integral stage is second, with fixed proportional gain k_p, variable integral gain k_I. A switch shorts out the integrator, leaving a proportional only stage. The final stage provides variable overall gain g.

loosely locked. The last stage provides a variable overall gain, ranging from 10 - 0.1, which is accessible by the potentiometer on the front panel. The overall loop filter gain is thus

$$F(s) = gk_p + \frac{gk_I}{s} \tag{4.46}$$

where the proportional gain $K_P = gk_p$ and the integral gain $K_I = gk_I$. We typically use the settings $g = 10$, giving us an overall proportional gain $K_P = 4$. The integral gain varies.

4.6 Testing

Ultimately we require that out phase feedback system provides a constant geometry optical lattice, and does not add any additional heating to our atoms. We turn these two requirements into a set of observables we can use to optimize our system.

If the geometry of the optical lattice fluctuates faster than the largest tunneling timescale in the system J/h, we expect that the atomic wavefunction does not follow these changes. We thus expect that variations of the geometry between different experimental realizations are roughly determined by the RMS noise in the error signal $\theta_{err}(t)$, over a bandwidth J/h. Instead of optimizing these results for every value of J/h, we simply consider the worse case scenario: when J/h is largest. In practice the noise of the system is dominated by frequencies less than 1 kHz, and so we simply measure the RMS noise in the error signal over 10s of ms. As the largest J/h values in our system are 100s of Hz, this is likely an overestimate. We characterize the displacement as

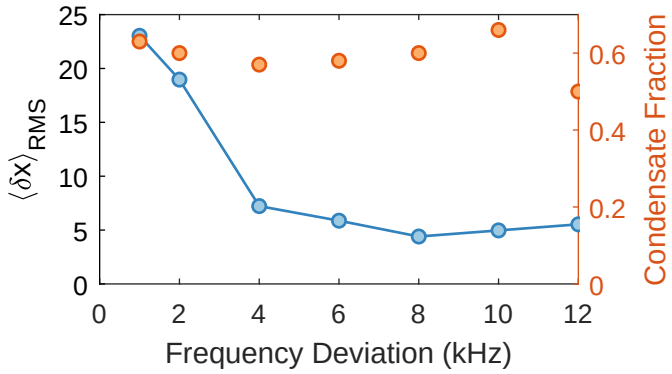

Figure 4.8: Optimization of the feedback gain, performed before August 2018 data was taken. The overall gain of $G(s)$ is scaled by the frequency deviation of the Keysight function generator. Increasing the gain decreases the observed error signal, converted to displacement here. No significant heating is observed at higher gain, as seen in the condensate fraction data. Note in this case K_{VCO} = Frequency Deviation (kHz)/5 V.

$$|\delta| = \frac{2\lambda}{3}\frac{V_{RMS}}{2\pi K_D} \tag{4.47}$$

where V_{RMS} is the RMS noise in the error signal V_{PD}. As we also measure in loop, we may also be mapping electronic noise onto the phase of the light by suppressing the error signal. Ideally we would measure with a phase detector out of loop, and simply minimize V_{RMS} but that comes with considerable overhead.

To quantify the effect of higher frequency fluctuations on the heating of the system, we use the atoms. We typically prepare a weakly interacting gas in a lattice of tubes of a single color of light, and hold for a long period of time. By ramping down the lattice slowly, we map the excitations of the system onto the condensate fraction. As we increase the gain we tend to see a drop in condensate fraction, likely due to the mapping of electronic noise onto the system as described above.

Optimization example

In figure 4.8, we show an example of an optimization of the PLL final gain by adjustment of the frequency deviation. We load a 532 nm lattice of tubes to a depth $V_{532} = 90$ kHz as described in chapter 6, and hold for 100 ms. The lattice ramp is reversed to create a Bose-Einstein condensate and the condensate fraction is measured in time-of-flight. This is compared to the RMS fluctuations of 532 nm B1-B2 θ_{err} for as measured on an oscilloscope as shown in figure

As we increase the overall gain, the error signal is suppressed, but see no change in the condensate fraction. Whilst we cannot see the signs of heating here at high gain, we do not see an improvement in the error signal beyond 8 kHz, and simply choose chose this as the 532

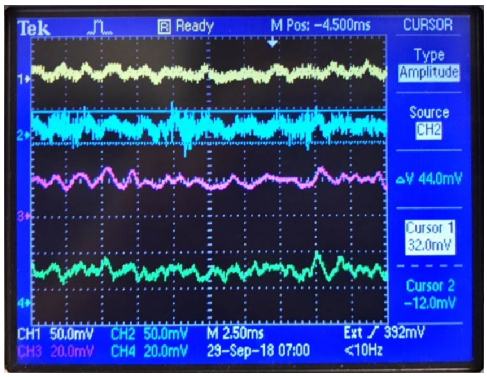

Figure 4.9: Example error signal traces taken during the final hold period of the experimental cycle. From top to bottom: 532 nm B1-2 error signal (yellow), 532 nm B2-3 error signal (blue), 1064 nm B1-2 error signal (pink), 1064 nm B2-3 error signal (green). All signals have a constant run to run offset, i.e. the average of these signals does not vary significantly run to run. Therefore we estimate the run to run error as the RMS size of these signals. The high frequency noise on 532 nm B2-3 is pickup noise from the long BNC cable.

nm frequency deviation for B1 feedback. The other three feedback systems are optimized in a similar manner.

The constraint on the frequency deviation for stability, equation 4.44 is well satisfied by the choice of frequency deviation of 8 kHz. In fact the gain margin of the system is 10, well above the rules of thumb suggested.

The absence of significant heating and the large gain margin suggest room for further increase in F_{dev}.

Final estimate of the error

Finally, in table 4.8 we show displacement estimates for the experimental data taken in August 2018 (see chapter 5 and 6). In chapter 6, we derive the sensitivity of the energy shift ΔE between sites A and BC of the trimerized kagome lattice to displacements of the optical lattice (equation 6.23). For this energy shift to be less than the tunneling energy J, we require a displacement of less than 1 nm at $V_{1064} = 40$ kHz.

The displacements of the individual lattices, as derived from the error signal are shown in table 4.8. Clearly these numbers are larger than our requirement, but also represent an overestimation of the fluctuations.

Experimental measurements

In chapter 6 we derive the RMS deviation of the momentum space populations ΔP for an ideal trimerized kagome lattice in terms of the relative displacement δ. In this section we calculate these deviations ΔP for a set of data taken under nominally identical conditions in

	Error signal V_{RMS}	Phase Detector Gain K_D	$\lvert\delta\rvert$
532 nm B1-B2	36 mV	0.48 V/rad	4 nm
532 nm B3-B2	56 mV	0.7 V/rad	5 nm
1064 nm B1-B2	11 mV	0.5 V/rad	2 nm
1064 nm B3-B2	13 mV	0.52 V/rad	3 nm

Table 4.8: Final RMS displacement measurements for data taken August 2018. These estimates for δ are inferred from the RMS error signal.

order to estimate the run-to-run fluctuations of δ. We analyze the momentum distributions of the $t = 0$ subset of the data described in section 6.3. This subset represents an gas prepared in a trimerized kagome lattice of depths $V_{532}/h = 45$ kHz, $V_{1064}/h = 15$ kHz with none of the evolution in a single lattice that is described in section 6.3. We calculate the relative populations in the first order diffraction peaks, defined as

$$P_i = \frac{n_{\boldsymbol{G}_i} + n_{\boldsymbol{G}_i}}{n_{\boldsymbol{G}_1} + n_{\boldsymbol{G}_{-1}} + n_{\boldsymbol{G}_2} + n_{\boldsymbol{G}_{-2}} + n_{\boldsymbol{G}_3} + n_{\boldsymbol{G}_{-3}}}, \tag{4.48}$$

and then calculate the RMS deviation from the ideal trimerized kagome lattice, where $P_1 = P_2 = P_3 = 1/3$:

$$\Delta P = \sqrt{(P_1 - \tfrac{1}{3})^2 + (P_2 - \tfrac{1}{3})^2 + (P_3 - \tfrac{1}{3})^2}. \tag{4.49}$$

This RMS quantity ΔP is independent of the exact direction that a given displacement $\boldsymbol{\delta}$ occurs. Thus when we compare the experimental ΔP to that calculated in chapter 6, which was the result of displacement along the x-axis, we are making an approximation. The calculated relationship between ΔP and the RMS displacement δ_{RMS} equation x, is

$$\delta_{RMS} = \frac{3}{8.4}\sqrt{\frac{3}{2}}\Delta P \frac{\mu}{V_{1064}} a \tag{4.50}$$

For a chemical potential of $\mu/h = 550$ Hz, and $V_{1064}/h = 15$ kHz, the run to run displacement δ_{RMS} is shown in figure 4.10, with a data set averaged mean of $\delta_{RMS} = 1.3$ nm. This experimentally derived estimate of the relative displacement is smaller than the estimates derived from the error signals in table 4.8. This observation suggests that the error signal derived estimates are indeed an overestimate. Further investigation could be done by performing the same experiment are higher V_{1064}, and ensuring the measured ΔP scale appropriately.

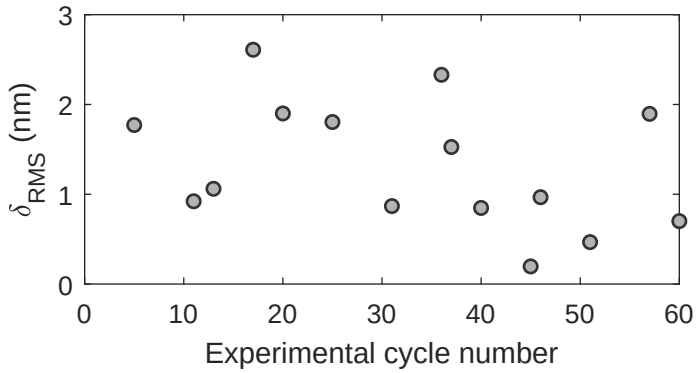

Figure 4.10: Run to run RMS displacement for the $t = 0$ subset of the experiment described in section 6.3. The average RMS displacement is 1.3 nm.

Chapter 5

Phase coherence in the Mott insulator

In our work on mean-field scaling, we showed that such a theory provides a good description of the phase transition between superfluid and Mott insulating states [67]. In this theory we ignore the correlations between sites and solve an energetics problem. It is surprising that mean-field theory provides a good description, given that these correlated fluctuations are what drive quantum phase transitions.

Approaching the phase transition in the reverse direction, from the Mott insulator to the superfluid state, correlated number fluctuations break up the fixed particle number Mott insulating state. These correlated number fluctuations lead to a small coherence length deep in the Mott insulating phase. As the system approaches the phase transition, this coherence length diverges and the gas becomes a superfluid.

To see some of the effects of quantum fluctuations in a Bose-Hubbard system, we follow the lead of seminal experiments in Munich [26], Maryland [60] and Hamburg [5] and study the phase coherence of the Mott insulator. In this chapter, we first explain how the momentum distribution of a Bose gas encodes the phase coherence, then explain how phase coherence arises in the Mott insulator. We then explain how we perform experiments realizing a Mott insulating gas in a triangular lattice, and extracting the phase coherence. Finally we resolve a discrepancy between theory and experiment.

5.1 Momentum distribution

The momentum distribution of a bosonic gas is defined as

$$n(\boldsymbol{k}) = \int d^3\boldsymbol{r}\, d^3\boldsymbol{r}'\, e^{i\boldsymbol{k}\cdot(\boldsymbol{r}-\boldsymbol{r}')}\langle\Psi^\dagger(\boldsymbol{r})\Psi(\boldsymbol{r}')\rangle \tag{5.1}$$

where $\Psi(\boldsymbol{r})$ is the bosonic field operator [43]. Making the same Wannier substitution as before, $\Psi(\boldsymbol{r}) = \sum_i w_i(\boldsymbol{r}-\boldsymbol{r}_i)b_i$, this becomes

$$n(\boldsymbol{k}) = \sum_{i,j} \tilde{w}_i^*(\boldsymbol{k})\tilde{w}_j(\boldsymbol{k})e^{i\boldsymbol{k}\cdot(\boldsymbol{r}_i-\boldsymbol{r}_j)}\langle b_i^\dagger b_j\rangle \tag{5.2}$$

where $\tilde{w}_i(\boldsymbol{k}) = \int d^3\boldsymbol{r}_1 w_i^*(\boldsymbol{r}_1 - \boldsymbol{r}_i)\, e^{i\boldsymbol{k}\cdot\boldsymbol{r}_1}$ is the Fourier transform of the Wannier function on site i. To gain some insight into the momentum distribution we will assume the system is invariant under the translation of one site, which means all Wannier functions are the same. This is not true in general, and won't be true for some of the lattices we study. In this simplified case, equation 5.1 becomes

$$n(\boldsymbol{k}) = N|w(\boldsymbol{k})|^2 \sum_i e^{i\boldsymbol{k}\cdot\boldsymbol{r}_i}\langle b_0^\dagger b_i\rangle. \tag{5.3}$$

The momentum distribution is thus a Fourier sum of coherences $\langle b_0^\dagger b_i\rangle$ at different lengths i, with an approximately Gaussian envelope. In the superfluid limit of the Bose-Hubbard model the coherence length is the system size, so many Fourier terms add up to give sharp peaks in the momentum distribution. In the Mott insulating limit, the coherence length is very short so at most we expect to see a slow modulation of the Wannier function. The signature of correlated number fluctuations in the Mott insulator will be precisely this slow modulation.

The terms $e^{i\boldsymbol{k}\cdot\boldsymbol{r}_i}\langle b_0^\dagger b_i\rangle$ and $e^{-i\boldsymbol{k}\cdot\boldsymbol{r}_i}\langle b_0^\dagger b_{-i}\rangle = e^{-i\boldsymbol{k}\cdot\boldsymbol{r}_i}\langle b_0^\dagger b_i\rangle^*$ add together to give a momentum symmetric $\cos(\boldsymbol{k}\cdot\boldsymbol{r}_i)$ modulation and a momentum anti-symmetric $\sin(\boldsymbol{k}\cdot\boldsymbol{r}_i)$ modulation. The strength of the cosine modulation is proportional to the real part of the coherence $\langle b_0^\dagger b_i\rangle$, whilst the sine part is proportional to the imaginary part of the same coherence.

Validity of the momentum distribution

In practice we obtain an approximation of the momentum distribution by letting the atoms expand in time-of-flight t_{TOF}. For times much larger than the lattice well oscillation frequency ω_L, the spatial distribution of the gas is given by

$$n(\boldsymbol{r}) = \left(\frac{m}{\hbar t}\right)^3 |w(\boldsymbol{k})|^2 \sum_{i,j} e^{i\boldsymbol{k}\cdot(\boldsymbol{r_i}-\boldsymbol{r}_j) - i(m/2\hbar t)(\boldsymbol{r}_i^2 - \boldsymbol{r}_j^2)}\langle b_i^\dagger b_j\rangle, \tag{5.4}$$

where $\boldsymbol{k} = m\boldsymbol{r}/\hbar t_{TOF}$ [24]. This only simplifies to the momentum distribution when $t_{TOF} \gg T_{FF}$, where the far-field time T_{FF} is defined as

$$T_{FF} = m l_c R_0/\hbar \tag{5.5}$$

where R_o is the system size, and l_c is the coherence length [24]. When the system is deep in the Mott insulating regime, we take the coherence length to be one site giving $T_{FF} = 4$ ms for typical system parameters ($R_0 = 10$ μm, $l_c = 355$ nm).

Interactions during time-of-flight can also distort the momentum distribution. When the atoms are released from the lattice, their wavefunctions quickly expand and the direct overlap required for contact interactions increases. However their density rapidly decreases, and whether this is sufficiently fast as to neglect interactions is captured by the ratio $U/\hbar\omega_L$ in a 3D optical lattice [24].

We assumed this term was small in our derivation of the Hubbard model, and in practice this ratio is maximally 0.05 for the lattice parameters we use in the Mott insulating regime.

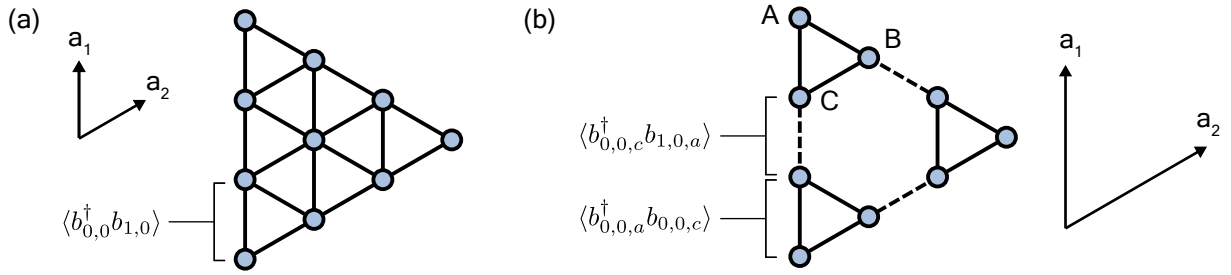

Figure 5.1: Coherences on triangular and trimerized kagome lattice. (a) The nearest-neighbor coherence of a triangular lattice is simply described by a single pair of sites. (b) The nearest-neighbor coherence of a trimerized kagome lattice. There are two contributions, one between sites across strong bond, and the other across weak bonds. Note the lattice vectors in the trimerized kagome lattice are twice as long as those in the triangular lattice.

Momentum distribution of specific lattices

We now evaluate equation 5.2 on specific lattices in the case of nearest-neighbor coherence, i.e. where $\langle b_i^\dagger b_j \rangle = 0$ for $|r_i - r_j| > a$, as depicted in figure 5.1. This will provide us functional forms to compare theory and experiment. We will also make assumptions about rotational symmetry and realness of the coherences given the type of state studied. The coherences of ground states will be real, and inherit the underlying rotational symmetry of the lattice. More general states have both real and imaginary coherences, and can be rotationally asymmetric.

Triangular lattice ground state

The unit cell of the triangular lattice is just one site, so nearest-neighbor coherences occur between identical sites displaced by the lattice vectors $\boldsymbol{a}_1$ and $\boldsymbol{a}_2$. We expect the coherences in the ground state to be real with sixfold rotational symmetry, giving us the momentum distribution

$$n(\boldsymbol{k}) = N|\tilde{w}(\boldsymbol{k})|^2(1 + \alpha(\cos(\boldsymbol{k}\cdot\boldsymbol{a}_1) + \cos(\boldsymbol{k}\cdot\boldsymbol{a}_2) + \cos(\boldsymbol{k}\cdot\boldsymbol{a}_3)) \tag{5.6}$$

where N is the total particle number, and $\boldsymbol{a}_3 = \boldsymbol{a}_1 - \boldsymbol{a}_2$. Defining the sites on the triangular lattice as $\boldsymbol{r}_{i,j} = i\boldsymbol{a}_1 + j\boldsymbol{a}_2$, we introduce the quantity

$$\alpha_{Tri} = \frac{2}{n}\langle b_{0,0}^\dagger b_{1,0}\rangle \tag{5.7}$$

which is twice the nearest-neighbor coherence per particle at one lattice site. n is the number of particles per site.

Trimerized kagome lattice ground state

The trimerized kagome lattice, introduced in the next chapter, has three sites per unit cell, and two different bond strengths. Nearest-neighbor coherence occurs between sites displaced by $\boldsymbol{a}_i/2$. The three sites, labeled A, B and C in general have three different Wannier functions w_A, w_B and w_C. Again assuming the ground state coherences are real with threefold rotational symmetry,

$$\begin{aligned} n(\boldsymbol{k}) = N(&\tfrac{1}{3}\tilde{w}_1^2(\boldsymbol{k}) + \tfrac{1}{3}\tilde{w}_2^2(\boldsymbol{k}) + \tfrac{1}{3}\tilde{w}_3^2(\boldsymbol{k}) + \alpha\tilde{w}_1(\boldsymbol{k})\tilde{w}_2(\boldsymbol{k})\cos(\boldsymbol{k}\cdot\boldsymbol{a}_1/2) \\ &+ \alpha\tilde{w}_1(\boldsymbol{k})\tilde{w}_3(\boldsymbol{k})\cos(\boldsymbol{k}\cdot\boldsymbol{a}_2/2) + \alpha\tilde{w}_2(\boldsymbol{k})\tilde{w}_3(\boldsymbol{k})\cos(\boldsymbol{k}\cdot\boldsymbol{a}_3/2)) \end{aligned} \tag{5.8}$$

where in this case ν is the number of particles per plaquette, and

$$\alpha_{TKL} = \tfrac{2}{\nu}\left(\langle b^\dagger_{0,0,a} b_{0,0,c}\rangle + \langle b^\dagger_{0,0,c} b_{1,0,a}\rangle\right). \tag{5.9}$$

The sites of the trimerized kagome lattice are $r_{i,j,\gamma} = i\boldsymbol{a}_1 + j\boldsymbol{a}_2 + \boldsymbol{r}_\alpha$, for $\gamma \in \{\mathrm{a}, \mathrm{b}, \mathrm{c}\}$.

Trimerized kagome lattice general state

An excited state of the trimerized kagome lattice does not have the restriction that the coherences must be real, nor do we expect it to have threefold rotational symmetry. Making the assumption that the Wannier states are negligibly different gives us

$$\begin{aligned} n(\boldsymbol{k}) = N|\tilde{w}_1(\boldsymbol{k})|^2(1 &+ \alpha_1(\cos(\boldsymbol{k}\cdot\boldsymbol{a}_1/2) + \alpha_2\cos(\boldsymbol{k}\cdot\boldsymbol{a}_2/2) + \alpha_3\cos(\boldsymbol{k}\cdot\boldsymbol{a}_3/2)) \\ &+ \beta_1\sin(\boldsymbol{k}\cdot\boldsymbol{a}_1/2) + \beta_2\sin(\boldsymbol{k}\cdot\boldsymbol{a}_2/2) + \beta_3\sin(\boldsymbol{k}\cdot\boldsymbol{a}_3/2)) \end{aligned} \tag{5.10}$$

where

$$\alpha_1 = \frac{2}{\nu}\mathrm{Re}\left(\langle b^\dagger_{0,0,a} b_{0,0,c}\rangle + \langle b^\dagger_{0,0,c} b_{1,0,a}\rangle\right) \qquad \beta_1 = \frac{2}{\nu}\mathrm{Im}\left(\langle b^\dagger_{0,0,a} b_{0,0,c}\rangle + \langle b^\dagger_{0,0,c} b_{1,0,a}\rangle\right) \tag{5.11}$$

$$\alpha_2 = \frac{2}{\nu}\mathrm{Re}\left(\langle b^\dagger_{0,0,c} b_{0,0,b}\rangle + \langle b^\dagger_{0,0,c} b_{0,1,b}\rangle\right) \qquad \beta_2 = \frac{2}{\nu}\mathrm{Im}\left(\langle b^\dagger_{0,0,c} b_{0,0,b}\rangle + \langle b^\dagger_{0,0,c} b_{0,1,b}\rangle\right) \tag{5.12}$$

$$\alpha_2 = \frac{2}{\nu}\mathrm{Re}\left(\langle b^\dagger_{0,0,b} b_{0,0,a}\rangle + \langle b^\dagger_{0,0,a} b_{1,-1,b}\rangle\right) \qquad \beta_2 = \frac{2}{\nu}\mathrm{Im}\left(\langle b^\dagger_{0,0,b} b_{0,0,a}\rangle + \langle b^\dagger_{0,0,a} b_{1,-1,b}\rangle\right) \tag{5.13}$$

Kagome lattice ground state

The (untrimerized) kagome lattice also has three sites per unit cell, but only one bond strength. Nearest-neighbor coherence occurs between sites displaced by $\boldsymbol{a}_i/2$. The three sites, labeled A, B and C in general have three different Wannier functions w_A, w_B and w_C. Again assuming the ground state coherences are real with threefold rotational symmetry gives,

$$\begin{aligned} n(\boldsymbol{k}) = N(&\tfrac{1}{3}\tilde{w}_1^2(\boldsymbol{k}) + \tfrac{1}{3}\tilde{w}_2^2(\boldsymbol{k}) + \tfrac{1}{3}\tilde{w}_3^2(\boldsymbol{k}) + \alpha\tilde{w}_1(\boldsymbol{k})\tilde{w}_2(\boldsymbol{k})\cos(\boldsymbol{k}\cdot\boldsymbol{a}_1/2) \\ &+ \alpha\tilde{w}_1(\boldsymbol{k})\tilde{w}_3(\boldsymbol{k})\cos(\boldsymbol{k}\cdot\boldsymbol{a}_2/2) + \alpha\tilde{w}_2(\boldsymbol{k})\tilde{w}_3(\boldsymbol{k})\cos(\boldsymbol{k}\cdot\boldsymbol{a}_3/2)) \end{aligned} \tag{5.14}$$

where in this case n is the number of particles per site, and

$$\alpha_{Kag} = \tfrac{2}{n}\langle b^\dagger_{0,0,a} b_{0,0,c}\rangle. \tag{5.15}$$

The sites of the kagome lattice are $r_{i,j,\gamma} = i\boldsymbol{a}_1 + j\boldsymbol{a}_2 + \boldsymbol{r}_\alpha$, for $\gamma \in \{\mathrm{a}, \mathrm{b}, \mathrm{c}\}$.

Longer range coherences

In general, coherences exist in our system beyond one lattice site. When the coherences are very long range, such as in the superfluid state, it makes more sense to analyze the system in the quasimometum picture. For intermediate range coherence, we consider the Fourier transform of the momentum distribution

$$F[n(\boldsymbol{k})] = N\sum_\mu \alpha_\mu F[|\tilde{w}(\boldsymbol{k})|^2 e^{i\boldsymbol{k}\cdot\boldsymbol{r}_\mu}] = N\sum_\mu \alpha_\mu W(\boldsymbol{r} - \boldsymbol{r}_\mu) \tag{5.16}$$

where we have summed all of the coherences of length μ into $\alpha_\mu = \frac{1}{N}\sum_\nu \langle b^\dagger_{(\mu+\nu)/2} b_{(\mu-\nu)/2}\rangle$ and defined $W(\boldsymbol{r}) = F[|\tilde{w}(\boldsymbol{k})|^2]$. As the Wannier function is approximately Gaussian, the Fourier transform of the momentum distribution is simply a set of displaced Gaussian functions, with amplitudes proportional to the sum of coherences at that length.

Effect of terminated expansion

We terminated the expansion of equation 5.2, only considering coherences between sites r_m and r_n if $|r_m - r_n| < a$. In principle, the presence of longer range coherences in the gas leads to an overestimation of the nearest-neighbor coherence if the longer range coherences are not accounted for in the fitting function. This overestimation occurs because functions of the form $|\tilde{w}(\boldsymbol{k})|^2 \cos(\boldsymbol{k}\cdot(i\boldsymbol{a}_1 + j\boldsymbol{a}_2)$ are not exactly orthogonal when i and j are different. The level of overlap of these functions is controlled by the relative width of $|\tilde{w}(\boldsymbol{k})|^2$ to the lattice spacing a.

In practice we find that fitting gases with the expansion truncated at $|r_m - r_n| < a$ does not produce a systematic difference when compared to fitting with an expansion truncated at $|r_m - r_n| < 2a$. However, this observation does not hold true in general, and care must be taken when higher order correlations are expected to be large.

5.2 Perturbation theory

In this section we will demonstrate how a weak tunneling term admixes particle-hole excitations into the Mott insulating ground state, leading to phase coherence between sites. Whilst we will study this from a perturbation theory perspective in the limit of weak tunneling, we note the existence of a strong coupling description of the same problem [25]. We begin by solving the $J = 0$ limit of the Bose-Hubbard Hamiltonian on the triangular lattice, given by

$$H = U/2 \sum_i n_i(n_i - 1) - \mu \sum_i n_i \tag{5.17}$$

The ground state is a product state of number Fock states at each lattice site,

$$|\Psi_0\rangle = \prod_i |n\rangle_i \tag{5.18}$$

where there are n atoms per site if $(n-1)U < \mu < nU$ and the ground state energy is $E_0 = N(\frac{U}{2}n(n-1) - \mu n)$, where N is the number of sites. The lowest energy excitations fall into three categories: states with an extra particle $|\Psi_{P,j}\rangle$, states with a missing particle (or extra hole) $|\Psi_{H,j}\rangle$ and states with a particle and hole $|\Psi_{PH,i,j}\rangle$, with wave functions and excitation energies ΔE given by

Particle states:	$\|\Psi_{P,j}\rangle = \frac{1}{\sqrt{n+1}} b_j^\dagger \|\Psi_0\rangle$	$\Delta E = nU - \mu$
Hole states:	$\|\Psi_{H,j}\rangle = \frac{1}{\sqrt{n}} b_j \|\Psi_0\rangle$	$\Delta E = U(1-n) + \mu$
Particle-hole states	$\|\Psi_{PH,i,j}\rangle = \frac{1}{\sqrt{n(n+1)}} b_i^\dagger b_j \|\Psi_0\rangle$	$\Delta E = U$

Now we consider the action of the hopping term $V = -J \sum_{<i,j>} b_i^\dagger b_j$ in the context of first order perturbation theory. We can clearly see from the form of the perturbation that it will couple the ground state to some of the particle-hole states, but not to the particle or hole states. In fact, only the nearest-neighbor particle-hole state will be admixed into the ground state. The perturbation does diagonalize the particle and hole states, forming excited bands which will be relevant in the discussion of finite temperature. The admixture of these excited particle-hole states $\left|\Psi^0_{PH,m.n}\right\rangle$ into the ground state $|\Psi_0^0\rangle$ is given by

$$\begin{aligned}
\left|\Psi_0^1\right\rangle &= \left|\Psi_0^0\right\rangle + \sum_{m,n} \frac{\langle\Psi_0^0| V \left|\Psi^0_{PH,m,n}\right\rangle}{E_{PH,m,n} - E_0} \left|\Psi^0_{PH,m,n}\right\rangle \\
&= \left|\Psi_0^0\right\rangle - \frac{J}{U} \sum_{m,n} \sum_{<i,j>} \frac{1}{\sqrt{n(n+1)}} \left\langle\Psi_0^0\right| b_i^\dagger b_j b_m^\dagger b_n \left|\Psi_0^0\right\rangle \left|\Psi^0_{PH,m,n}\right\rangle \\
&= \left|\Psi_0^0\right\rangle - \frac{J}{U} \sum_{m,n} \sum_{<i,j>} \frac{n(n+1)}{\sqrt{n(n+1)}} \delta_{jm}\delta_{in} \left|\Psi^0_{PH,m,n}\right\rangle \\
&= \left|\Psi_0^0\right\rangle - \frac{J}{U} \sum_{<i,j>} \sqrt{n(n+1)} \left|\Psi^0_{PH,m,n}\right\rangle \\
&= \left|\Psi_0^0\right\rangle - \frac{J}{U} \sum_{<i,j>} b_i^\dagger b_j \left|\Psi_0^0\right\rangle
\end{aligned} \tag{5.19}$$

Nearest-neighbor particle hole states are admixed into the ground state, which is what leads to a non-zero nearest-neighbor coherence:

$$\begin{aligned}\langle a_0^\dagger a_1\rangle &= \left(\langle\Psi_0|^{(0)} - \frac{J}{U}\sum_{<i,j>}\langle\Psi_0|^{(0)} b_i b_j^\dagger\right) b_0^\dagger b_1 \left(|\Psi_0\rangle^{(0)} - \frac{J}{U}\sum_{<i,j>} b_i^\dagger b_j |\Psi_0\rangle^{(0)}\right) \\ &= -\frac{2J}{U}\sum_{<i,j>}\langle\Psi_0|^{(0)} b_0^\dagger b_1 b_1^\dagger b_0 + b_0 b_1^\dagger b_0^\dagger b_1 |\Psi_0\rangle^{(0)} \\ &= -\frac{2J}{U} n(n+1). \end{aligned} \tag{5.20}$$

Thus on the triangular lattice, we have the result

$$\alpha_{Tri} = 4(n+1)U/J. \tag{5.21}$$

Inhomogenous filling

As explained in chapter 2, we account for the presence of an overall harmonic trapping potential by making the local density approximation. At each point in space the gas is described by a Bose-Hubbard model with a local chemical potential $\mu(r)$, leading to a slowly varying density profile [73].

When the gas is described by an ideal Mott insulating state, the density profile takes the form of concentric rings of constant particle number per site, known a 'wedding cake' structure. As equation 5.21 is linear in n, we assume that the ensemble averaged nearest-neighbor coherence is simply given by the ensemble averaged density,

$$\langle\alpha_{tri}\rangle = 4(\langle n\rangle + 1)U/J. \tag{5.22}$$

In doing this, we assume that sites of a given particle number n only develop coherences with sites of equal particle number in the mechanism described in section 5.2. Thus we ignore the regions between different Mott lobes. In these regions the delocalization of atoms across the boundary costs very little energy, and as such a strong nearest-neighbor coherence is developed. Whilst the fraction of the gas occupying these regions is small, the strong nearest-neighbor coherence means these regions may not be negligible.

Finite temperature

Whilst the particle and hole states are not coupled to the ground state by first order action of the perturbation V, the action of the perturbation on these states is important at finite temperature. The perturbation diagonalizes these degenerate states, forming bands of delocalized particles and holes.

These bands can be thermally populated, and the energy cost to do so is relatively small for chemical potentials close to the edge of the Mott lobe. If just the lowest energy states of these bands are occupied, there can be a substantial increase in the nearest-neighbor

coherence α as these states all have a nearest neighbor coherence of 1. Thus as noted in [69], the nearest-neighbor coherence of the whole system initially increases with temperature, before dropping towards zero.

5.3 Comparison of theory and experiment

In this section we will describe experiments done in the lab measuring the short range coherence of Mott insulating states of atoms in a two dimensional triangular lattice.

Experimental procedure

The experiment begins after evaporative cooling of rubidium atoms in a hybrid optical and magnetic trap to quantum degeneracy. At the end of evaporation we have a Bose-Einstein condensate of 5×10^4 atoms with an undetectable thermal fraction in a final trap with trap frequencies $\omega_x = 2\pi \cdot 34$ Hz, $\omega_y = 2\pi \cdot 64$ Hz and $\omega_z = 2\pi \cdot 49$ Hz.

We load both an in-plane triangular lattice, and an out of plane vertical lattice in a two-step sequence. In the first step we increase the power in the in-plane beams until we have sufficient signal-to-noise for the optical phase lock system described in chapter 5 to engage. The power is held at this level for 20 ms while the integrator in the loop feedback switched on. In the second section, the triangular lattice and vertical lattice powers are ramped up exponentially to their final values.

The vertical lattice is always ramped to a constant depth of 41 kHz, which splits the gas into an ensemble of disconnected systems. The tunneling time between 'pancakes' is $h/J = 200$ ms, greater than the 30 ms timescale over which experiments occur. Furthermore, the vertical trap frequency of these isolated systems is $\omega_z = 2\pi \cdot 18$ kHz, which is large compared to the atomic temperature or Hubbard model energies, and as such the system is strongly two-dimensional.

In the second loading step the power in triangular lattice is exponentially increased. The final depth of the triangular lattice is chosen to access desired Bose-Hubbard parameters. During this lattice ramp the power in the crossed dipole traps is increased.

After the lattice has finished loading, we hold for 30 ms before simultaneously switching off all of the lattice beams and dipole traps. The atoms evolve in a magnetic potential that is harmonic in-plane, and with a gradient in the vertical direction that cancels gravity. By evolving for a quarter-cycle of the harmonic period (16 ms), the density distribution is transformed into the momentum distribution.

The atoms are pumped into the $|F = 2\rangle$ hyperfine manifold before being illuminated with a 100 μs pulse of a laser beam co-propagating with the vertical lattice, and resonant on the $|F = 2, m_F = 2\rangle \rightarrow |F' = 3, m'_F = 3\rangle$ transition. The atoms leave a shadow in the beam, which is imaged with 2X magnification onto a CCD camera. Two further images are taken, one with an identical pulse with no atoms present, and one with no pulse at all.

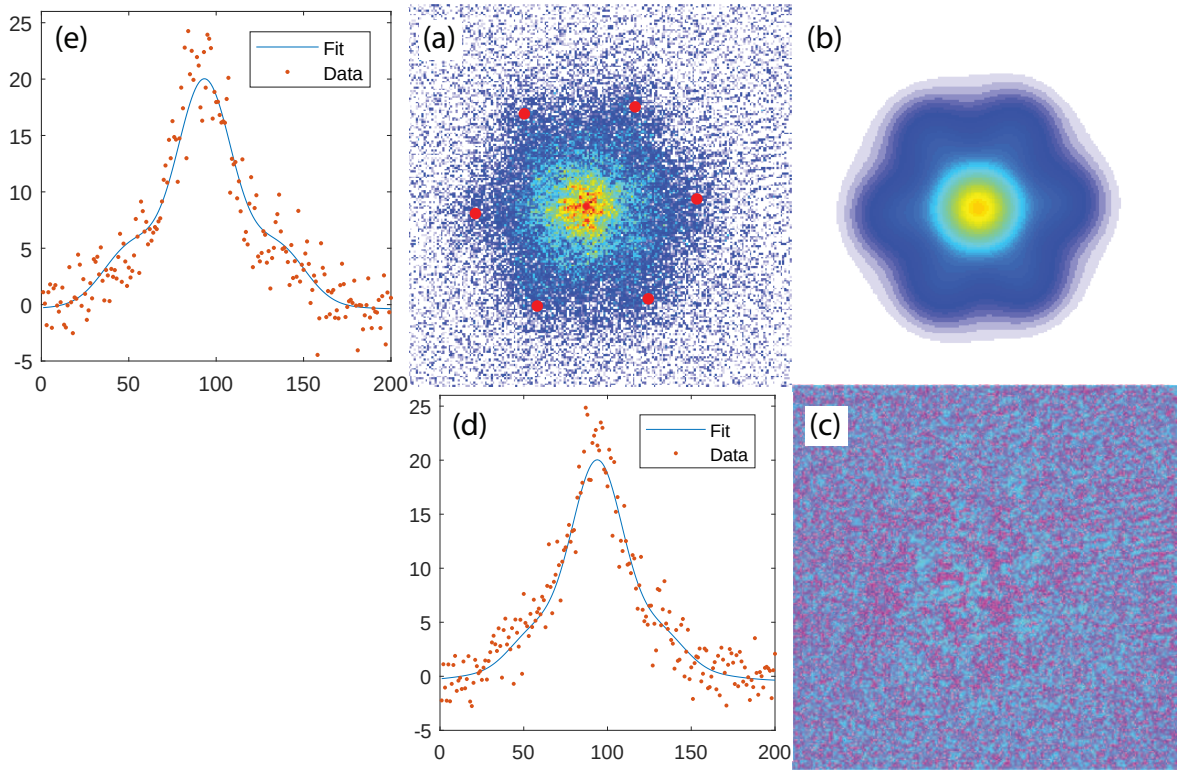

Figure 5.2: Images of the phase coherence fitting. (a) Momentum distribution of a Mott insulator in a triangular lattice at $U/J' = 80$. The six-fold symmetry of the image demonstrates a weak nearest-neighbor coherence in the system. Red dots show the position of the first order reciprocal lattice vectors $\boldsymbol{G}_i$. (b) The fitted momentum distribution yielding $\alpha = 0.15$. (c) Fitting residuals. These are not simply shot-noise fluctuations, there is some structure in the image. However, it doesn't clearly take the form of longer range correlations. (d) Cut-through of the data (red dots) and fit (blue line) along the x-axis. No modulation is visible as this cut is orthogonal to the lattice vector $\boldsymbol{a}_1$. (e) Cut-through of data and fit along y-axis. The modulation due to phase coherence is clearly visible in the fit.

We reconstruct the optical density, and thus the real density $n(\boldsymbol{r})$ as is standard in absorption imaging. An example of the density is shown in figure 5.2(a).

Data analysis

To extract the nearest-neighbor coherence α from the acquired images, we perform least squares fitting of the following functional form

$$n(\boldsymbol{R}) = a + be^{-\boldsymbol{R}^2/(2f^2)}(1 + \alpha_1 \cos(\boldsymbol{a}_1 \cdot \boldsymbol{R}) + \alpha_2 \cos(\boldsymbol{a}_2 \cdot \boldsymbol{R}) + \alpha_3 \cos(\boldsymbol{a}_3 \cdot \boldsymbol{R})) \tag{5.23}$$

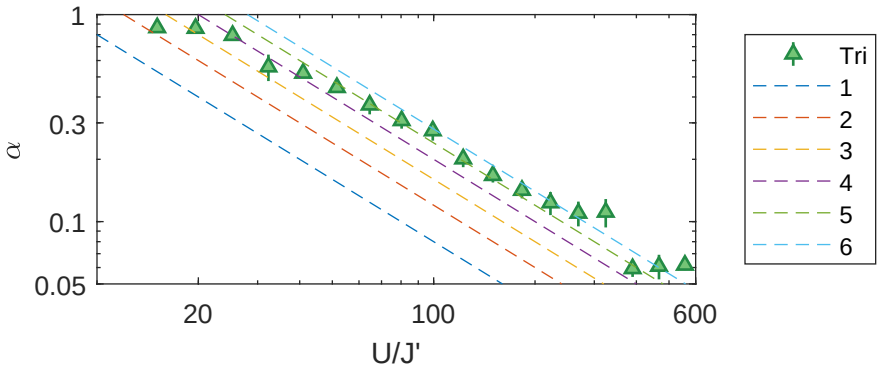

Figure 5.3: Initial results for the nearest-neighbor coherence of atoms in a triangular lattice (green triangles). Data taken in January 2018. Dashed lines are perturbation theory results for varying particle number per site n, using equation 5.21. After $U/J' = 30$ the data approximately follows the $n = 5 - 6$ lines, showing the the expected $(U/J')^{-1}$ scaling. However the overall coherence is much larger than expected for $n < 1$.

where $\boldsymbol{R}$ are the rotated and centered co-ordinates

$$\boldsymbol{R} = \begin{pmatrix} \cos(t) & -\sin(t) \\ \sin(t) & \cos(t) \end{pmatrix} \begin{pmatrix} x - x_0 \\ y - y_0 \end{pmatrix}. \tag{5.24}$$

The magnitudes of $\boldsymbol{a}_i$ are set by deriving the reciprocal lattice vectors $\boldsymbol{G}_i$, and ensuring they are coincident with the superfluid diffraction peaks when U/J is small. All other parameters are free to fit. We extract α_i for the three different directions, and then average the three α_i to obtain the experimental value α. An example of this fitting procedure is shown in figure 5.2.

Initial results

In figure 5.3 we show the extracted value of α for varying U/J in the triangular lattice. After $U/J \approx 30$, the coherence falls like $(U/J)^{-1}$, as expected from perturbation theory. However, we find that the prefactor of U/J of 29 for equation 5.22 which in our local density approximation corresponds to an average occupation $\langle n \rangle = 6$ in our lattice. This is substantially larger than our expected average filling of 1. We observed a consistently high value of the nearest-neighbor coherence α over a range of total particle number, final trap frequencies and loading rates. The rest of this chapter is dedicated to our attempts to understand and correct this unusual result.

5.4 Coherence explanations

In this section we will detail our calculation of the filling, and confirm our expected density with a precision spectroscopy technique. We will expand on our discussion of the finite

V_{532}	U	N	$\bar{\omega}$	n_0	$\bar{n}$
120 kHz	2.33 kHz	5×10^4	$2\pi \cdot 47$ Hz	0.74	0.3

Table 5.1: Density estimation in the triangular lattice, assuming a superfluid profile. These are the relevant parameters for the data shown in figure 5.3.

temperature contributions to the coherence, and conclude that the high measured coherence is unlikely to be explained by equilibrium physics.

Density estimation

We can make a crude estimation of the average density by assuming the Mott insulating gas has the same density profile as a superfluid at the same U. This is a poor approximation when the central filling is 1, but as the density increases the superfluid and Mott insulator profiles converge.

Recalling equation 2.21 for the central chemical potential in a three-dimensional optical lattice, we find the central filling is

$$n_0 = \frac{m^{3/5}}{U}\left(\frac{15}{16\pi\sqrt{2}}V_{cell}NU\right)^{2/5}\bar{\omega}^{6/5}. \tag{5.25}$$

The volume of the unit cell is just the area of the triangular unit cell multiplied by the vertical lattice spacing a_{vert}:

$$V_{cell} = a_{vert} \times \sqrt{3}/2 \times |a_{tri}|^2. \tag{5.26}$$

The measured parameters in our experiment, and resultant central density are given in table 5.1.

The central density is nowhere near 6, and for a superfluid in a 3D optical lattice, the average density is $\frac{2}{5}n_0$. We do not expect this relationship to hold when the central filling is below 1. At zero temperature and in equilibrium we would simply expect to see an average density of 1, as the entire gas would form a $n = 1$ Mott insulator.

Density measurements with microwave spectroscopy

Our estimated density measurements are rough, but strongly inconsistent with the density implied by the nearest-neighbor coherence. To confirm this, we measure 10 ppb level interaction shifts of the Rubidium hyperfine resonance, and derive the density from this spectroscopy, following the technique described by [8].

Interaction shifts of hyperfine states

We exploit a small difference in the low energy scattering properties of the rubidium $F = 1$ and $F = 2$ hyperfine states to measure the atom number per site distribution. The s-wave scattering length between $F = 1$ atoms is $a_{11} = 5.32\,\text{nm}$, whereas for one $F = 1$ and one $F = 2$, is $a_{12} = 5.19$ nm [17]. This small difference has an important consequence in an optical lattice: the interaction energy of one $F = 1$ atom, and one $F = 2$ atom is 2.4% larger than that of two $F = 2$ atoms. The resonance frequency for weak microwave excitation from $F = 1$ to $F = 2$ is thus smaller than the bare frequency by 2.4% of $U_{11}$when there are two atoms per site. For n atoms per site, the shift is [8]

$$\delta f = \frac{U}{h}(n-1)\left(\frac{a_{11}-a_{12}}{a_{11}}\right). \tag{5.27}$$

Unfortunately U in our experiment is of order 1 kHz, and thus these shifts are on the order of tens of Hz. This small signal can be easily swamped by uncontrolled Zeeman shifts of the different m_F sublevels of these hyperfine manifolds in a noisy lab environment.

Two-photon clock transitions

We can remedy this problem by choosing initial and final $|F, m_F\rangle$ state with the same first order Zeeman shift. We choose to drive transitions between $|1,-1\rangle$ and $|2,1\rangle$ because both of these states are magnetically trappable, and because the first order insensitivity occurs at finite field, namely 3.23 G. At this magnetic field, the energy differential is $\Delta E = 431\ \text{Hz/G}^2 \times (B - 3.23\ \text{G})^2$ for magnetic field strength B in Gauss [33]. For typical magnetic field fluctuations of ~ 10 mG, this gives line shifts on the order of a 0.1 Hz which should be sufficient to resolve the tens of Hz interaction shifts.

However transitions between $|1,-1\rangle$ and $|2,1\rangle$ are dipole forbidden they differ in m_F by 2. We thus drive a two-photon transition with microwave $\omega_{\mu w}$ and radio frequency ω_{RF} transitions with $|2,0\rangle$ as the intermediate state. The microwaves were detuned 1 MHz above the intermediate state, and the RF was precisely tuned to bring the two photon transition into resonance.

We roughly estimate the maximum microwave and RF Rabi frequencies to be at least $2\pi \cdot 10$ kHz and $2\pi \cdot 1$ kHz respectively, and so the maximum two-photon Rabi frequency at 1 MHz detuning is at least $2\pi \cdot 10$ Hz. In practice our measured maximum two photon Rabi frequency is $2\pi \cdot 70$ Hz on resonance.

Density estimation in the Mott insulator

To perform spectroscopy in the Mott insulator, we load the lattice as described in the previous section to a depth of 150 kHz. At this depth the entirety of the gas is in the Mott insulating regime, and the tunneling time h/J is 290 ms. We then hold the atoms in the lattice while we simultaneously drive a long square pulse of both microwave and RF radiation.

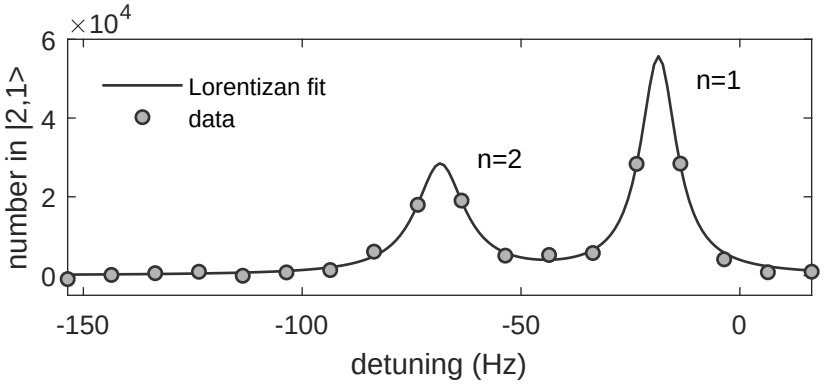

Figure 5.4: Two-photon clock spectroscopy of atoms in a deep optical lattice (V_{532} = 150 kHz). Clear resonance peaks can be seen in the atom number transferred to the $|2,1\rangle$ state (gray dots), corresponding to lattice sites with one and two atoms per site. No higher filling peaks can be seen. The inferred average density is $\bar{n} = 1.2$, and the calculated interaction strength is $U = 2.13$ kHz.

To detect the atoms transferred into the $|2,1\rangle$ state, we simply allow a short time of flight and image the atoms without the usual repump pulse. The atoms in $|1,-1\rangle$ are thus 6.8 GHz off resonant and do not contribute to the absorption signal. Plotted in figure 5.4 is the number of atoms transferred to $|2,1\rangle$ as a function of the detuning of $\omega = \omega_{\mu w} - \omega_{RF}$ from the interaction free resonance, for a pulse time of 50 ms.

Two sharp peaks can be seen, the highest one corresponding to $n = 1$ atoms, and the lower energy one to $n = 2$ atoms. These data are certainly inconsistent with the average filling $\langle n \rangle = 6$, which is inferred from the nearest-neighbor coherence α, shown in figure 5.3. Whilst we do not count the number of unoccupied sites, and such can't directly estimate the density, it is impossible to have an average filling $\langle n \rangle = 6$ without at least some sites occupied by 6 atoms or higher.

Finally, we use the separation of the peaks to estimate U, and compare it to U as calculated from the Wannier functions. Approximating the peaks in figure 5.4 as Lorenztian functions, we extract a difference in frequency of 49.9 Hz, corresponding to $U = 2.13$ kHz. At 150 kHz, the Wannier calculation gives us an estimate of U as 2.29 kHz.

Temperature

As noted previously, thermal occupation of bands of delocalized holes or particles offers a way to increase the coherence of the system. In the work of [69], a maximum increase of α of 28% is observed in a 2D square lattice system at $k_B T \approx 0.1U$ with $n = 1$ filling at the center of a trap. Even taking into account the difference in lattice structure in our experiment, it is unlikely that this mechanism can account for a 250% increase in the value of α. We also never observe the signature increase then decrease in α, which means we are unlikely to be

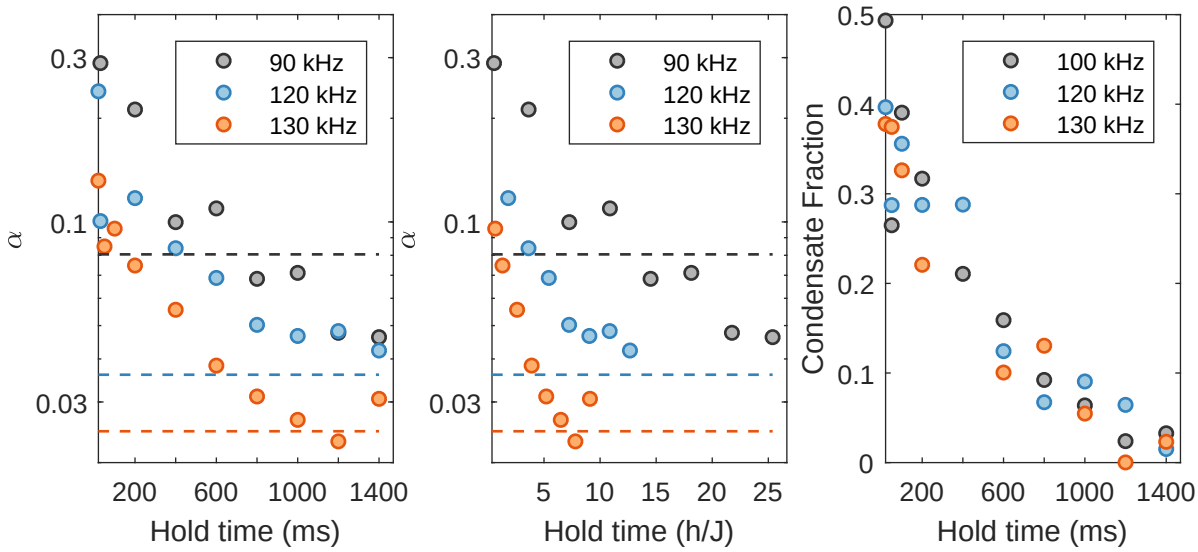

Figure 5.5: Decay of the nearest-neighbor coherence and round-trip condensate fraction. The different color dots correspond to different values of V_{532}. (a) Alpha decreases as the gas is held in the optical lattice. Dashed lines correspond to perturbation theory for $n = 1$. (b) Across a range of lattice depths, the gas takes $\sim 10\,h/J$ to reach the $n = 1$ theoretical value. However at $V_{532} = 90$ kHz, it continues to decay past this value. (c) The round-trip condensate fraction also decreases as we hold the gas, at an approximately equal rate for the three lattice depths considered.

near some maximum due to temperature.

5.5 Out of equilibrium

Lacking a convincing equilibrium explanation of the extra coherence, we study how the gas evolves as a function of time.

Nearest-neighbor coherence α

To test if the nearest-neighbor coherence α is in equilibrium we simply prepare the gas as in section 5.3, and hold for times longer than 30 ms before time of flight. As can be seen in figure 5.5, the coherence clearly has not reached equilibrium as it continues to decay over long timescales. It consistently takes about 10 hopping times h/J for the coherence to reach its expected $\langle n \rangle = 1$ value, over a range of U/J from 105 to 340. This seems like a long timescale for relaxation of a nearest-neighbor measurement, which suggests that this system is relaxing over spatial scales much larger than nearest-neighbor, and so provides the first clue that we may be globally out of equilibrium.

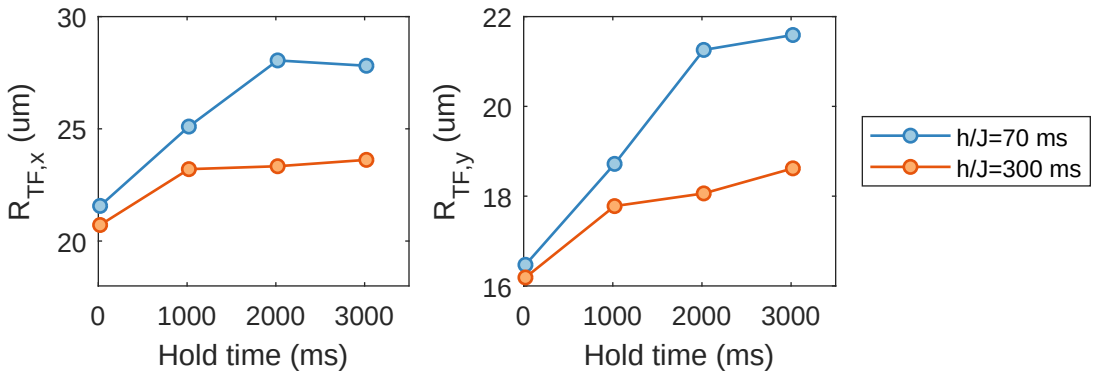

Figure 5.6: Expansion of the gas as it is held in the lattice. The Thomas-Fermi radius increase in both dimensions over long time periods. Expansion happens faster for at 110 kHz (blue) than at 150 kHz (orange).

Additionally, we measure a proxy for the heating by loading the gas, holding for a variable amount of time, and then reversing the loading procedure. In doing this, all of the excitations of the system are mapped to the thermal fraction of the Bose-Einstein condensate, which we measure in figure 5.5. We see a loss in condensate fraction over similar timescales as the loss in coherence α, but we are unable to determine the causal relationship between the two. Is the system out of equilibrium, and as such heating up as the excitations thermalize, or is the gas being heated by the technical noise of the laser, leading to a reduction in α?

Thomas-Fermi radius

To study the global equilibrium properties of the gas, we measure the Thomas-Fermi radius of the gas directly via in-situ imaging. We prepare the gas in the optical lattice as in section 5.3, perform *in-situ* imaging and fit the density with a Thomas-Fermi profile.

The Thomas-Fermi radius grows over long timescales compared to the hopping time h/J, as shown in figure 5.6. The gas expands faster in a 110 kHz deep optical lattice (blue dots) than in a 150 kHz deep optical lattice (orange dots) . If the gas was approximately in equilibrium, and expanding due to heating by the optical lattice, then we would expect the gas in a 150 kHz deep lattice to increase faster as the lattice causes more heating. If the gas was close to equilibrium we would also expect the gas in the 150 kHz lattice to be larger as the interaction strength U is bigger.

We thus conclude that the gas has not reached its equilibrium size, and as such is globally out of equilibrium.

Density

In section 5.4 we identified peaks in the hyperfine spectroscopy that corresponded to single and doubly occupied sites. We track the amplitude of these peaks as a function of time

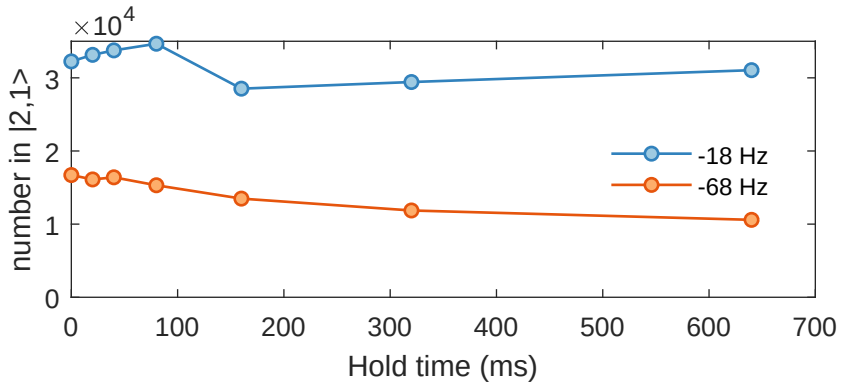

Figure 5.7: Evolution of the $n = 1$ and $n = 2$ hyperfine spectroscopy peaks.

that the atoms are held in the optical lattice. At $V_{532} = 150$ kHz we see the loss of doubly occupied sites, but no increase in singly occupied sites over a timescale $\approx 2 \cdot h/J$, plotting the results in figure 5.7.

Two process can occur in the expansion of a Mott insulator. Doubly occupied sites and unoccupied sites can combine to become two singly occupied sites. If this process occurs the number of singly occupied sites would increase as the number of doubly occupied sites decreases. We do not see any evidence of this process in figure 5.7. However, the Mott insulator can expand by singly occupied sites moving into the region of unoccupied sites. The two photon spectroscopy measurements tell us nothing about this second process.

If the singly occupied sites were expanding into the unoccupied region, they would become increasingly surrounded by unoccupied site. This would likely increase, not decrease their contribution to the nearest-neighbor coherence. This second model of expansion appears inconsistent with the decrease in α in time we observe . Ultimately we cannot conclude if the gas is expanding or not from this data, but we can conclude that the distribution of atom numbers per site is approximately constant.

Local equilibrium

The quantum adiabatic theorem tells us that the system remains in its ground state if the system is gapped, and we vary the parameters sufficiently slowly [27]. At the beginning of our lattice loading ramp, the system is a gapless superfluid, so there is no way to perfectly satisfy this theorem.

In practice, we simply ensure that the change in the system parameters are slow compared to fixed energies of the system [27]. This is approximately the same as remaining adiabatic with respect to the energies of a single site model . From largest to smallest, these energies are the band gap ω_0, the interaction strength U, the trap frequencies ω_i and the tunneling energy J. Adiabaticity with respect to the first three is easily satisfied, but the exponential suppression of J with the lattice depth possibly poses a challenge. We have calculated the

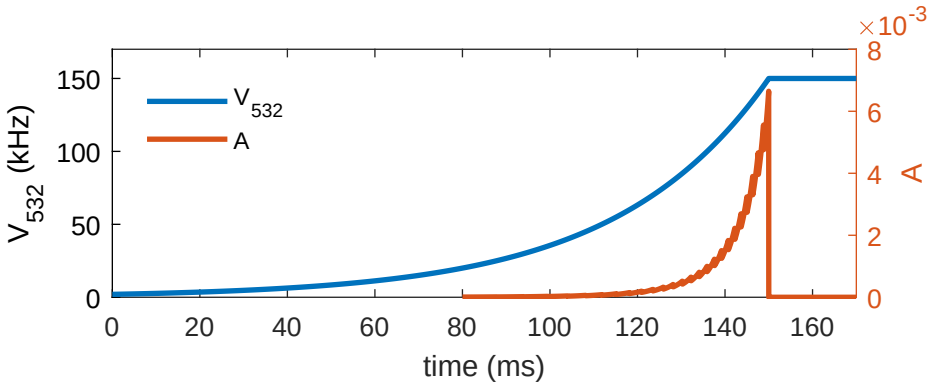

Figure 5.8: Adiabaticity of loading the 532 nm triangular optical lattice. Depth of the 532 nm lattice (blue) is shown for the second section of the ramp described in section 5.3. The adiabaticity parameter (orange) remains below 10^{-2} throughout the ramp.

adiabaticity parameter [27],

$$A = \frac{\dot{J}}{J^2}, \tag{5.28}$$

for the the ramp described in section 5.3 assuming loading to the largest lattice depth considered in this work. Even with an exponential increase in the lattice depth to 150 kHz, the adiabaticity parameter A remains below 10^{-2}, thus satisfying the requirement that $A \ll 1$ [27].

Whilst we conclude from this analysis that the system is locally adiabatic, we nevertheless adopt a 'safer' ramp scheme. The 532 nm lattice is subsequently loaded exponentially to 90 kHz, then linearly to 150 kHz over 70 ms. This reduces the maximum adiabaticity parameter to 10^{-3}. This increase in local adiabaticity has no effect on the effective $\langle n \rangle$ we see in measurements of the nearest-neighbor coherence α.

Global equilibrium

We have few pieces of evidence supporting the conclusion that the gas is locally in equilibrium. The distribution of atom numbers per site is approximately constant, as shown by two-photon spectroscopy. Additionally a single-site measure of adiabaticity is satisfied by our lattice loading ramps. Now we informally consider the question of global equilibrium by simply considering one aspect of the system, the global density distribution.

A superfluid has Thomas-Fermi profile introduced in chapter 2, with a Thomas-Fermi radius $R_{TF,i}$ in direction i determined by the central chemical potential μ_0,

$$R_{TF,i} = \sqrt{\frac{2\mu_0}{m\omega_i^2}}. \tag{5.29}$$

The chemical potential μ of a lattice trapped gas depends on the interaction strength U as

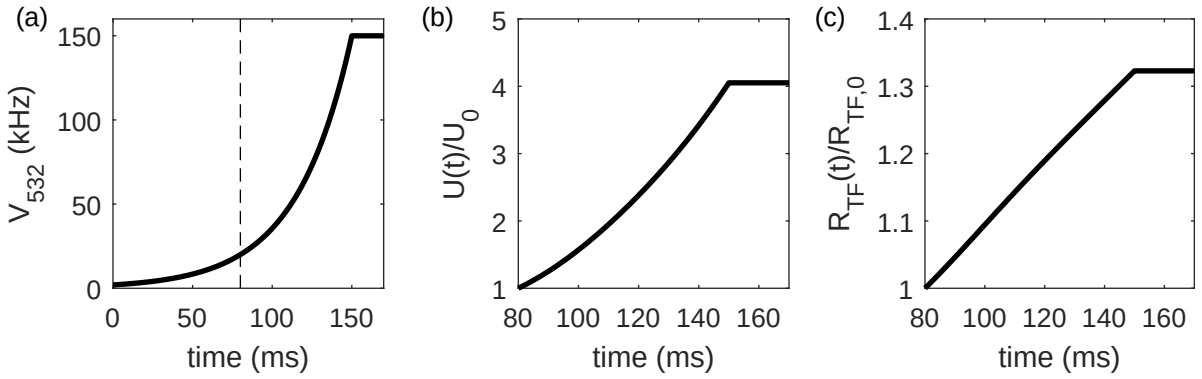

Figure 5.9: Predicted expansion of the Thomas-Fermi radius of the gas during lattice loading. (a) Loading profile of the 532 nm lattice. After the dashed line (80 ms), the lattice depth is sufficiently high to trust calculations of U. (b) Relative increase of the interaction strength from its value at 80 ms. (c) Relative increase in the Thomas-Fermi radius from its value at 80 ms.

$$\mu \propto U^{2/5} \tag{5.30}$$

When the lattice depth is increased, the Wannier function is compressed, increasing the interaction strength U, which in turn increases the chemical potential and thus the Thomas-Fermi radius. Thus as we load the optical lattice, the equilibrium size of the gas expands.

How U and thus R_{TF} changes throughout the lattice ramp is shown in figure 5.9. Changes in the interaction strength and equilibrium Thomas-Fermi radius are shown relative to their value at 80 ms, where $V_{532} > 20$ kHz. Below this level the system is not well described by the Bose-Hubbard model as the next order terms are too high. As a result, we expect the gas to increase as we increase the lattice depth. We only see an expansion over very long times in figure 5.6.

This analysis is a substantial oversimplification, as the trap frequencies are increasing in the data we consider, due to the radial confinement of the vertical lattice, and increase in the dipole trap power. At some point in the load time, the adiabaticity in the vertical direction is broken to separate the atoms into separated systems.

A detailed analysis shows that these increases are not sufficient to cancel the expansion of the gas in all three dimensions. We still expect to see an increase in the Thomas-Fermi radius, and only do so over very long timescales. We believe that this means that when we measure the nearest-neighbor coherence, the gas has not reached it's equilibrium density distribution. Even though we are using the Thomas-Fermi profile of a superfluid to model the density of a Mott insulator, we still expect this expansion to occur.

We note an experiment performed in Chicago describing the observation of extremely slow equilibration to the 'wedding cake' profile after crossing the superfluid-to-Mott insulator transition [36]. As with our procedure they describe a locally adiabatic lattice loading

sequence, and observe global density redistribution up to 100 tunneling times h/J after the lattice is loaded. One explanation for this slow relaxation is the formation of Mott domains that inhibits transport across the lattice [53]. Similar inhibition of transport could explain the long timescales we observe, but the connection to the coherence is still unknown.

5.6 New potentials for equilibrium

Having identified the changing extent of the gas as a likely candidate for the non-equilibrium value of α, we develop a procedure to keep the Thomas-Fermi radius constant through the lattice ramp. We drastically simplify the potentials in which we begin the lattice loading, then add another potential that we can tune to keep the radius constant.

Simpler potentials

In the experiment detailed in section 5.3, the Thomas-Fermi radii in each of the three dimensions increase by different amounts as we load the lattice. Compensating the increase of all three radii simultaneously is challenging, so we simplify our initial potentials so that the gas does not expand in the vertical direction, and expands symmetrically in plane.

After evaporatively cooling to quantum degeneracy in the hybrid magnetic-optical potential, we load the vertical lattice to a depth of 50 kHz. At the end of the ramp, the tunneling time $1/J$ between layers is 400 ms, and so the vertical number distribution is fixed. We then smoothly ramp off the magnetic quadrupole field and crossed dipole traps over 50 ms.

As each pancake has trap frequencies $\omega_x = \omega_y = 2\pi \cdot 61$ Hz and $\omega_z = 2\pi \cdot 22$ kHz, and $\hbar\mu, k_B T \ll \hbar\omega_z$, each layer is an independent, radially symmetric two dimensional system. When the lattice is loaded the gas will only expand symmetrically in the radial direction, so we have drastically simplified the problem of keeping the extent of the gas constant. In 2D, the radial Thomas-Fermi radius R_{TF} is proportional to

$$R_{TF} \sim \left(\frac{U}{\omega_R^2}\right)^{1/4} \tag{5.31}$$

where $\omega_R = \omega_x = \omega_y$. Thus all we need to do is keep U/ω_R^2 constant throughout the ramp. The dependence of U on the in-plane lattice depth V is $U \sim V^{1/2}$, so this will approximately require us to scale the radial trap frequency as $\omega_R \sim V^{1/4}$. We note that these relationships are only true in the tight binding limit, so in low lattice depth regime the relationship will need to be numerically calculated.

Compensation beam filling

We have a number of methods available to us to increase the radial trap frequency through the loading process, but we felt the simplest from a control perspective was to add another potential. We co-propagate a second 1064 nm beam along the vertical lattice, with orthogonal

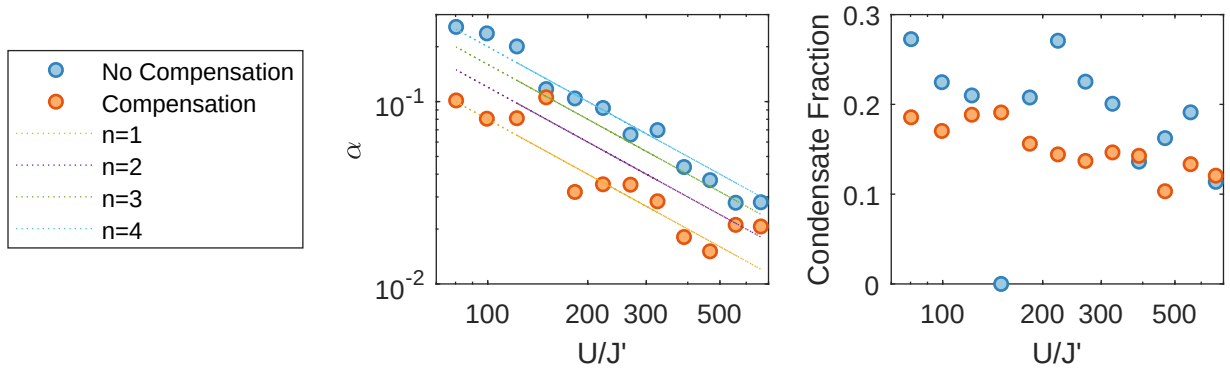

Figure 5.10: A direct comparison of a compensated and uncompensated triangular lattice. Two back-to-back data sets taken under identical conditions except that the expansion compensation is applied in the orange data, and not in the blue. The compensation causes a drastic decrease in α, moving it close to the value predicted by $n = 1$. There is a slight decrease in the condensate fraction due this technique.

polarization, and detuned by 30 MHz. This beam is not retroreflected, so simply provides an attractive Gaussian potential of equal waist to the vertical lattice. In comparison to our previous intensity stabilization schemes, this system uses a linear (not logarithmic) photodiode.

An arbitrary waveform generator (Agilent 33220A) generates the voltage setpoints for the intensity servo throughout the lattice loading sequence. At the start of each experimental cycle a MATLAB scripts reads in the upcoming lattice ramp details over serial and generates a voltage ramp for the compensation beam intensity that keeps the Thomas-Fermi radius constant. This script interpolates a table of Thomas-Fermi radii at different trap frequencies and interaction strengths generated by a numerical ground state calculation done by Zephy Leung. This calculation is valid in the low to medium lattice depth range, but doesn't take into account the Mott insulating transition.

Constant Thomas-Fermi results

Finally, we determine the effect of applying expansion-compensating curvature on the nearest-neighbor coherence. We first look a direct comparison of a gas with identical starting conditions, where we apply the curvature or override it off, shown in figure 5.10. Applying the curvature clearly reduces the nearest-neighbor coherence, despite the increased density caused by the extra curvature. The compensated data follow the $n = 1$ theoretical curve, consistent with the expected density. There is a small increase in the heating of the gas, resulting in a slightly lower condensate fraction. Some of this heating may be due to a problem discovered after taking this data, whereby the vertical lattice and compensation beams drifted relative to each other, resulting in a gradient in addition to curvature. We saw clear evidence later on that large separations lead to substantial heating.

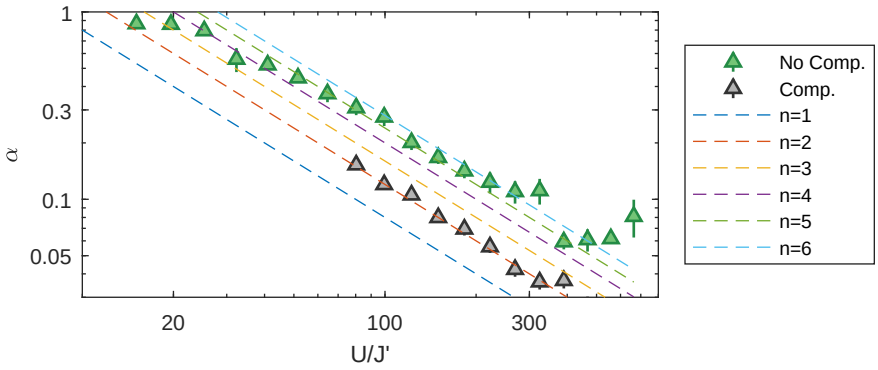

Figure 5.11: Comparison of triangular lattice data sets taken in January (green) and August (gray). The January data set was taken with an asymmetric and uncompensated potential with an average filling of 0.3 , whilst the August data were taken with a symmetric compensated potential, at an average filling of 0.9.

Finally we show the effect of all of our changes to the experiment in figure 5.11, from the simpler potentials to the compensating curvature. Here we have resolved the drift of the compensation beam relative to the vertical lattice. Clearly the coherence has been substantially reduced, and we get a result much closer to its equilibrium value.

Final triangular data analysis

We examine this final triangular data set in more detail to determine how large a discrepancy between theory and experiment remains. We first extract the power law dependence by fitting $\log(\alpha)$ and $\log(U/J')$ with a linear function. Fitting α and $(U/J)'$ directly weights the largest values most strongly, whereas fitting in log space weights the values equally. The results of fitting the entire data set directly are show in figure 5.12, where we find an exponent of $-1.01 \pm (0.03)$. This is very much consistent with the prediction from perturbation theory.

Having validated the power law behavior, we calculate the density of each realization of the experiment via $\langle n \rangle = \alpha/(4U/J) - 1$. The mean value of this data set is $\langle n \rangle = 2.03 \pm 0.07$. Finally, we compare the experimental values of α against those for the expected density $\bar{n} = 0.9$. The data set averaged uncertainty in the lattice depth is 7%, leading to a 40% uncertainty in U/J. The uncertainty due to the lattice depth is shown as dashed lines in figure 5.12. This leads to a value of $\langle n \rangle = 2^{+1.2}_{-0.9}$, which only slightly disagrees with our expected value $\langle n \rangle = 0.9$, shown in blue.

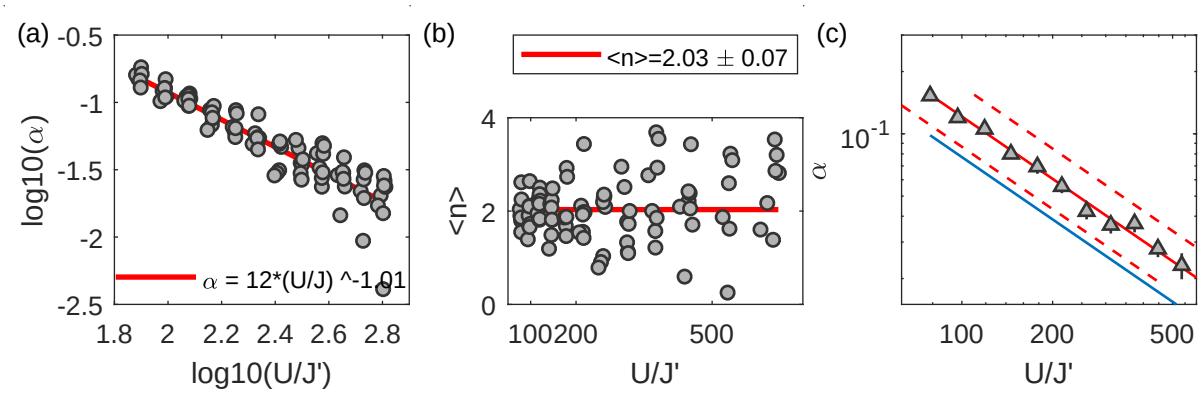

Figure 5.12: Analysis of the August triangular data set. (a) Power law fitting of triangular data. Data points represent individual realizations of the experiment. The extracted exponent is $-1.01 \pm (0.03)$, consistent with the perturbation theory result -1. (b) Extraction of the average density. We calculate the average density of each realization of the experiment using equation 5.21. (c) Comparison of theoretically predicted data α for the expected density $\bar{n} = 0.9$ (blue) and experimental realization (red) where dashed lines represent the uncertainty in the lattice depth.

Chapter 6

The trimerized kagome lattice

6.1 Introduction

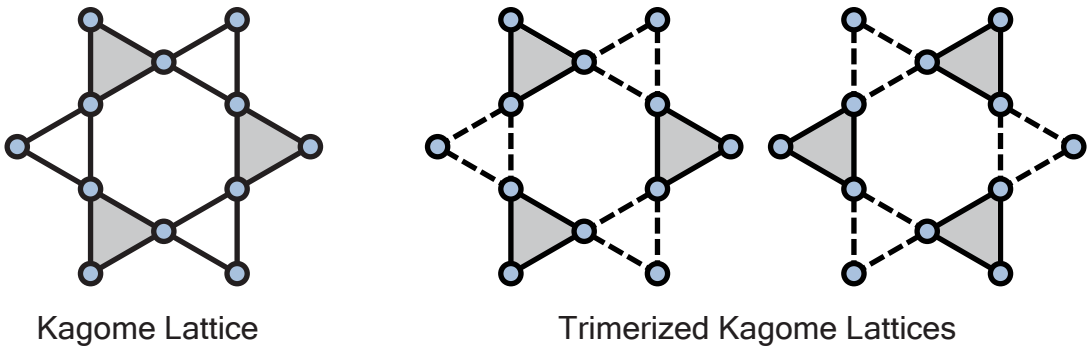

Figure 6.1: The kagome lattice and its trimerized variants. The kagome lattice is a triangular lattice of corner sharing triangles. Plaquettes of right facing triangles are emphasized in gray. For the trimerized kagome lattice (TKL), connections inside right facing triangles have a different coupling strength than connections in left facing triangles. The two variants are either right facing triangles (emphasized in gray) strongly bonded (bold lines) or left facing triangles (emphasized in gray) strongly bonded.

In this section we describe a newly realized optical lattice potential, known as the trimerized or breathing kagome lattice, shown in figure 6.1. This is a triangular lattice of triangular plaquettes, where the intra-trimer couplings J are stronger than the couplings between different trimers J'. In the limit $J \gg J'$ this describes a set of isolated triangular plaquettes, and for $J = J'$ this becomes a regular kagome lattice [59].

The kagome lattice has long been of interest because antiferromagnetic couplings on this lattice are naturally frustrated , meaning no single spin configuration has the lowest energy [56]. Consider the classical Heisenberg model on a kagome lattice with anti-ferromagnetic couplings, with the Hamiltonian

$$H = -J \sum_{\langle ij \rangle} \boldsymbol{s}_i \cdot \boldsymbol{s}_j, \tag{6.1}$$

In each triangle the energy is minimized if the vector sum of the spins is zero. Because the triangles only share corners, choosing a configuration in one triangle does not uniquely determine the configuration on an adjacent triangle. As such there is an infinite number of spin configurations of equal energy in the ground state [57]. It is this massive degeneracy, or spin frustration, that makes the kagome lattice of such interest.

Whilst the classical Heisenberg antiferromagnet demonstrates the spin frustration of the kagome lattice, it is the quantum antiferromagnet that is the true source of interest. The ground state nature of the quantum antiferromagnet on the kagome lattice has been studied extensively after it was proposed to be a resonant valence bond state [58, 18]. After 30 years there is still disagreement on the exact ground state of this system [16], but we note one particular motivating insight. In [50], it is argued that studying the same problem on a trimerized kagome lattice is far more tractable theoretically, yet reproduces much of the known numerics for the kagome lattice.

Studying a system of weakly coupled subsystems composed of strongly coupled few-body states is just as attractive experimentally as it is theoretically. There are many tools experimentally for the preparation and study of few body states, and so being able to connect these controllably and weakly a promising idea [71, 51].

$J < 0$ orbital frustration

As we introduced in chapter 2, our ultracold atoms in optical lattices form a Bose-Hubbard model on the (trimerized) kagome lattice, not a Heisenberg quantum antiferromagnet. I will first describe how we could access the physics of frustration.

Considering just the hopping term of the Bose-Hubbard Hamiltonian $H_{Hop} = -J \sum_{\langle ij \rangle} b_i^\dagger b_j$, we can see an analog to an in-plane magnet. $J > 0$ is 'ferromagnetic' as it favors the same phase of the wavefunction on adjacent sites whilst $J < 0$ is 'antiferromagnetic' as it favors the opposite phase. The ground state of the hopping Hamiltonian has an infinite number of states for $J < 0$ on the Kagome lattice. As with the classical antiferromagnet, the energy in each triangle is minimized when the the sites of the triangle are 120° out of phase with each other. Again this doesn't sufficiently constrain adjacent triangles, and as such we end up with infinite degeneracy.

When considered from a band structure perspective, the $J < 0$ kagome lattice has a 'flat band' in the ground state, i.e. all momentum states are of equal energy [64]. In this analogy, we see how the physics of spin frustration turns up in the band structure of the kagome lattice. Our optical lattice naturally corresponds to the $J > 0$ ferromagnetic case, where the orbital frustration turns up in the highest s-band. In future works we hope to study this orbital frustration.

$J > 0$: Fractional Mott insulator

The trimerization of the kagome lattice allows us to break down the problem of spin frustration into exactly solvable strongly coupled systems, which are all weakly coupled to one another. We can apply the same break down to the unfrustrated trimerized kagome lattice, where $J > 0$. We explore this not in the language of spin, but the regular Bose-Hubbard language of density and coherence.

This trimerization leads to a new type of Mott insulating state where there is exactly integer atom number per trimer, rather than per site [14]. As a consequence the filling per site is fractional rather than integer. When the tunneling inside the triangular plaquette is sufficiently strong, the atoms are delocalized over the three sites even in the presence of interactions. Thus there is always an interaction energy cost $\sim U/3$ to adding another atom to a plaquette, which can be much greater than the weak tunneling energy J'. This energy cost stabilizes a state of constant particle number per plaquette, thus giving us the fractional Mott insulator state. It should be noted whilst the average filling per site is fractional, there is no relation to fractionalized excitations like in the fractional quantum hall effect.

This new state has some interesting properties: the number fluctuations on a given site are large, but the number fluctuations for a trimer are small. This state is an insulator and has no long range coherence, but it can have strong coherence at short range.

Throughout this chapter we describe the experimental realization of a Bose-Hubbard model for an unfrustrated trimerized kagome lattice, and study its phase coherence properties.

6.2 Realizing the trimerized kagome lattice

We follow our general prescription for realizing the Bose-Hubbard model on a specific lattice: identify an appropriate potential, generate the s-band Wannier functions, and then derive the Hubbard parameters.

Potential

The trimerized Kagome lattice is one of the specific configurations of our optical superlattice, where the 532 nm lattice is polarized in-plane, and the 1064 lattice is polarized out of plane, as shown in figure 6.2. The explicit potential is given by

$$\begin{aligned} V_{\pm}(\boldsymbol{r}) = &\tfrac{2}{9}V_{532}\left(3 - \cos(2\boldsymbol{G}_1\cdot\boldsymbol{r}) - \cos(2\boldsymbol{G}_2\cdot\boldsymbol{r}) - \cos(2\boldsymbol{G}_3\cdot\boldsymbol{r})\right) \\ &- \tfrac{1}{9}V_{1064}\left(3 + 2\cos(\boldsymbol{G}_1\cdot(\boldsymbol{r}\pm\boldsymbol{\delta}) + 2\cos(\boldsymbol{G}_2\cdot(\boldsymbol{r}\pm\boldsymbol{\delta})) + 2\cos(\boldsymbol{G}_3\cdot(\boldsymbol{r}\pm\boldsymbol{\delta}))\right) \end{aligned} \tag{6.2}$$

where $\boldsymbol{\delta} = a(\frac{1}{2\sqrt{3}}, 0)$, and as before V_{532} and V_{1064} are the peak-to-peak potential depths of the 532 nm and 1064 nm lattices respectively. Each of these two lattices form a triangular lattice of potential minima, of spacings 355 nm and 710 nm respectively. A trimerized Kagome lattice is formed when the 1064 minimum is positioned equidistant from three 532

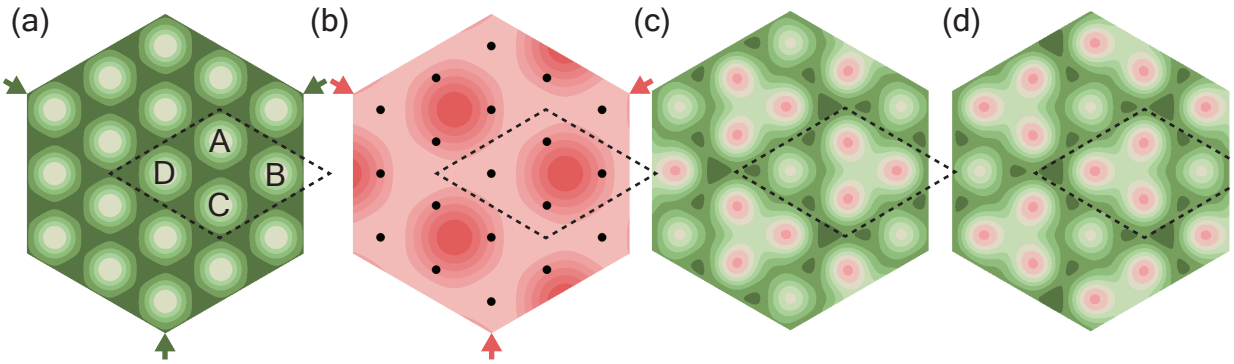

Figure 6.2: The underlying superlattice potentials of the right trimerized kagome lattice. (a) A triangular lattice of spacing 355 nm is formed by in-plane polarized 532 nm light. The sites of the 2×2 unit cell are labeled A-D. (b) A second triangular lattice with spacing 710 nm is formed by out-of-plane polarized 1064 nm light. In this trimerization the the 1064 nm minimal lie in the center of three 532 nm minima (black dots) which form a right facing triangle. (c) Final combined potential of the right trimerized kagome lattice. (d) Final combined potential of the left trimerized kagome lattice for comparison.

nm minima, and we note that there are two such patterns. As seen in figure 6.2 one occurs with the 1064 minimum at the center of sites A, B and C, which form a right facing triangle. The other trimerization (figure 6.2(d)) is formed with the 1064 minimum at the center of A, C and D sites, which form a left facing triangle.

The 1064 nm potential detunes sites A, B and C from D by $\Delta V = \frac{1}{2}V_{1064}$. As shown in previous work this detuning must be larger than the chemical potential μ for the D site to be unoccupied, and the Kagome lattice faithfully realized [39]. The trimerization of the tunneling elements can easily be seen by looking at the potential cut-through in figure 6.3. The energy barriers between sites in a common triangle are reduced by $\sim \frac{1}{2}V_{1064}$, whilst the barriers between sites of different triangles are increased by $\sim \frac{1}{2}V_{1064}$. These reduced and increased potential barriers lead to exponentially stronger and weaker tunneling respectively.

There is also a small modification in the location of the minima, as the the 1064 nm potential has a gradient at the 532 minima. This is a relatively small effect, but care must be taken in quantitative analyses that rely on the position of the sites, such as the $\tilde{P}$ measurements in the work of Jo et. al. [39].

Hubbard parameters

We numerically generate the ground band Wannier functions and derive the Hubbard parameter using the MATLAB package "Wannier states for optical lattices", produced by the Jaksch group at Oxford [40]. In figure 6.4 we show the values of the Hubbard parameters extracted from these calculations, assuming a 50 kHz vertical lattice depth.

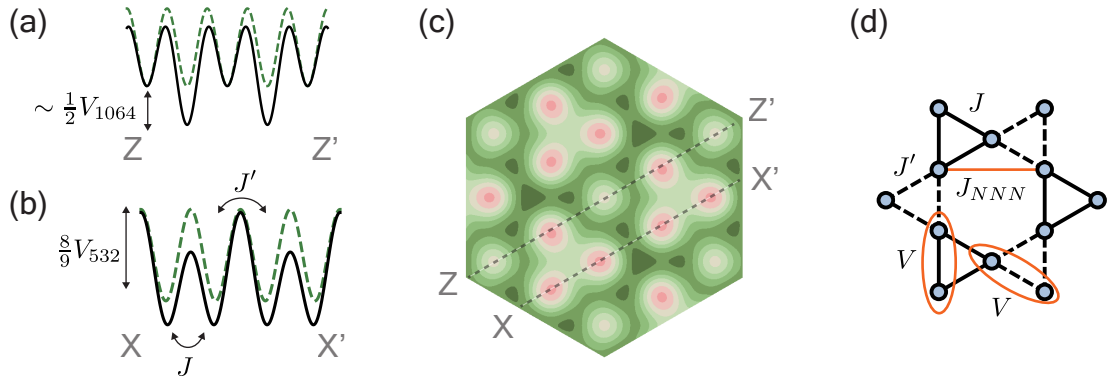

Figure 6.3: Cut-through of left trimerized kagome lattice potential. (a) Trimerized kagome lattice potential (black) and 532 nm triangular potential (green dashed) along X-X'. The excluded site is detuned by $\Delta V \sim \frac{1}{2}V_{1064}$. (b) The same potentials along cut-through Z-Z'. The 1064 nm potential reduces the barrier between sites inside the triangle, and increases it between sites of different triangles, leading to strong tunneling J and weak tunneling J'. (c) Left trimerized kagome lattice potential. (d) Bose-Hubbard model derived from this potential. The non-Hubbard terms V and J_{NNN} are shown in orange, and discussed in section 6.2.

We see that we can independently tune the ratios U/J and J/J' by appropriate choice of V_{532} and V_{1064}, and we have access to a number of distinct regimes:

- $U \gg J \gg J'$ Strongly interacting, strongly trimerized
- $U \gtrsim J \gg J'$ Moderately interacting, strongly trimerized.
- $U \gg J \gtrsim J'$ Strongly interacting, weakly trimerized.
- $U \gtrsim J \gtrsim J'$ Moderately interacting, weakly trimerized.

To ensure we have correctly realized a Bose-Hubbard model, we look at the next order terms: the next-nearest neighbor tunneling J_{NNN} and the nearest-neighbor interaction V. For the $V_{532} > 40$ kHz considered in this calculation, all values of V_{1064} have $J_{NNN} \ll J'$, which is sufficient to neglect J_{NNN}. The nearest-neighbor interaction splits into two cases: interactions within the same triangle, and interactions between different triangles. The latter are always 100 times smaller than J', sufficient to neglect them completely. However, the intra-trimer interactions can be larger than J' for strong trimerizations. As these interactions will only modify the local trimer wavefunction to a small degree, and cause no other coupling, they can also be neglected.

Some of the data points in figure 6.4 are missing, where the calculation hasn't converged to a sufficiently symmetric solution after a number of repetitions. This appears to happen when $V_{1064} = V_{532}$, which is where the tunneling barrier between sites in the triangle gets

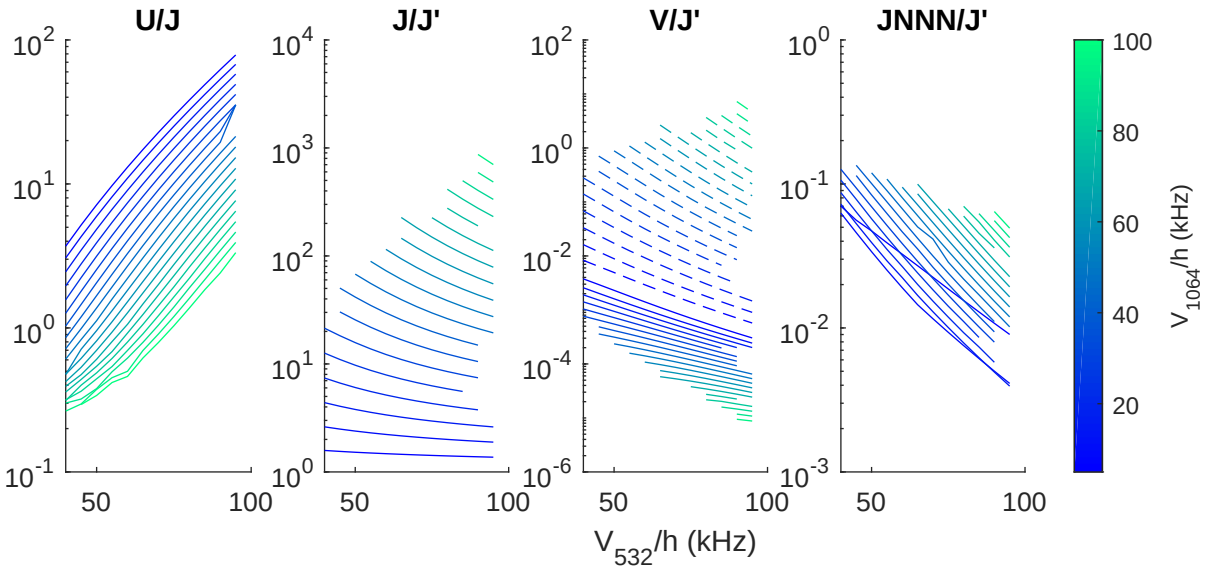

Figure 6.4: The Hubbard energies for the trimerized kagome lattice as calculated by the "Wannier states for optical lattices" package [40]. We assume a 50 kHz vertical lattice depth. (a) Ratio of interaction energy U to strong tunneling J. (b) The trimerization ratio, strong tunneling J to weak tunneling J'. (c) Ratio of nearest-neighbor interaction V to the smallest Bose-Hubbard energy J'. Dashed lines are nearest-neighbor interactions inside the same triangle,which can be comparable to the weak tunneling J'. Solid lines are for interactions between different triangles, which can always be neglected. (d) Ratio of the next-nearest-neighbor tunneling J_{NNN} to J'. This is always small enough to ignore in the range of lattice depths considered.

small. The trimer collapses to a single well at $V_{1064} = 2.5V_{532}$, but before that point the individual sites are not well resolved, and likely the tight binding approximation breaks down. Thus we avoid points with $V_{1064} > V_{532}$.

In summary, as long as we work with $V_{532} > V_{1064} > \mu$, and $V_{532} > 40$ kHz, we should faithfully realize a Bose-Hubbard model. Given the exponential suppression of the tunneling energy, we have substantial freedom in choosing U, J and J'.

6.3 A Bose-Einstein condensate in an trimerized kagome lattice

Thus far we have argued that an idealized optical lattice potential realizes the Bose-Hubbard model on a trimerized kagome lattice. Now we verify our faithful realization of this potential using a weakly interacting Bose-Einstein condensate.

The trimerized kagome lattice potential, displayed in equation 6.2 has many factors that

are easy to write down but challenging to realize in practice. We require that the intensities of the three beams of each color are equal, do not fluctuate significantly, and can be controlled arbitrarily. The wavevectors of the 532 nm and 1064 nm beams must be highly co-linear, and the relative phases of the two lattices must be controlled arbitrarily, and do not fluctuate too much.

We discussed the solution to many of these challenges in chapter 3, but here we focus on the relative phase control of the optical lattices: how we control and set the phase, as well as the physical effect of finite phase fluctuations.

Finding the trimerized kagome lattice

In general we begin a day's experiments with a randomized but stable phase relationship between the 532 nm and 1064 nm lattice. We get no direct information about this phase relationship from our interferometer, so we need to use the atoms to determine and adjust this relationship it until we reach the trimerized kagome lattice. Our primary technique for doing this is the superfluid diffraction of a Bose-Einstein condensate in an optical lattice.

We load a bichromatic triangular optical lattice in a similar method as described later in section 6.5 but without a lattice in the vertical direction. This realizes a two dimensional lattice of tubes, where the filling is high and the interactions are sufficiently weak to ignore. The lattice is loaded to $V_{532} = 45$ kHz and $V_{1064} = 15$ kHz where we satisfy the tight binding requirement, and chemical potential requirement as dictated above, but the tunneling energy scales are high. All potentials are turned off, and the gas is release in time-of-flight.

We use the symmetry in the superfluid diffraction pattern to determine how to adjust the relative phases of the two lattices as described in section 4.1. Follow the description in figure 6.5.

Verifying two different trimer patterns

There are two different trimerization patterns, either strong bonding on a left or right facing triangle. Whilst the Bose-Hubbard physics of these two patterns are identical, we demonstrate our ability to deterministically prepare and detect each pattern.

Ground state momentum distribution

The superfluid diffraction pattern of the $\boldsymbol{q} = 0$ ground state of both lattices are independent of the trimerization ratio J/J', and identical to the diffraction pattern of a Kagome lattice. The momentum distribution of a superfluid is still described by equation 5.2, but now as the coherence length is infinite, this becomes an infinite sum, and so we need to consider all terms in

$$n(\boldsymbol{k}) = |\tilde{w}(\boldsymbol{k})|^2 \sum_{i,j} e^{-i\boldsymbol{k}\cdot(\boldsymbol{r}_i - \boldsymbol{r}_j)} \langle b_i^\dagger b_j \rangle. \tag{6.3}$$

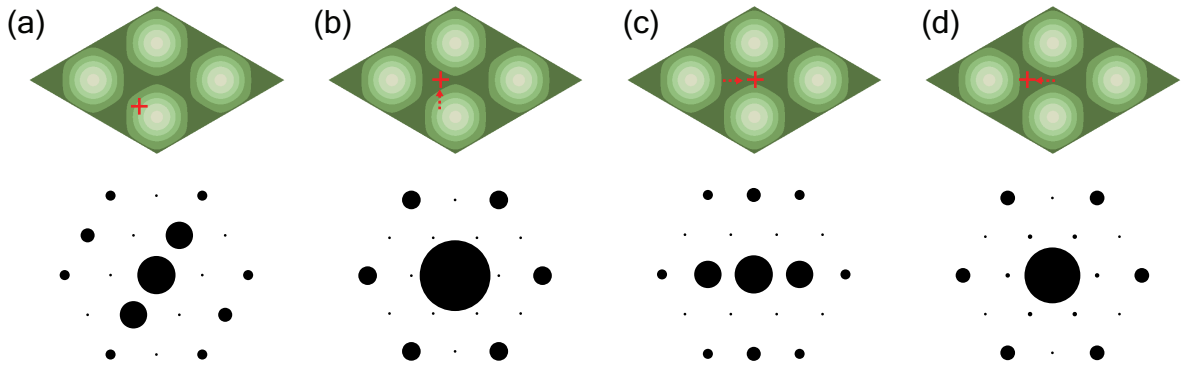

Figure 6.5: Position of the 1064 nm minimum inside the unit cell, and the corresponding diffraction peak population. (a) A random minimum position (red), with left-right diffraction peak asymmetry. (b) The position of the minimum is adjusted up/down to create a left-right symmetric image. (c) The minimum is adjusted left-right until the horizontal 1D stripe diffraction pattern is obtained. (d) The left trimerization is obtained by moving left from the 1D stripe. The right trimerization is obtained by moving right.

In a system with multiple sites per unit cell, the sites are given by $\boldsymbol{r}_{i,\alpha} = i_1\boldsymbol{a}_1 + i_2\boldsymbol{a}_2 + r_\alpha$,where $\boldsymbol{r}_\alpha$ are the displacement vectors for the unit cell, and ψ_α is the wavefunction on each site. Substituting this into the above momentum distribution gives

$$n(\boldsymbol{k}) = |\tilde{w}(\boldsymbol{k})|^2 \sum_{i_1,i_2,j_1,j_2,} e^{-i\boldsymbol{k}\cdot((i_1-j_1)\boldsymbol{a}_1+(i_2-j_2)\boldsymbol{a}_2)} \sum_{\alpha,\beta} e^{-i\boldsymbol{k}\cdot(\boldsymbol{r}_\alpha-\boldsymbol{r}_\beta)}\psi_\alpha^\dagger\psi_\beta \tag{6.4}$$

The first infinite sum is only non-zero if $\boldsymbol{k}$ is a multiple of a reciprocal lattice vector $\boldsymbol{G}_i$. In that case, it is equal to the number of plaquettes in the system N_{plaq}, and as such the momentum distribution is a set of delta functions

$$n(\boldsymbol{k}) = N_{plaq} \sum_i n_{\boldsymbol{k}} \delta(\boldsymbol{k} - \boldsymbol{G}_i) \tag{6.5}$$

where the weights of each delta function are $n_{\boldsymbol{k}} = |\tilde{w}(\boldsymbol{k})|^2|\sum_\alpha \psi e^{-i\boldsymbol{k}\cdot\boldsymbol{r}_\alpha}|^2$. In the ground state, the coherent state amplitude is $\psi_\alpha = \sqrt{n_\alpha}$ where n is the average number of atoms in site α. In the kagome lattice, and its two trimerized variants the populations have the same $n_A = n_B = n_C = n$, and the displacement vectors are the same. Thus the ground state diffraction patterns are the same. The exact strengths of the different momentum peaks are calculated in Claire Thomas's [66], and Jennie Guzman's theses [32]. For the purposes of this discussion, we note that in the ground state the densities at $\pm\boldsymbol{G}_1$ are the same,

$$n_{\boldsymbol{G}_1} = n_{-\boldsymbol{G}_1} = n|\tilde{w}(\boldsymbol{k})|^2|1 + 2e^{i\pi}|^2 = n|\tilde{w}(\boldsymbol{k})|^2 \tag{6.6}$$

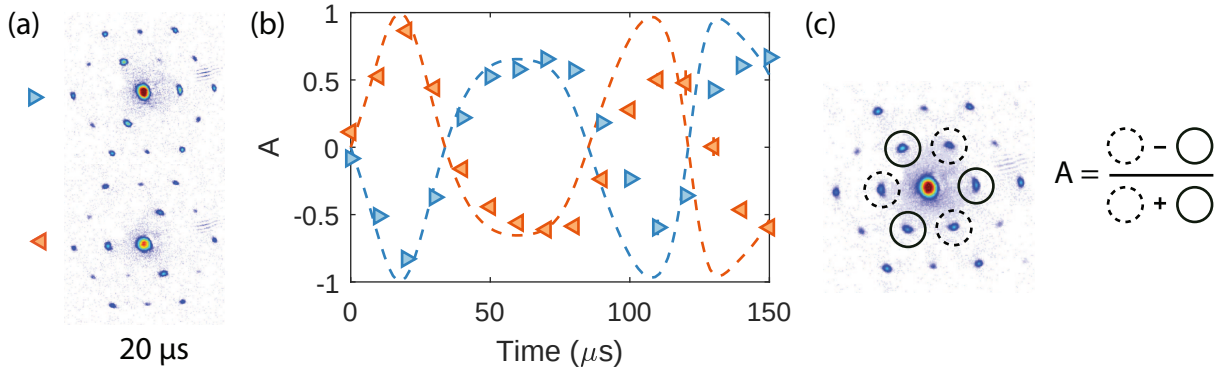

Figure 6.6: (a) Strong asymmetry between $\boldsymbol{k}$ and $-\boldsymbol{k}$ in the first order diffraction peaks. 20 μs of evolution in the 1064 nm only potential is sufficient to clearly distinguished between trimerizations. (b) Oscillations of the asymmetry parameter $\mathcal{A}$ for the two trimerizations. Blue right-facing triangles correspond to the right trimerization, and orange left-facing triangles correspond to the left trimerization. The dashed lines are zero free parameter non-interacting band structure theory. (c) How $\mathcal{A}$ is calculated. The total population in the three dashed circles is counted, as is the population in the three solid circles. $\mathcal{A}$ is the difference over the sum.

Trimer oscillations

To differentiate the two trimerization patterns, we develop an atom optics technique to imprint the inversion asymmetry of the lattice onto the diffraction pattern. We load the trimerized Kagome lattice as above, again to a depth of $V_{532} = 45$ kHz, $V_{1064} = 15$ kHz. We then turn off the 532 nm lattice, and allow the gas to evolve for a time τ in the 1064 nm potential, before we perform time-of-flight measurements.

The diffraction pattern obtained from this technique is shown in figure 6.6 for $\tau = 20$ us. We still see diffraction peaks at the same reciprocal lattice vectors as the ground state momentum distribution, but the amplitude of the first order peaks quickly develops an asymmetry between $\boldsymbol{k}$ and $-\boldsymbol{k}$. Most importantly this asymmetry is opposite for the two trimerization patterns, allowing us to easily tell them apart.

We extract the populations in the first order peaks $P_{\boldsymbol{G}_i}$, and following our previous work on momentum space inversion asymmetries, we construct the following asymmetry parameter:

$$\mathcal{A} = \frac{(P_{-\boldsymbol{G}_1} + P_{-\boldsymbol{G}_2} + P_{-\boldsymbol{G}_3}) - (P_{\boldsymbol{G}_1} + P_{\boldsymbol{G}_2} + P_{\boldsymbol{G}_3})}{(P_{-\boldsymbol{G}_1} + P_{-\boldsymbol{G}_2} + P_{-\boldsymbol{G}_3}) + (P_{\boldsymbol{G}_1} + P_{\boldsymbol{G}_2} + P_{\boldsymbol{G}_3})}. \tag{6.7}$$

In figure 6.6 we plot $\mathcal{A}$ against the the evolution time τ and see that it oscillates in a way that is equal and opposite for the two trimerization patterns.

Theory comparison

We compare our results to a non-interacting band structure calculation. We find the $\boldsymbol{q} = 0$ ground state of the trimerized kagome lattice by diagonalizing a momentum space Hamiltonian generated from the exact potential equation 6.2 using the same method described in Claire Thomas's thesis [66]. We also diagonalize a similar Hamiltonian but with $V_{532} = 0$, project the trimerized kagome lattice ground state onto the eigenstates of this Hamiltonian, and evolve the eigenstates at their eigenenergies. We construct the asymmetry parameter $\mathcal{A}$ from these eigenstates, and compare without any free parameters to our data at $V_{532} = 45$ kHz, $V_{1064} = 15$ kHz.

For the first few oscillations, we see fairly good agreement between experiment and theory. Eventually the zero crossing of the data lags the theory, and we see a substantial disagreement in the amplitude of oscillation. We calculate the sum-of-square errors (SSE) between theory and experiment and minimize the SSE to find the best fitting lattice depths V_{532}, V_{1064}. We find an optimal fit of $V_{532} = 29.5$ kHz,$V_{1064} = 14.2$ kHz for the left trimerization, and $V_{532} = 27.5$ kHz, $V_{1064} = 13.2$ kHz for the right. The dependence of the SSE on V_{532} is very weak, so the fitting of V_{532} is very unreliable. This is not the case for V_{1064} and we must conclude that there must be a lattice calibration error on the order of 10%.

Explanation of asymmetry

Whilst the band structure numerics demonstrate that we implement this trimer identification technique as intended, they offer little in the way of understanding. To explain the asymmetry in the momentum distribution, we examine the center of mass dynamics of the Wannier functions.

Consider the three sites A, B, C as drawn in figure 6.7, with the center of the 1064 nm potential equidistant from the three sites. The center of the potential is at $\boldsymbol{r}_{i,j} = i\boldsymbol{a}_1 + j\boldsymbol{a}_2 + (0,0)$, and the three sites are located

$$\boldsymbol{r}_{i,j,A} = i\boldsymbol{a}_1 + j\boldsymbol{a}_2 + a\left(\tfrac{1}{4\sqrt{3}}, -\tfrac{1}{4}\right) = i\boldsymbol{a}_1 + j\boldsymbol{a}_2 + \boldsymbol{r}_a \tag{6.8}$$

$$\boldsymbol{r}_{i,j,B} = i\boldsymbol{a}_1 + j\boldsymbol{a}_2 + a\left(-\tfrac{1}{2\sqrt{3}}, 0\right) = i\boldsymbol{a}_1 + j\boldsymbol{a}_2 + \boldsymbol{r}_b \tag{6.9}$$

$$\boldsymbol{r}_{i,j,C} = i\boldsymbol{a}_1 + j\boldsymbol{a}_2 + a\left(\tfrac{1}{4\sqrt{3}}, \tfrac{1}{4}\right) = i\boldsymbol{a}_1 + j\boldsymbol{a}_2 + \boldsymbol{r}_c \tag{6.10}$$

When the 532 lattice is switched off, the atoms at these sites are accelerated due to the approximately harmonic potential of the 1064 nm lattice. Denoting the harmonic oscillator frequency of the 1064 nm lattice as ω_{1064}, the accelerations of the three sites are:

$$\boldsymbol{a}_A = -\,\omega_{1064}^2 \boldsymbol{r}_a \tag{6.11}$$

$$\boldsymbol{a}_B = -\,\omega_{1064}^2 \boldsymbol{r}_b \tag{6.12}$$

$$\boldsymbol{a}_C = -\,\omega_{1064}^2 \boldsymbol{r}_c \tag{6.13}$$

If $w(\boldsymbol{r}-\boldsymbol{r}_{i,\gamma})$ is a wavepacket that satisfies the Schrödinger equation, then when it is accelerated it is transformed as [74]:

$$w(\boldsymbol{r}-\boldsymbol{r}_{i,\gamma}) \rightarrow e^{i\boldsymbol{k}_\gamma(\boldsymbol{t})\cdot\boldsymbol{r}} w(\boldsymbol{r}-\boldsymbol{r}_{i,\gamma}(t)) \tag{6.14}$$

where we have dropped terms beyond first order in time t, giving the momenta $\boldsymbol{k}_\gamma(t)$ and position $\boldsymbol{r}_{i,\gamma}(t)$:

$$\boldsymbol{k}_\gamma(t) = -t\tfrac{m}{\hbar}\omega^2\boldsymbol{r}_\gamma = -\kappa\boldsymbol{r}_\gamma \tag{6.15}$$

$$\boldsymbol{r}_{i,\gamma}(t) = \boldsymbol{r}_{i,\gamma} \tag{6.16}$$

With these transformed Wannier functions, we can calculate the weights $n_{\boldsymbol{G}_i}$ of the momentum distribution equation 6.5:

$$n_{\boldsymbol{G}_i} = |\sum_\gamma \tilde{w}(\boldsymbol{G}_i-\boldsymbol{k}_\gamma)e^{i(\boldsymbol{G}_i-\boldsymbol{k}_\gamma)\cdot\boldsymbol{r}_\gamma)}\psi_\gamma|^2). \tag{6.17}$$

Note that we have dropped the time dependence of $\boldsymbol{k}_\gamma(t)$ for greater clarity. As $\boldsymbol{k}_\gamma\cdot\boldsymbol{r}_\gamma \propto |\boldsymbol{a}|^2$, the phase $e^{-i\boldsymbol{k}_\gamma\cdot\boldsymbol{r}_\gamma}$ is common to all sites. Assuming the Wannier function is as symmetric Gaussian function of the form $\tilde{w}(\boldsymbol{k}) = e^{-\frac{\boldsymbol{k}^2}{2Q^2}}$, and $|\boldsymbol{k}| \ll |\boldsymbol{G}_i|$ then

$$\tilde{w}(\boldsymbol{G}_i-\boldsymbol{k}_\gamma) = e^{-\frac{(\boldsymbol{G}_i-\boldsymbol{k}_\gamma)^2}{2Q^2}} \approx e^{-\frac{\boldsymbol{G}_i^2}{2Q^2}} e^{\frac{\boldsymbol{G}_i\cdot\boldsymbol{k}_\gamma}{Q^2}} = \tilde{w}(\boldsymbol{G}_i)e^{\boldsymbol{G}_i\cdot\boldsymbol{k}_\gamma/Q^2} \tag{6.18}$$

Thus we have

$$n_{\boldsymbol{G}_i} = nw(\boldsymbol{k})|^2\,|\sum_\gamma e^{\boldsymbol{G}_i\cdot\boldsymbol{k}_\gamma/Q^2}e^{i(\boldsymbol{G}_1\cdot\boldsymbol{r}_\gamma)}|^2 \tag{6.19}$$

Calculating $n_{\boldsymbol{G}_i}$ for $\boldsymbol{G}_i = \pm\boldsymbol{G}_1$

$$n_{\boldsymbol{G}_1} = n\tilde{w}(\boldsymbol{G}_i)|e^{2\pi\kappa/3Q^2} + 2e^{-\kappa\pi/3Q^2}e^{i\pi}|^2$$
$$n_{-\boldsymbol{G}_1} = n\tilde{w}(\boldsymbol{G}_i)|e^{-2\pi\kappa/3Q^2} + 2e^{\kappa\pi/3Q^2}e^{-i\pi}|^2.$$

Assuming that κ/Q^2 is small allows us to expand these to first order, giving

$$n_{\boldsymbol{G}_1} = n\tilde{w}(\boldsymbol{G}_i)\left(1-\frac{8\pi\kappa}{3Q^2}\right) \tag{6.20}$$

$$n_{-\boldsymbol{G}_1} = n\tilde{w}(\boldsymbol{G}_i)|\left(1+\frac{8\pi\kappa}{3Q^2}\right). \tag{6.21}$$

Thus the asymmetry parameter scales as

$$\mathcal{A} = \frac{P_{\boldsymbol{G}_1}-P_{\boldsymbol{G}_{-1}}}{P_{\boldsymbol{G}_1}+P_{\boldsymbol{G}_{+1}}} = -\frac{8\pi\kappa}{3Q^2} \tag{6.22}$$

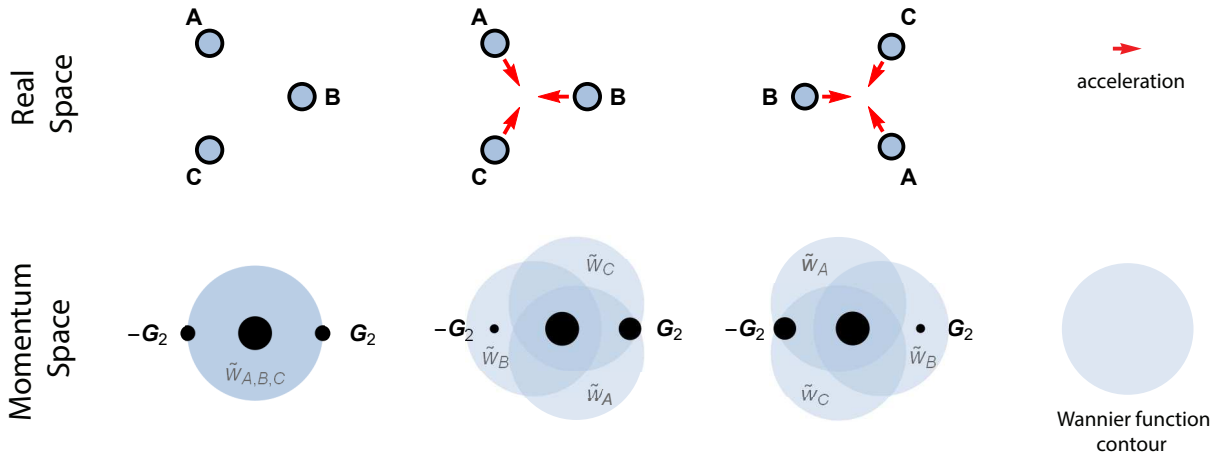

Figure 6.7: How the momentum space asymmetry is generated. (a) With no acceleration (red arrows), the Fourier transform of the Wannier functions $\tilde{w}_\alpha$from sites A,B and C lie onto of each other in momentum space. (b,c) The 1064 nm potential accelerates the Wannier functions in opposite ways for the two different trimerizations. This causes a displacement of the Wannier functions in momentum space, favoring interference at $\boldsymbol{G}_2$ or $-\boldsymbol{G}_2$.

Summarizing what the analytic calculation tells us, population at a reciprocal lattice vector comes a result of interference from the three sites A, B and C. At $\boldsymbol{G}_2$ AB and BC interference are out of phase with AC interference, leading to a partial cancellation. When the Wannier functions are accelerated by the 1064 nm lattice they are displaced from $\boldsymbol{k} = 0$, which biases their contribution to interference at $\boldsymbol{G}_2$ or at $-\boldsymbol{G}_2$. This changes the interference at the $\boldsymbol{G}_2$ in such a way that the population decreases if the Wannier function at site B is accelerated towards $\boldsymbol{G}_2$.

Linear sensitivity to lattice displacement

An important practical feature of our implementation of the trimerized kagome lattice is that the energies of the sites are linearly sensitive to the relative displacement $\boldsymbol{\delta}$ of the 532 nm lattice and 1064 nm lattice. This is notably unlike our implementation of the Kagome lattice, where the onsite energies are quadratically sensitive to $\boldsymbol{\delta}$.

In practice we always have finite displacement, so it is important to understand what level we can tolerate and still capture the essential physics. As we will show in the next chapter, the Bose-Hubbard physics of the trimerized kagome lattice is that of eigenstates of the trimers being weakly coupled together by J'. Thus we argue that if the local eigenstates remain sufficiently similar, the Bose-Hubbard physics remains similar.

We argue that if the relative energy shift ΔE_γ of the site γ is small compared to J for all sites, the eigenstate effectively remains the same. The tunneling J controls the hybridization of the three sites of the trimer, so if $\Delta E_\gamma \ll J$ the population, and coherence of the eigenstates

are virtually identical to the case $\Delta E_\gamma = 0$. We can even relax this restriction to $\Delta E < J_\gamma$, where we note that for eigenstates of a Hamiltonian with $U > J > \Delta E_\gamma$, the shift in the energies of the eigenstates from $\Delta E_\gamma = 0$ are relatively small. For displacements $\boldsymbol{\delta}$ along the x-axis (i.e. towards site B) from the symmetric trimerized kagome lattice position, the energy shift between sites B and sites A and C is

$$\Delta E = \Delta E_A - \Delta E_B = -4.2 V_{1064} \frac{|\boldsymbol{\delta}|}{a} \tag{6.23}$$

At $J/h = 250$ Hz, satisfying $\Delta E < J$ requires a displacement of less than 1 nm at $V_{1064} = 40$ kHz. See chapter 4 for more details.

Momentum distribution

Additionally, we calculate the effect on the momentum distribution of this displacement along the x-axis by δ. Let us assume that δ is sufficiently small that the unoccupied site D remains unoccupied. Thus the weights of the first order peaks of the momentum distribution are given by

$$n_{\boldsymbol{G}_1} = n_{-\boldsymbol{G}_1} = N|w(\boldsymbol{k})|^2|\psi_A + \psi_B - \psi_C|^2 \tag{6.24}$$
$$n_{\boldsymbol{G}_2} = n_{-\boldsymbol{G}_2} = N|w(\boldsymbol{k})|^2|\psi_A - \psi_B + \psi_C|^2 \tag{6.25}$$
$$n_{\boldsymbol{G}_3} = n_{-\boldsymbol{G}_3} = N|w(\boldsymbol{k})|^2|-\psi_A + \psi_B + \psi_C|^2, \tag{6.26}$$

where ψ_A, ψ_B and ψ_C are the amplitudes of the wavefunction at sites A, B and C. Under the displacement δ, these wavefunction amplitudes are modified from $\psi_A = \psi_B = \psi_C = \sqrt{\frac{\mu}{g}}$ to

$$\psi_A = \sqrt{\frac{\mu + \Delta E/3}{g}} \tag{6.27}$$
$$\psi_B = \sqrt{\frac{\mu - 2\Delta E/3}{g}} \tag{6.28}$$
$$\psi_C = \sqrt{\frac{\mu + \Delta E/3}{g}}. \tag{6.29}$$

We define the relative population in the momentum peak $\boldsymbol{G}_i$ and $-\boldsymbol{G}_i$ as

$$P_i = \frac{n_{\boldsymbol{G}_i} + n_{\boldsymbol{G}_i}}{n_{\boldsymbol{G}_1} + n_{\boldsymbol{G}_{-1}} + n_{\boldsymbol{G}_2} + n_{\boldsymbol{G}_{-2}} + n_{\boldsymbol{G}_3} + n_{\boldsymbol{G}_{-3}}}. \tag{6.30}$$

With no displacement $P_1 = P_2 = P_3$. As fluctuations of the displacement happen in both x and y experimentally, we compare to theory by calculating the RMS deviation from 1/3 of these relative populations:

$$\Delta P = \sqrt{\left(P_1 - \frac{1}{3}\right)^2 + \left(P_2 - \frac{1}{3}\right)^2 + \left(P_3 - \frac{1}{3}\right)^2}. \tag{6.31}$$

Combining equations and expanding to first order in $|\delta|$ we find

$$\Delta P = \frac{2}{3}\sqrt{\frac{2}{3}}\frac{\Delta}{\mu} = \frac{8.4}{3}\sqrt{\frac{2}{3}}\frac{V_{1064}}{\mu}\frac{\delta}{a}. \tag{6.32}$$

Inverting this equation gives us the RMS value of δ:

$$\delta_{RMS} = \frac{3}{8.4}\sqrt{\frac{3}{2}}\Delta P\frac{\mu}{V_{1064}}a. \tag{6.33}$$

6.4 Bose-Hubbard physics

Having verified that we have faithfully implemented the trimerized Kagome lattice potential, we now introduce the physics of the Bose-Hubbard lattice derived from this potential. Throughout this chapter we will follow the theoretical approach that inspired the trimerized kagome lattice: solve the strongly coupled problem on each trimer before introducing weak coupling between trimers.

Single trimer

We begin with studying the three site Bose-Hubbard model

$$H = -J\sum_{\langle i,j\rangle} b_i^\dagger b_j + \frac{U}{2}\sum_i n_i(n_i - 1). \tag{6.34}$$

One particle

In the $\nu = 1$ sector, the ground state is one atom completely delocalized over the three sites with equal phases

$$\left|\psi_1^0\right\rangle = \frac{1}{\sqrt{3}}\left(|001\rangle + |010\rangle + |100\rangle\right) \tag{6.35}$$

$$E_1^0 = -2J - \mu \tag{6.36}$$

The two excited states $|\psi_1^1\rangle$ and $|\psi_1^2\rangle$ correspond to rotation clockwise and counterclockwise

$$\left|\psi_1^1\right\rangle = \frac{1}{\sqrt{3}}\left(|100\rangle + e^{i2\pi/3}|010\rangle + e^{i4\pi/3}|001\rangle\right) \tag{6.37}$$

$$= \frac{1}{\sqrt{3}}\left(|100\rangle + e^{-i2\pi/3}|010\rangle + e^{-i4\pi/3}|001\rangle\right), \tag{6.38}$$

both with energy

$$E_1^{1,2} = J - \mu \tag{6.39}$$

We follow [14] and note these are eigenstates $(0, +1, -1)$ of a chirality operator

$$\chi = B_+^\dagger B_+ - B_-^\dagger B_- \tag{6.40}$$

where $B_\pm = (b_1 + e^{\pm i2\pi/3}b_2 + e^{\pm i4\pi/3}b_3)$.

Two particles

H commutes with the chirality operator, and it can be shown [14] that the ground state has chirality zero. Thus in the $n = 2$ manifold the ground state $|\psi_2^0\rangle$ is a combination of the zero chirality two particle states $|W_2^2\rangle$,$|W_2^1\rangle$

$$\left|\psi_2^0\right\rangle = \sin(\phi)\left|W_2^1\right\rangle + \cos(\phi)\left|W_2^2\right\rangle \tag{6.41}$$

$$\left|W_2^1\right\rangle = \tfrac{1}{\sqrt{3}}\left(|110\rangle + |101\rangle + |011\rangle\right) \tag{6.42}$$

$$\left|W_2^1\right\rangle = \tfrac{1}{\sqrt{3}}\left(|200\rangle + |020\rangle + |002\rangle\right) \tag{6.43}$$

where the ground state energy E_2^0 and ϕ are

$$E_2^0 = \frac{1}{2}\left(U - \sqrt{(U+2J)^2 + 32J^2}\right) - J - 2\mu \tag{6.44}$$

$$\tan\phi = \frac{1}{4\sqrt{2}J}\left((U+2J) + \sqrt{(U+2J)^2 + 32J^2}\right). \tag{6.45}$$

In the limit U/J is small, the $|\psi_2^0\rangle$ is simply a product of two of the $\nu = 1$ ground states, with wavefunction and energy,

$$\left|\psi_2^0\right\rangle = \sqrt{\tfrac{2}{3}}\left|W_2^1\right\rangle + \sqrt{\tfrac{1}{3}}\left|W_2^2\right\rangle \tag{6.46}$$

$$E_2^0 = -4J + U/3 - 2\mu. \tag{6.47}$$

When J/U is small no site is doubly occupied, and the state can be seen as a completely delocalized hole, with wavefunction and energy,

$$\left|\psi_2^0\right\rangle = \left|W_2^1\right\rangle \tag{6.48}$$

$$E_2^0 = -2J - 2\mu. \tag{6.49}$$

Fractional Mott insulating states

To study the Mott insulating states of the trimerized Kagome lattice we will first describe the states in the $J' = 0$ limit, argue why these states are still groundstates at small J', then demonstrate the evidence from mean-field theory.

The fractional Mott insulating states are simply products of the ground states we derived above for the trimers. For example, the $\nu = 1$ atom per plaquette state is simply

$$|\Psi\rangle = \prod_{plaq} |\psi_1^0\rangle \tag{6.50}$$

We can understand why this remains the ground state by looking at the excitation spectrum. There are now 5 lowest lying excitations of this state: a single excitation to $+1$ and -1 chirality states $|\psi_1^1\rangle$ and $|\psi_1^2\rangle$, a particle excitation $|\psi_2^0\rangle$, a hole excitation $|\psi_0^0\rangle$ and a simultaneous particle-hole excitation $|\psi_2^0\rangle$ and $|\psi_0^0\rangle$.

The weak hopping Hamiltonian $H_{Hop} = -J' \sum_{i,j} b_i^\dagger b_j$ only couples the ground state to the particle-hole excitation, and so to roughly argue for the existence of this Mott insulating state, we compare J' to the energy cost of the particle-hole excitation. The cost of a particle hole excitation is

$$E_2^0 + 0 - 2E_1^0 = 3J + \tfrac{U}{2} - \tfrac{1}{2}\sqrt{36J^2 + 4JU + U^2} \tag{6.51}$$

This energy cost is best understood in the limit J/U is large, where $\Delta E = U/3$. The atoms are completely delocalized over the three sites, adding another particle doesn't change that. However, there is still an energy cost $U/3$, which is less than U because the atoms are spread over 3 sites. When this $U/3 \gg J'$, these particle-hole excitations are strongly suppressed and the gas doesn't develop long range coherence. An interesting fact is that this argument holds true not just at $J \gg U$, but even at J slightly smaller than U. At $J = 0.2U$, the particle-hole energy gap is 60% of its value at $J \gg U$. From this argument we can make a qualitative prediction: the fractional Mott insulating states are more stable when J is larger, where this effective interaction is larger.

It should be noted that these fractional average filling Mott insulator states have none of the fractionalized excitations of the fractional quantum hall effect.

Mean field theory

The phase diagram for the Bose-Hubbard model on the trimerized kagome lattice has been studied via two methods: mean-field theory [14] and a cluster strong coupling expansion approach [9]. The mean-field calculation was rederived by Dr. Masayuki Okano, the results of which are plotted in figure 6.9.

The phase diagram calculated by Dr. Okano and the theoretical treatment in the literature agree with the basic intuition developed by considering particle-hole excitations in the previous sections. Both the mean-field and strong coupling methods predict the existence of stable insulating ground states, with $\nu = 1, 2, 3, ...$ atoms per trimer.

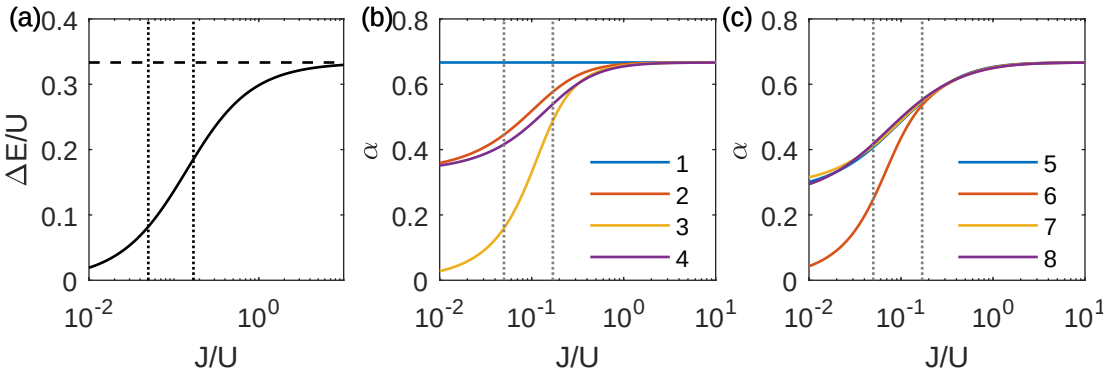

Figure 6.8: Energies and coherence of single trimers. (a) Particle-hole excitation energy for $\nu = 1$ filling. Dashed line is the $\Delta E = U/3$ limit for $J/U \to \infty$. Dotted vertical lines are $J/U = 0.05, 0.17$, where we take data later in the chapter. (b) Nearest-neighbor coherence α for isolated trimers of particle number ν. Dotted vertical lines are $J/U = 0.05, 0.17$. Note that particle number 4,5,7 and 8 all behave approximately like $\nu = 2$.

As J/U increases, so does the maximum J'/U of the $\nu = 1$ and 2 phase boundaries. The increased delocalization gives a larger particle-hole energy gap, and the Mott state is stabilized to larger values of J'.

For $J'/U = 0.17$, the experimental values required to access the $\nu = 1$, 2 and 3 states are well within reach. The $\nu = 1$, 2 states are accessible over a significant range of chemical potential, so are likely to be occupied in an inhomogeneous potential. Furthermore, creating a trimerized kagome lattice with $J'/U < 0.015$ for $J/U = 0.17$ is well within our capacity as can be seen in section 6.2.

Nearest-neighbor coherence

Even at $J' = 0$, there is a non-zero next-neighbor coherence of the fractional Mott insulating states due to the delocalization of the atoms inside the trimers. Calculating this coherence simply reduces to evaluating the coherence of the single trimers. Using the definition for α in the trimerized kagome lattice (equation 5.9), we calculate the nearest-neighbor coherence at $J' = 0$ for varying values of U/J, and plot them in figure 6.8(b,c)

We note an interesting behavior of the single trimer coherences. All ν that are multiples of 3 have the approximately the same coherence as $\nu = 3$, and all others after $\nu = 3$ have the approximately the same coherence as $\nu = 2$. We can understand this in the U/J large limit. When ν is a multiple of three the ground state is simply

$$\left|\psi_\nu^0\right\rangle = \left|\tfrac{\nu}{3}, \tfrac{\nu}{3}, \tfrac{\nu}{3}\right\rangle, \tag{6.52}$$

which has no coherence. When ν is not a multiple of three, there is either an extra delocalized particle, or an extra delocalized hole, which gives the substantial coherence even at $U/J \gg 1$.

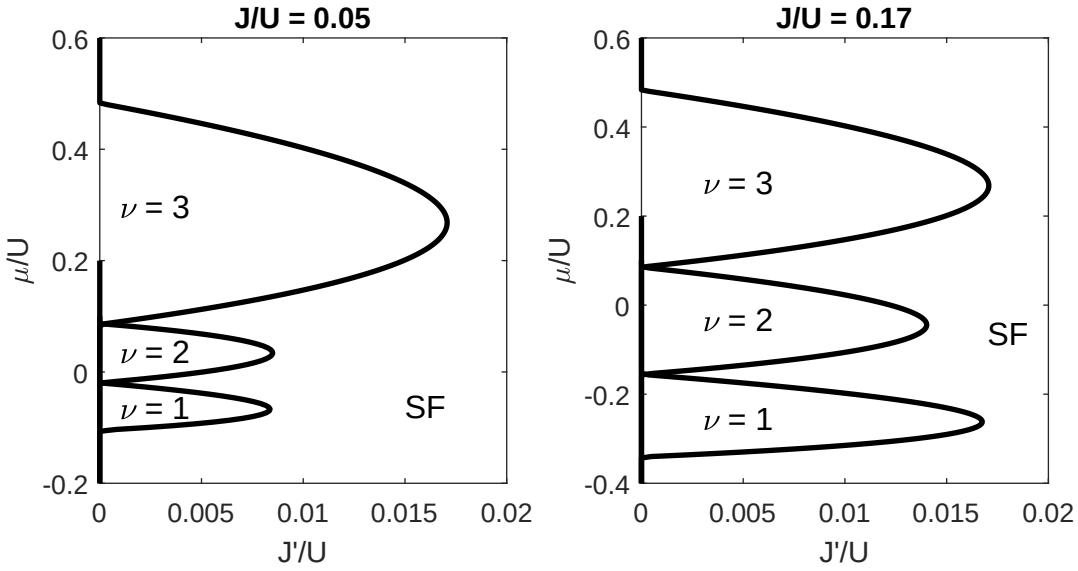

Figure 6.9: Phase diagram of the Bose-Hubbard model in a trimerized kagome lattice. The phase boundaries for Mott insulating states with $\nu = 1 - 3$ atoms per trimer are shown for $J/U = 0.05$ and $J/U = 0.17$. SF denotes the superfluid phase.

6.5 Nearest-neighbor coherence experiments

In this section we describe measurements of the nearest-neighbor coherence in a trimerized kagome lattice that demonstrates one of the unique features of this lattice: even when long range coherence has disappeared, nearest-neighbor coherence remains. This is one piece of evidence for the fractional Mott insulating states.

Experimental procedure

We begin by preparing the gas in an identical manner to the triangular lattice experiments in section 5.6, that is a Bose-Einstein condensate loaded into a 50 kHz deep vertical lattice with all other potentials turned off. The lattice is loaded by simultaneously ramping the 532 nm and 1064 nm lattices in exponential ramps. We continue to apply a compensating curvature to keep the Thomas-Fermi radius constant, but we take into account the curvature of the 1064 lattice, and the structure of the trimerized Kagome lattice. These ramps are sufficiently slow as to be adiabatic with respect to the band gap, interaction energies, and both tunneling timescales. The gas is held for 40 ms, after which all potentials are turned off and the gas expands for 16 ms time-of-flight before absorption imaging is performed.

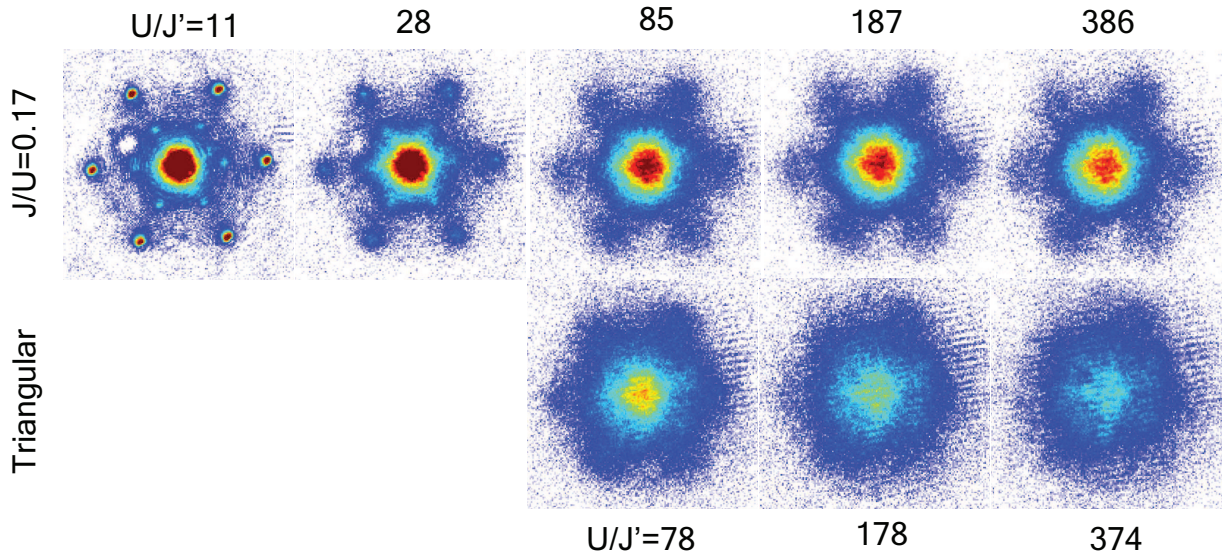

Figure 6.10: Momentum distribution of gases released from triangular or trimerized kagome lattices. As U/J' is increased at constant J/U, sharp diffraction peaks are lost for the TKL. However, a broad modulation pattern persists as U/J' is further increased. Whilst modulation can be seen in the triangular lattice at $U/J = 78$, it disappears as U/J' is further increased.

Data and analysis

In figure 6.10 we present the time-of-flight images obtained at constant $J/U = 0.17$ and varying U/J'. In the first few figures we can clearly see sharp diffraction peaks corresponding to the long range coherence of the superfluid fraction. As U/J' increases, these peaks diminish in amplitude and eventually disappear. Broad structure remains in the diffraction patterns corresponding to nearest neighbor coherence. In contrast to the triangular lattice in the previous chapter, it does not disappear at U/J' is increased.

We fit the images with the same functional form as the triangular lattice, equation 5.6, neglecting the ellipticity of the Wannier functions (discussed in the next section), and extract the nearest-neighbor coherence α for two constant values of $U/J = 0.17, 0.05$. The fitting procedure is as performed in section 5.3, with the exception that the size of the Wannier functions is fixed for each U/J data set. Each data point in figure 6.11 is the average of 3 to 9 individual measurements.

For both values of U/J' we see an initial decrease in α, which follows an approximate $(U/J)^{-1}$ form. After $U/J' = 100$ the value of α in the trimerized kagome lattices sharply diverges from that of the triangular lattice, which continues to fall as $(U/J)^{-1}$. The trimerized kagome lattice data never precisely plateaus at large values of U/J', but $\log \alpha$ does show a weak dependence on $\log(U/J')$. For virtually all of the points shown, the coherence of $J/U = 0.17$ is larger than $J/U = 0.05$.

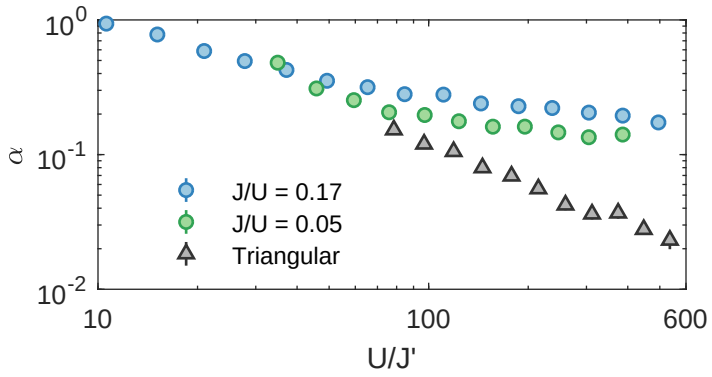

Figure 6.11: Nearest-neighbor coherence α of atoms in triangular and trimerized kagome optical lattices.

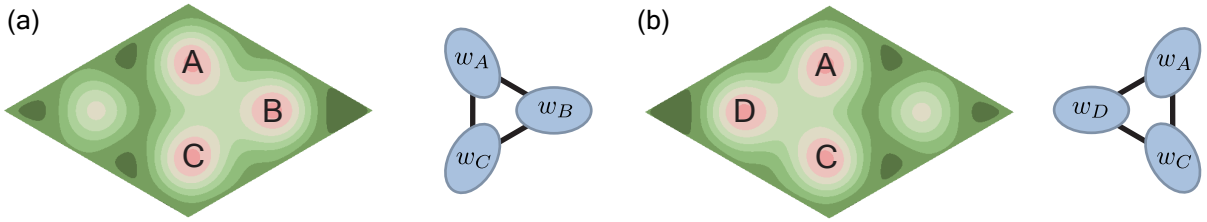

Figure 6.12: (a) Potential of the unit cell of the right trimerized kagome lattice and the corresponding elliptical Wannier functions. The ellipticity of the Wannier functions at sites A, B and C is shown by an exaggerated contour of the respective Wannier functions $w_A(\boldsymbol{r})$, $w_B(\boldsymbol{r})$ and $w_C(\boldsymbol{r})$. (b) Potential of unit cell of the left trimerized kagome lattice and the corresponding elliptical Wannier functions.

Ellipticity of the Wannier functions

As can be seen in figure 6.12 the potential wells of sites A, B and C are not symmetric. Each is slightly elliptical along a different axis, so in general it follows that the Wannier functions are not rotationally symmetric, nor identical as can be seen in figure 6.12. We calculate the ratio of the eigenvalues of the Hessian matrix η, evaluated at the minima of the trimerized Kagome lattice potential, and find a maximum ratio $\eta = 1.16$ in the data presented in section 6.5. We then fit the momentum distributions with the functional form equation 5.9, with the Wannier functions as elliptical Gaussians with the ellipticity derived from the ratio of curvatures η. We find that this has a 3% effect on the value of α at the maximum ellipticity. The effect on the entire data set is thus substantially smaller than the error in the mean. Due to the lower stability of these fits, we neglect this effect.

6.6 Phase imprinting

In the previous section, we showed that the nearest-neighbor coherence in the TKL only weakly depends on U/J' at large values of U/J'. As expected in the ground state, the nearest neighbor coherence was completely real, and told us the sum of contributions from the weak and strong bonds. As U/J' increases, we expect the coherence to mostly come from the strong bond J. In this section we demonstrate a method to show the asymmetry of the bonds.

Momentum distribution

To explain how we can generate a signal in the momentum distribution showing the difference in coherence of the bond, consider the 1D hopping model. Hopping one step to the right contributes factors e^{ika}, whereas hopping to the left contributes e^{-ika}. When the wavefunction is real the left and right hopping terms across any bond have equal prefactors, and as such the overall momentum distribution is symmetric.

Introducing at phase at site 1 breaks this equality. Hopping that begins at site 1 picks up a phase ϕ, whereas hopping that ends at 1 picks up $-\phi$, If the original strength of the coherence was the same, then the prefactor for hopping right from 0 to 1 is the same for hopping from 2 to 1, and as such the momentum distribution is symmetry. However, if those coherences are not the same, the momentum distribution is not symmetric. Thus we can relate asymmetry in the momentum distribution to the difference in coherences .

Consider the general form of the momentum distribution on the kagome lattice derived in chapter 5:

$$\begin{aligned} n(\boldsymbol{k}) = N|\tilde{w}(\boldsymbol{k})|^2(1 + \alpha_1(\cos(\boldsymbol{k}\cdot\boldsymbol{a}_1) + \alpha_2\cos(\boldsymbol{k}\cdot\boldsymbol{a}_2) + \alpha_3\cos(\boldsymbol{k}\cdot\boldsymbol{a}_3)) \\ + \beta_1\sin(\boldsymbol{k}\cdot\boldsymbol{a}_1) + \beta_2\sin(\boldsymbol{k}\cdot\boldsymbol{a}_2) + \beta_3\sin(\boldsymbol{k}\cdot\boldsymbol{a}_3)) \end{aligned} \tag{6.53}$$

Adding a phase ϕ on site C and looking at the real and imaginary part of the nearest-neighbor coherence α_1 and β_1 :

$$\begin{aligned} \alpha_1 &= \tfrac{2}{v_0} Re(e^{-i\phi}\langle b^\dagger_{0,0,a} b_{0,0,c}\rangle + e^{i\phi}\langle b^\dagger_{0,0,c} b_{1,0,a}\rangle \\ &= \tfrac{2}{v_0}\cos(\phi)\left[\langle b^\dagger_{0,0,a} b_{0,0,c}\rangle + \langle b^\dagger_{0,0,c} b_{1,0,a}\rangle\right] \qquad (6.54) \\ \beta_1 &= -\tfrac{2}{v_0} Im(e^{-i\phi}\langle b^\dagger_{0,0,a} b_{0,0,c}\rangle + e^{i\phi}\langle b^\dagger_{0,0,c} b_{1,0,a}\rangle \\ &= -\tfrac{2}{v_0}\sin(\phi)\left[\langle b^\dagger_{0,0,a} b_{0,0,c}\rangle - \langle b^\dagger_{0,0,c} b_{1,0,a}\rangle\right] \qquad (6.55) \end{aligned}$$

we see that α_1 and β_1 oscillate with the applied phase ϕ. Applying a $\phi = \pi/2$ phase shift should make the distribution along $\boldsymbol{a}_1$ a sine not cosine, with an amplitude proportional to the difference in bond strengths. α_3 and β_3 should also similarly oscillate with ϕ and α_2 and β_2 should remain untouched.

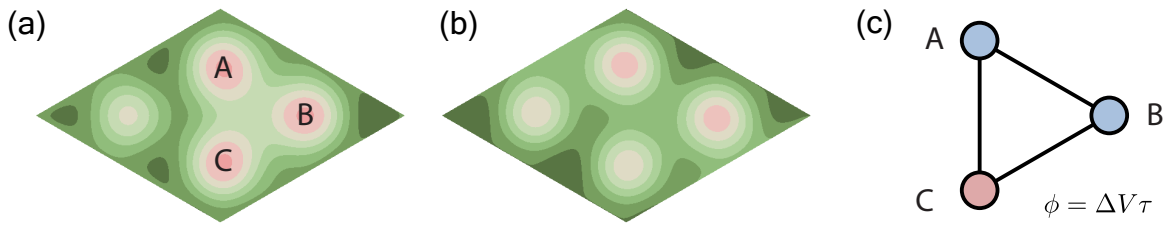

Figure 6.13: The change in potential in the phase imprint technique. (a) The unit cell of the trimerized kagome lattice, with sites A, B and C. (b) The same unit cell in the phase imprint potential. Sites A and B are at equal energy, but site C is displaced by ΔV. (c). The idealized implementation of this process as phase evolution.

Imprinting a phase

We implement a phase shift ϕ in a relatively simple way, by simply turning off one of the 1064 beams for a period of time τ. In the original potential all three minima are at the same energy, and as such the the resultant Bose-Hubbard model derived from this potential has no offset. In the 'Phase Imprint' potential $V_{PI\pm}(\boldsymbol{r})$, one of the minima is shifted $\Delta V \approx 0.2 V_{1064}$ higher than the other two, as can be seen in figure 6.13. We solve the band structure of this new potential exactly, and compare it to a tight binding model to extract the correct value of the energy shift $\Delta V = 0.20 V_{1064}$.

$$\begin{aligned} V_{PI\pm} = &\tfrac{2}{9} V_{532} \left(3 - \cos(2\boldsymbol{G}_1 \cdot \boldsymbol{r}) - \cos(2\boldsymbol{G}_2 \cdot \boldsymbol{r}) - \cos(2\boldsymbol{G}_3 \cdot \boldsymbol{r})\right) \\ &- \tfrac{1}{9} V_{1064} \left(2 + 2\cos(\boldsymbol{G}_1 \cdot (\boldsymbol{r} \pm \boldsymbol{\delta})\right) \end{aligned} \tag{6.56}$$

We prepare the gas in a identical manner to section 6.5 with constant $J/U = 0.15$, for three different values of U/J'. We then turn off beam 1 for a time τ, before turning off all potentials and performing time of flight and absorption imaging.

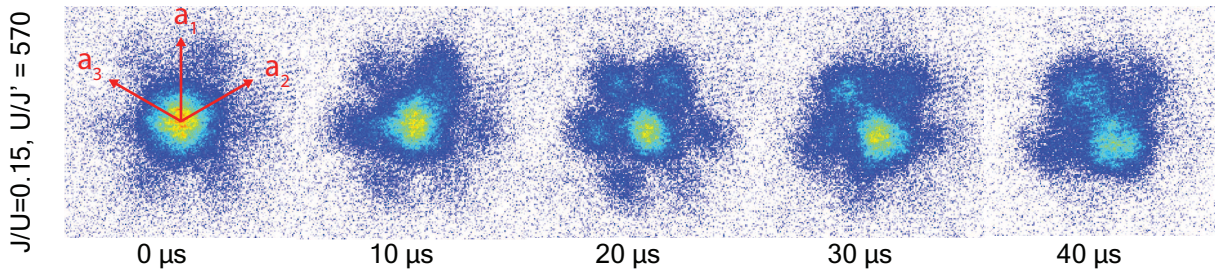

Figure 6.14: Evolution of the momentum distribution in the phase imprint potential. The gas is initially symmetric along $\boldsymbol{a}_1, \boldsymbol{a}_2$ and $\boldsymbol{a}_3$, but evolves into a gas with asymmetry along $\boldsymbol{a}_1$ and $\boldsymbol{a}_3$. It remains symmetric along $\boldsymbol{a}_2$.

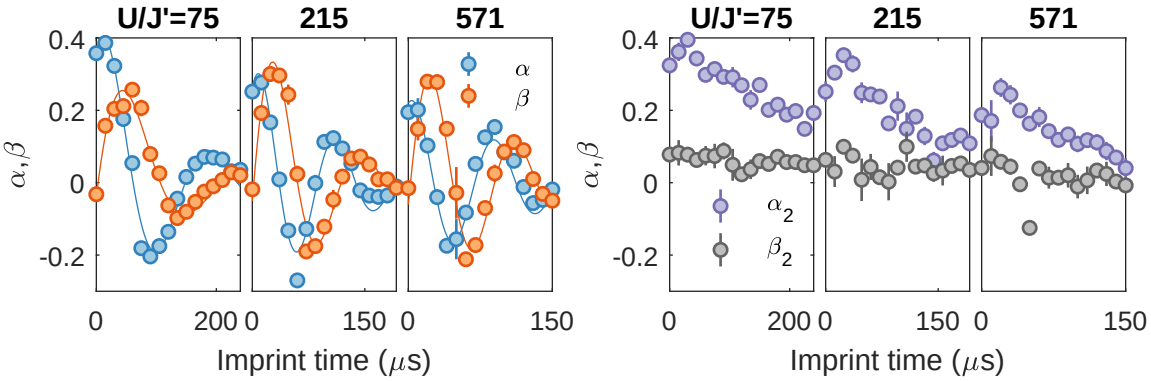

Figure 6.15: Final data for the phase imprint experiment. (a) Averaged values of α and β along directions $\boldsymbol{a}_1$ and $\boldsymbol{a}_3$. The coherence along these two directions rapidly oscillated due to the added potential on site C. (b) α and β along $\boldsymbol{a}_2$. No oscillation is observed along this direction as it does not involve site C. A slow decay of α_2 is however observed.

We display the momentum distributions obtained for $U/J' = 570$ in figure 6.14 for $\tau = 0 - 150\,\mu s$. The momentum distribution at $\tau = 0$ is initially symmetric along all three axis $\boldsymbol{a}_1, \boldsymbol{a}_2$ and $\boldsymbol{a}_3$. However, even at $t = 10\,\mu s$ we see that the gas develops asymmetry along $\boldsymbol{a}_1$ and $\boldsymbol{a}_3$ but remains symmetric across $\boldsymbol{a}_2$. For further imprint times we see the symmetry along these axes oscillate between symmetric and asymmetric.

We fit the gas with the functional form equation of 6.53 and extract the coefficients α_i and β_i, which are plotted in figure 6.15. We discuss our choice of Wannier function below. Data points are the averages of 2-3 measurements, and we reject points with large asymmetry along the $\boldsymbol{a}_2$ axis.

At each experimental U/J' value we see α_1 and α_3 oscillate, consistent with us applying a potential on site C. We also see a non-zero oscillation of β_1 and β_3, telling us there is a detectable difference in coherence between strong and weak bonds for all three values of U/J'. For $U/J' = 215, 570$ we conclude the coherence mostly comes from a single bond, as the maximum values of the α and β oscillations are similar. At $U/J' = 500$ we expect to see the weak bond contribute little to the coherence, and our data is consistent with this. For $U/J = 75$ the amplitudes of the α and β oscillations are not similar, and so the contribution from the weak bond is not negligible.

Whilst we can draw these qualitative conclusions, much of our data lie outside the model of simply imprinting a phase. The oscillations appear to decay, as does the value of α_2, which isn't consistent with simply having applied a phase shift to the C site. We also note that for $U/J' = 570$ the value of β rises above the value of α. That has no explanation in this model of phase imprinting. We will try to explain these deviations in the next section of this chapter.

We fit the evolution of α and β with an exponentially decaying sinusoids with a free choice of phase. The frequencies extracted from these fits are shown in table 6.1. In the

U/J'	Frequency from exp. decay fit α	Frequency from exp. decay fit β	$\Delta V/h$
75	5.7 ± 0.3 kHz	4.8 ± 0.3 kHz	6.0 kHz
215	9.7 ± 0.5 kHz	8.5 ± 0.4 kHz	9.2 kHz
571	11.7 ± 0.7 kHz	11.4 ± 0.4 kHz	12.4 kHz

Table 6.1: Results of fitting the data in figure 6.15 with the functional form $\alpha = Ae^{-\gamma t}\cos(2\pi f t + \phi)$. These frequencies are compared to the expected evolution frequency $\Delta V/h$.

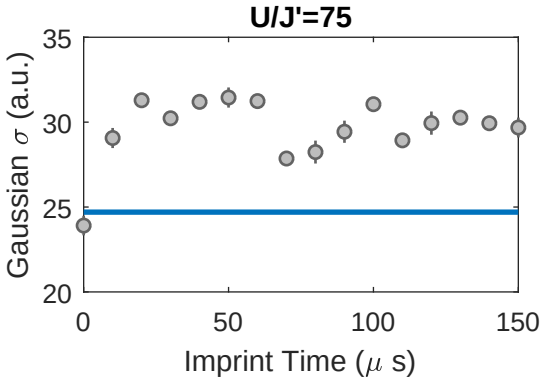

Figure 6.16: Change in the extracted Gaussian width during phase imprint for $J/U = 0.15$, $U/J' = 75$. At $\tau = 0$ μs, the extracted width is consistent with that of the blue $U/J = 0.17$ data from the previous section. After the potential is deformed, the width briefly oscillates before settling into its new equilibrium. These oscillations represent motion of the atoms within a well of the lattice, violating the ground band assumption

model of phase imprinting we expect that α and beta evolve at the same frequency given by $\Delta V/h$.

In these data, we fit the gas with a symmetric Gaussian function, but leave the width as a free parameter. We observe a damped oscillation of this Gaussian width, plotted in figure 6.16, during the phase imprint process on similar timescales to the phase evolution. We believe this is motion of the atoms within their lattice wells, and such is a violation of the ground band assumption of the Bose-Hubbard model.

Explaining the data

This 'phase imprinting' experiment produced a number of details inconsistent with simply imprinting a phase on one site. The oscillations of α and β decay quickly in time and are not described by the same frequency when fitted with an exponentially decaying sinusoid.

Furthermore, at relatively short times the maximum value of β becomes larger than the maximum value of α. This implies that the difference between the two coherences is larger

than their sum, a nonsensical result assuming the coherence is real and positive in the ground state.

We might expect some deviation from the phase imprint picture because of how it is implemented. We sharply turn off a single lattice beam and thus change the potential by a depth comparable to the ground to excited band energy spacing. We thus might expect that upper band dynamics play a role. We also implement the phase rotation in finite time, so extra evolution due to interactions and tunneling may play a role.

We explore these effects by performing some simple calculations that individually do not explain all of the behavior we see, but do allow us to isolate the causes of the various effects. We first study the role of interactions by considering evolution in a three site Bose-Hubbard model. We are thus able to conclude that much of the decay we see in figure 6.15 is due to evolution at two different eigenfrequencies with different interaction energies.

We then explore higher band effects by approximating the momentum distribution of a Mott insulator as a short coherence length thermal gas, and evolving this momentum distribution in the exact phase imprint potential. We do not see an explanation for the short time behavior of beta, or the discrepancy in evolution frequencies.

Bose-Hubbard model

The first theoretical comparison we make is to a three site, ν particle Bose-Hubbard Hamiltonian. We find the ground state of the initial Hamiltonian

$$H_I = -J \sum_{<i,j>} b_i^\dagger b_j + U/2 \sum_{i=1}^{3} n_i(n_i - 1), \tag{6.57}$$

before projecting this state into the eigenbasis of

$$H_{PI} = H_I + \Delta V n_1. \tag{6.58}$$

The eigenstates evolve at their eigenenergies, and then we construct the coherences

$$\alpha_1 = \frac{2}{v}\mathrm{Re}(b_a^\dagger b_c),\ \ \beta = \frac{2}{v}\mathrm{Re}(b_a^\dagger b_c). \tag{6.59}$$

In this model we neglect tunneling between plaquettes, and assume the plaquette is in an eigenstate of particle number. We believe this is a reasonable description of our system at short times relative to $1/J'$ because the energies of this local Hamiltonian $\Delta V, U, J \gg J'$, and our expectation is that the system is in a Mott insulating state.

We find good agreement between the observed coherence oscillations and those predicted by the local Bose-Hubbard model, if we scale the y-axis of the theory by 2/3. We expect to have a lower overall coherence because our system is at finite temperature, and naively scaling the y-axis is a proxy for this. What is clear from these simulations is that we are not seeing a dephasing, but just the beating of two different frequencies.

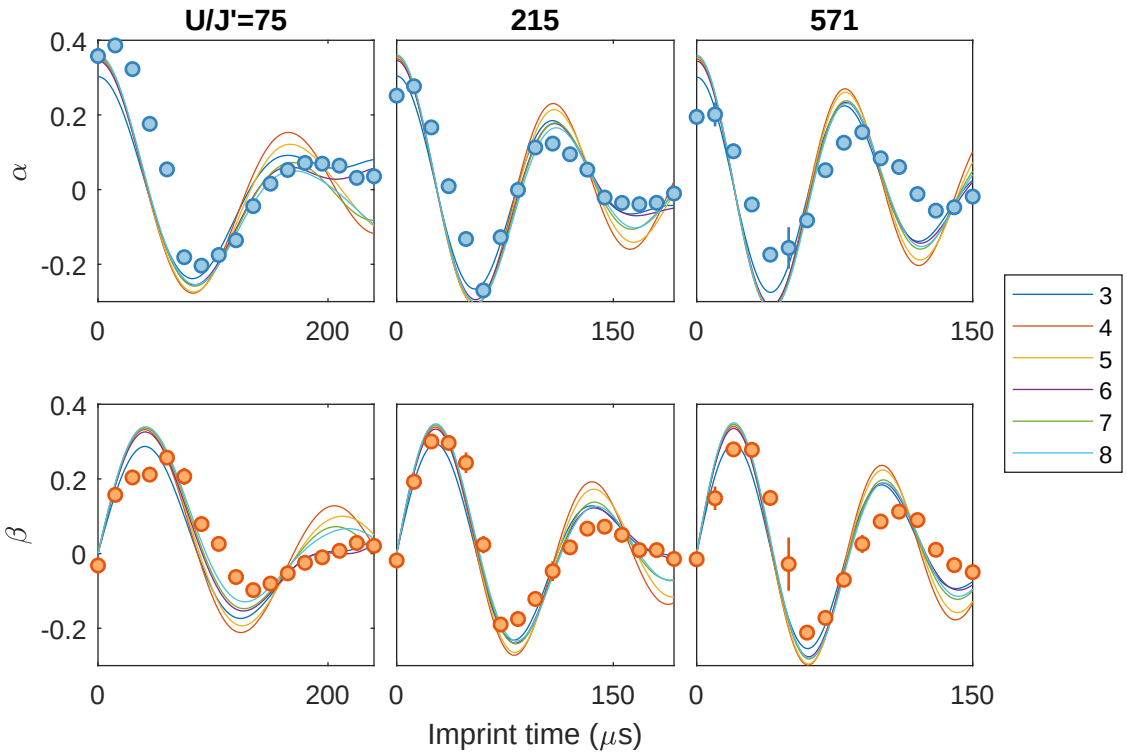

Figure 6.17: Comparison of the phase imprint data to an exact solution of the three site Bose-Hubbard model. The multiple theory lines correspond to different particle number ν per trimer. The overall consistency between theory and experiment shows the observed decay is largely, but not entirely, due to beating of states with different interaction energy.

For $U/J' = 570$ the ground state of the initial Hamiltonian is mostly projected into three eigenstates of the final Hamiltonian, shown in figure 6.18. The most occupied of these states has equal density in the three sites, but the other two states are mostly in BC, or mostly in A. Whilst we expected an energy splitting of ΔV, the different interaction energies of these states also give us splittings $\Delta V + O(U)$.

We would expect here our major beat frequencies at 11.0 kHz and 13.8 kHz. These numbers are higher than our two frequency fits, but overall provide a consistent description of our system up to a small miscalibration. We do not see any explanation for the short term where $\beta > \alpha$, and see a substantial disagreement with the observed decay of α_2, as shown in figure 6.19.

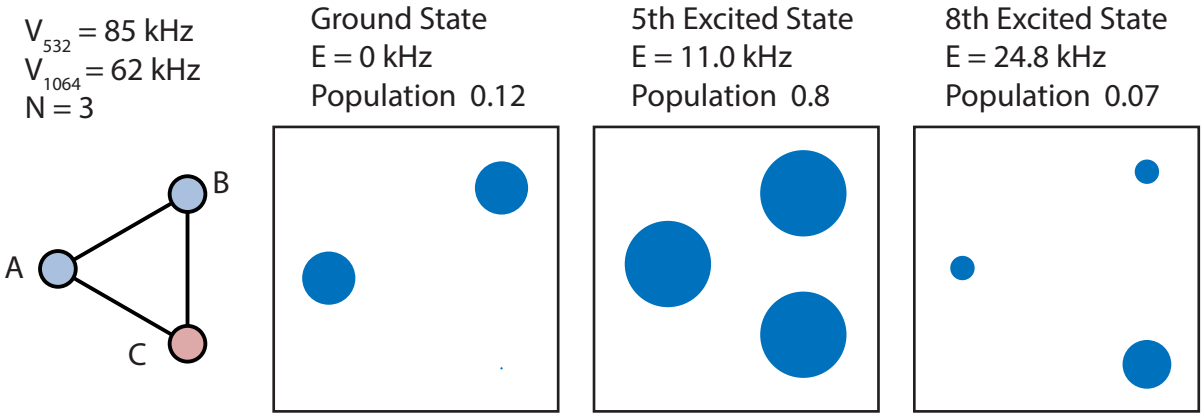

Figure 6.18: Densities of the eigenstates responsible for the beating in figure 6.15. The ground band of the trimerized kagome lattice at $V_{532} = 85$ kHz, $V_{1064} = 62$ kHz mostly projects into three eigenstates of the new potential. Most population is in an equal density excited state, but a significant population exists in the ground state and the eighth excited state, all of which have different interaction energies. Interference occurs between the ground and 5th excited state at 11.0 kHz, and between the fifth and eight excited states at 13.8 kHz.

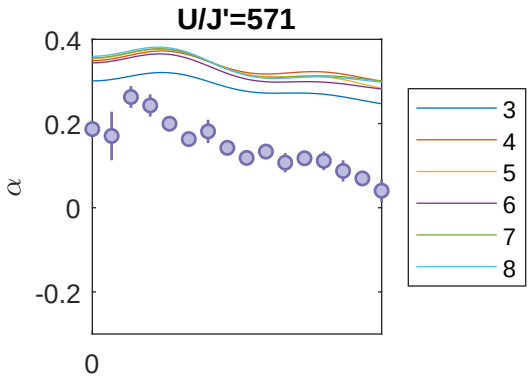

Figure 6.19: A comparison of α_2 between the phase imprint data and Bose-Hubbard theory. The theory doesn't account for the slow decay of α_2.

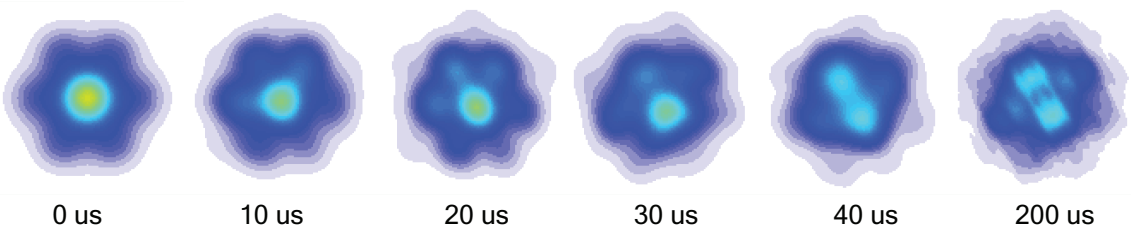

Figure 6.20: Thermal band structure simulation of the momentum distribution in figure 6.14. The momentum distribution is calculated for $V_{532} = 85$ kHz, $V_{1064} = 62$ kHz, corresponding to $J/U = 0.15$, $U/J' = 570$, with $k_B T = 0.5\ E_r$.

Finite temperature band structure

Whilst the Bose-Hubbard simulations explain the observed 'decay' of the oscillation signal, they don't explain the short time dynamics where $\max(\beta) > \max(\alpha)$. Instead we look to a non-interacting band structure model that takes into account higher band physics. We expect to have some coupling to higher bands, as we simultaneously introduce an energy offset ΔV, which is a significant fraction of the $S - P$ band gap, and shift the minima of the potentials. That we see oscillations of the fitted Wannier function widths shows that we are in fact breaking the ground band approximation.

To examine the effect of higher band dynamics, we solve a non-interacting band structure model following a similar method to section 6.3. Whilst we know interaction effects are important on the timescales we have data, we look for specific clues as to how the upper band dynamics affect our measurements.

In section 6.3 we looked at the dynamics of a $\boldsymbol{q} = 0$ ground state, but in this case we construct the momentum distribution of a gas with finite coherence length by thermally populating the Brillouin zone. Solving the band structure problem at each quasimomentum $\boldsymbol{q}$ tells us the momentum distribution at points $\boldsymbol{q} + \boldsymbol{G}_i$. We sum over the whole Brillouin zone, weighting the momentum distribution of each point by $e^{-E(\boldsymbol{q})/k_B T} / \sum_{\boldsymbol{q}} e^{-E(\boldsymbol{q})/k_B T}$

As before, we solve a second Hamiltonian with the phase imprint potential equation of 6.56. At each quasi-momentum we project the thermally populated eigenstates of the trimerized kagome lattice onto the eigenstates of the phase imprint potential. Each eigenstate evolves at its eigenenergy, and from these we construct the momentum distribution.

As can be seen in figure 6.20, evolution in the phase imprint potential evolves a symmetric potential into an asymmetric one. We see the oscillation of the nearest-neighbor coherence as before, but in addition we see the emergence of a high spatial frequency modulation in the momentum distribution not seen in the data. We believe structure in our images is likely caused by the rapid phase evolution of the higher band atoms. Certainly there is some upper band population, at $\boldsymbol{q} = 0$ this is 4%. In the experiment we would likely not see these higher band atoms, as they quickly relax back to the ground state via collisions.

We fit the generated images with the functional form given in equation 6.53. Whilst

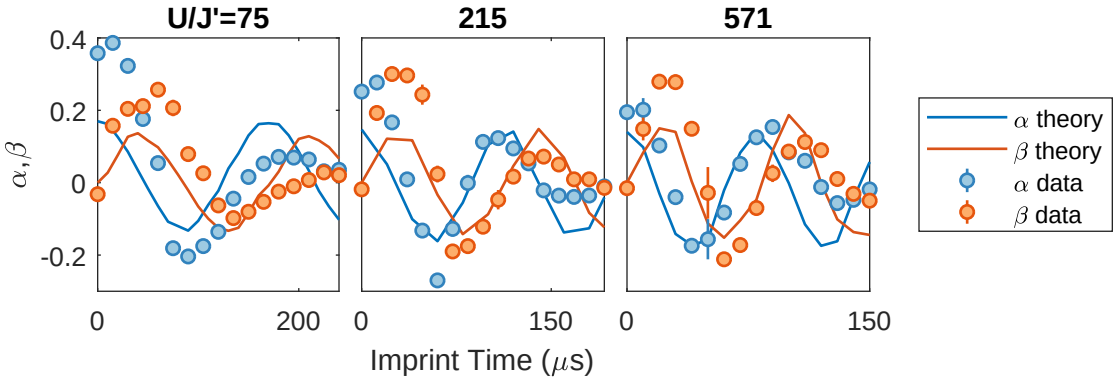

Figure 6.21: Comparison of the phase imprint data to a finite temperature band structure calculation. Coherences extracted from the theoretical momentum distributions are consistent in frequency and phase with experimental result, but show no damping. The theory does not reproduce the anomaly observed at short with where $\max(\beta) > \max(\alpha)$.

this modulation prevents us fitting the Gaussian width of these images, we believe it occurs at high enough spatial frequency not to affect our measurement of the nearest neighbor coherence.

In figure 6.21 we plot the extracted values of α_i, β_i and compare them to experiment. Whilst the results show some consistency with the oscillation frequency, they don't capture the features we are trying to understand .We do not see $\max(\beta)>\max(\alpha)$ at short time, and we do not see a decay in the oscillations, or α_2 . As a result, whilst we have some upper band population, we believe it is not important to understanding our data.

Chapter 7

Conclusion

Throughout this thesis we have shown how ultracold atoms in optical lattices make a quantum simulator for the Bose-Hubbard model, and we have performed experiments with this quantum simulator. Now we return to summarize the more significant contributions made by this thesis, and discuss their future exploration. We will summarize how effectively we stabilize the relative displacement of the optical superlattice, compare our results to our requirements, and consider improvements for the practical implementation of this system. We return to our discussion of the short range coherence of the Mott insulator in a triangular lattice, and the questions of global equilibrium. We will summarize what we know, and what is yet to be understood. We discuss the evidence we have for the fractional Mott insulating state, and what further measurements should be made to clearly show the existence of this state. Finally, we return to the many configurations of the optical superlattice and suggest further experiments.

7.1 Displacement stabilization

Our ability to simulate the Bose-Hubbard model on a large number of lattice structures is enabled by the system that stabilizes the relative displacement δ of the 532 nm and 1064 nm wavelength triangular lattices. For us to faithfully realize the ideal potentials described in section 2.3, we must control this relative displacement both in time, and across the entire spatial extent of the entire optical lattice. In this section we examine how well the displacement is controlled by summarizing the various estimates we have made of the displacement error.

Some of these effects are fast fluctuations in time, such as the displacement estimates from the error signals, or a slow drift in time caused by a drift of the laser frequency. Others are spatial variations of the displacement over the optical lattice such as that caused by the imperfect collinearity of 532 nm and 1064 nm wavevectors . We summarize all of these in table 7.1, and compare them to measurements taken before the redesign of the stabilization system, and to estimates of the required δ.

Cause of displacement	δ	Reference
Previous run-to-run fluctuation	20 nm	[39]
Previous variation over lattice due to wavelength	19, 9 nm	[39]
Variation over lattice due to rotation	1 nm	3.2
Variation over lattice due to wavelength	2 nm	3.2
Drift of 1064 nm wavelength in 1 hour	0.4 nm	4.1
Drift of 532 nm wavelength in 1 hour	3.5 nm	4.1
$1\,^{\circ}C$ change in air temperature	0.4 nm	4.1
0.1 kPa change in air pressure	5 nm	4.1
Estimation from 532 nm error signal	5 nm	4.6
Estimation from 1064 nm error signal	3 nm	4.6
Results from superfluid diffraction experiment	1.3 nm	4.6
Requirement for trimerized kagome lattice	< 1 nm	6.3
Requirement for kagome lattice	< 20 nm	[39]

Table 7.1: Comparison of various estimated and measured relative displacements δ.

It is clear our redesigned displacement stabilization scheme significantly improves on the previous scheme, described in Jennie Guzman's thesis [32]. This previous scheme relied on piezoelectric feedback to the displacements of mirrors. This older system would occasionally fail to keep the optical phase locked when the piezo hit the edge of its dynamic range. This failure mode is completely eliminated by switching to an optical frequency feedback scheme. Additionally we reduced the measured fluctuations of the displacement by a factor of 10, even as we added components with substantial optical phase noise such as independent optical fibers.

We estimated the required level of displacement for the trimerized kagome lattice as < 1 nm by requiring the energy shift between different sites to be less than the tunneling energy J. At $J = 250$ Hz this requires a < 1 nm displacement for $V_{1064} = 40$ kHz. These are representative numbers, but by no means the most challenging we deal with. Even then, our estimated or measured displacements shown in table 7.1 are almost all larger than this number. This agrees with our experience of needing to adjust the displacement control to counteract drifts every 20 minute, and we saw significant run to run variation.

The most substantial improvement to this apparatus is already underway. Zephy Leung, Masayuki Okano and Yee Ming Tso have built a system to double the 1064 nm light to produce the 532 nm light. The 532 nm wavelength drifts will be substantially improved, as they will inherit the slow drift rate of the Mephisto MOPA, but additionally the 532 nm and 1064 nm wavelength drifts will be correlated. Switching to doubled light will also remove a known frequency noise problem of the Verdi, which is responsible for the larger RMS displacement of the 532 nm light.

We also identify pressure changes as a large contributor to displacement drift. Whilst we do not measure the local barometric pressure near the optical lattice, changes of 1 mbar

are to be expected. Reducing the path length difference will reduce the sensitivity to to pressure changes, and it would be interesting to measure this local pressure to correlate it with observed drifts in the displacement.

Finally, the inhomogeneity of the displacement over the spatial extent of the lattice is significant. It would be useful to measure the tunneling in the lattice directly, perhaps by preparing atoms in a single site and then allowing evolution in three sites. The dephasing of the site occupation oscillations, such as seen in [20] would tell us the inhomogeneity of the lattice.

7.2 Large phase coherence in the triangular Mott insulator

In studying the phase coherence of a Mott integer on a triangular lattice, we observed an anomalously high nearest-neighbor coherence α. We implemented a curvature compensation technique that did mitigate some of the extra coherence we saw, but the mystery of high coherence is not fully resolved. We lack a predictive theoretical explanation for this anomalously large α, and we have not rigorously tested our expansion compensation scheme. We overview the evidence we do have, explore what has been observed in the literature, and suggest future measurements to investigate this phenomenon further.

Increasing the confining curvature of the gas as the lattice depth increases, thus keeping the nominal Thomas-Fermi radius constant, brings the measured coherence closer to its equilibrium value with little heating. However, we cannot confidently determine if our final measurements in figure 5.12 agree or disagree with equilibrium theory (equation 5.22). The uncertainty in the lattice depth is sufficiently large to plausibly explain the remaining discrepancy between theory and experiment. In chapter 3, we show how interaction effects may cause us to systematically overestimate the calibrated lattice depth, and an overestimated lattice depth results in a larger α than predicted. In other measurements we still see some dependence of α on time that we cannot explain, nor can we rule out heating. Additionally, we lack clear evidence from the density distribution itself that our expansion compensation scheme has been implemented correctly at all stages of the lattice loading sequence.

This erroneously high nearest-neighbor coherence has yet to be reported in the literature. In experiments in Munich, the density inferred from the visibility of a Mott insulator in a cubic lattice is systematically higher than the expected density, but not by the amount observed in our experiment [26]. In experiments in Maryland, the measured coherence α in a 2D square lattice agrees with that predicted by the density to within experimental error [60]. Both of these experiments take place in red-detuned optical lattices, for which the trapping potential automatically increases as the lattice depth increases. This extra curvature could play a similar role to our expansion compensation curvature. We do note the observation of long timescales for global density relaxation [36] and its potential explanation in terms of the formation of Mott domains [53]. Such an explanation may be relevant to our observations.

Currently we use finite temperature perturbation theory to connect the density to the coherence. Unfortunately the combination of this theory and the local density approximation do not provide us with an explanation of the anomalously higher coherence, nor its evolution in time. To understand this problem further, we both need a precise measurement of the density distribution, and a new theoretical model to explain how this density distribution leads to the high coherence. Thus any further work requires a high resolution image of the density distribution, and how it evolves in time. High resolution images would also permit proper testing of the curvature compensation scheme. It may also be interesting to take images of the gas at very short time of flight, where atoms in a given site only overlap with their nearest-neighboring site. Such a measurement would allow us to see where the coherence is developing spatially, which would be a good test for any theoretical models.

7.3 Fractional Mott insulator

In the chapter 6 we demonstrated a faithful experimental realization of the Bose-Hubbard model on a trimerized kagome lattice, and showed initial evidence for a fractional Mott insulating state. We demonstrated our ability to deterministically prepare each of the two trimerization pattern of this lattice, and developed a new atom-optics technique to determine the trimerization pattern. We calculated the Bose-Hubbard parameters for our particular implementation of this lattice and argued that we can satisfy the assumptions of the Bose-Hubbard model.

Our measurements of a persistent and asymmetric phase coherence deep in the Mott insulating phase provides initial evidence for the delocalized nature of this state. As the weak tunneling element J' was suppressed, the long range phase coherence diminished but the nearest-neighbor phase coherence persisted. We then developed a new technique to show the strong asymmetry of this coherence.

Our experiments were conducted at a relatively high central filling of 8 atoms per trimer in the center of the gas. The inhomogeneity of our confining potential means that our filling ranges from 8 atoms per trimer in the center to 1 atom per trimer at the edge of the gas. In the future it would be interesting to reduce the filling to at most 2 atoms per trimer, and study the loss of coherent fraction as the phase transition from superfluid to Mott insulator is crossed. Studying the position of the phase boundary as J/U is changed would confirm the phase diagrams in section 6.4.

Taking inspiration from studying a similar phase on a dimerized hexagonal lattice [42], we could also show the difference in the excitation spectrum between the fractional and the integer Mott insulating states. Amplitude modulation spectroscopy deep in the insulating phase of the integer Mott insulator shows the presence a particle-hole excitation at energy U, where as in the fractional state it would happen at largest $U/3$. Phase modulation spectroscopy would show the presence of rotational excitations within the plaquettes, at $3J$ for the $v = 1$ state.

7.4 Further experiments in triangular geometries

Finally we return to the eight lattice structures shown in section 2.3 to discuss possible future experiments.

Trimerized kagome lattice

The trimerized kagome lattice potential is shown in figure 2.7. In addition to further work on the fractional Mott insulating states, it would also be interesting to use the many tools developed in the community to prepare few body states in the triangular plaquettes. Preparing a few particles in the plaquette in rotating states, then slowly increasing the coupling between plaquettes J', could be a method to prepare atoms in the flat band of the trimerized kagome lattice.

Another exciting idea would be to follow the proposal of Damski et. al. [14] to add two spinless fermions to each trimer of the trimerized kagome lattice. They argue that this realizes an effective spin-$\frac{1}{2}$ model on the triangular lattice, which they suggest forms a quantum spin-liquid crystal; a state with a planar antiferromagnetic order and a very large numbers of low energy exciations.

Kagome lattice

The kagome lattice is shown in figure 2.4. Few exact results exist for the fermionic version of the Hubbard model, but one such result concerns the kagome lattice. Mielke [49] and Tasaki [65] showed that the exact ground state of the fermionic Hubbard model on the kagome lattices is ferromagnetic when the flat band if half filled. Furthermore, this result holds for a range of fillings and even under small perturbations to the flat band. As this ferromagnetism is driven by the direct overlap of the localized states of the flat band, it potentially could occur at significantly higher temperatures than those at which antiferromagnetism is currently observed in cold atom systems.

Hexagonal plaquette lattice

The lattice of hexagonal plaquettes, also known as the hexamerized honeycomb lattice and shown in figure 2.10, is formed by 532 nm and 1064 nm out-of-plane polarization. The hexagonal plaquette structure offers a range of interesting few body physics to explore. One such possibility would be to study resonant valence bond oscillations on precisely the benzene ring geometry on which they were originally proposed. This might be possible adapting techniques developed in Munich for the observation of RVB on square plaquettes [51].

Alternatively, the six sites can be deformed into a ring when the ratio V_{1064}/V_{532} is greater than 1. The potential barrier between nearest-neighbor sites decreases faster with V_{1064} than the potential barrier between opposite sites in a ring. This leaves a region where the

corrugation around the ring is small compared to the central potential, which approximates a ring. Atoms in a ring would have an angular momentum like structure, which may be interesting to study in the context of rotating gases and vortices.

Bibliography

[1] Mike H Anderson et al. "Observation of Bose-Einstein condensation in a dilute atomic vapor". In: *Science* 269.5221 (1995), pp. 198–201.

[2] Waseem S Bakr et al. "A quantum gas microscope for detecting single atoms in a Hubbard-regime optical lattice". In: *Nature* 462.7269 (2009), p. 74.

[3] John Bechhoefer. "Feedback for physicists: A tutorial essay on control". In: *Reviews of Modern Physics* 77.3 (2005), p. 783.

[4] Christoph Becker. "Multi-component quantum gases - From mean-field physics to strong correlations". PhD thesis. Universitat Hamburg, 2009.

[5] C Becker et al. "Ultracold quantum gases in triangular optical lattices". In: *New Journal of Physics* 12.6 (2010), p. 065025.

[6] KP Birch and MJ Downs. "An updated Edlén equation for the refractive index of air". In: *Metrologia* 30.3 (1993), p. 155.

[7] Immanuel Bloch, Jean Dalibard, and Sylvain Nascimbene. "Quantum simulations with ultracold quantum gases". In: *Nature Physics* 8.4 (2012), p. 267.

[8] Gretchen K Campbell et al. "Imaging the Mott insulator shells by using atomic clock shifts". In: *Science* 313.5787 (2006), pp. 649–652.

[9] Qi-Hui Chen, Peng Li, and Haibin Su. "Fractional Mott insulator-to-superfluid transition of Bose–Hubbard model in a trimerized Kagomé optical lattice". In: *Journal of Physics: Condensed Matter* 28.25 (2016), p. 256001.

[10] Lawrence W Cheuk et al. "Quantum-gas microscope for fermionic atoms". In: *Physical review letters* 114.19 (2015), p. 193001.

[11] Andrew John Daley. *Manipulation and simulation of cold atoms in optical lattices*. 2005.

[12] Franco Dalfovo et al. "Theory of Bose-Einstein condensation in trapped gases". In: *Reviews of Modern Physics* 71.3 (1999), p. 463.

[13] Jean Dalibard. "Collisional dynamics of ultra-cold atomic gases". In: *Proceedings of the International School of Physics-Enrico Fermi*. Vol. 321. 1999, p. 14.

[14] B Damski et al. "Quantum gases in trimerized kagomé lattices". In: *Physical Review A* 72.5 (2005), p. 053612.

[15] Peter Delos. "Phase locked loop noise transfer functions". In: *High Freq. Electron.* 15.3 (2016), p. 22.

[16] Stefan Depenbrock, Ian P McCulloch, and Ulrich Schollwöck. "Nature of the spin-liquid ground state of the S= 1/2 Heisenberg model on the kagome lattice". In: *Physical review letters* 109.6 (2012), p. 067201.

[17] M Egorov et al. "Measurement of s-wave scattering lengths in a two-component Bose-Einstein condensate". In: *Physical Review A* 87.5 (2013), p. 053614.

[18] Veit Elser. "Nuclear antiferromagnetism in a registered He 3 solid". In: *Physical review letters* 62.20 (1989), p. 2405.

[19] Richard P Feynman. "Simulating physics with computers". In: *International journal of theoretical physics* 21.6-7 (1982), pp. 467–488.

[20] Simon Fölling. "Probing strongly correlated states of ultracold atoms in optical lattices". PhD thesis. PhD thesis, Johannes Gutenberg-Universität, Mainz, Fachbereich 08: Physik ..., 2008.

[21] S Friebel et al. "CO 2-laser optical lattice with cold rubidium atoms". In: *Physical Review A* 57.1 (1998), R20.

[22] Floyd M Gardner. *Phaselock techniques*. John Wiley & Sons, 2005.

[23] Iulia M Georgescu, Sahel Ashhab, and Franco Nori. "Quantum simulation". In: *Reviews of Modern Physics* 86.1 (2014), p. 153.

[24] F Gerbier et al. "Expansion of a quantum gas released from an optical lattice". In: *Physical review letters* 101.15 (2008), p. 155303.

[25] Fabrice Gerbier et al. "Interference pattern and visibility of a Mott insulator". In: *Physical Review A* 72.5 (2005), p. 053606.

[26] Fabrice Gerbier et al. "Phase coherence of an atomic Mott insulator". In: *Physical Review Letters* 95.5 (2005), p. 050404.

[27] Tatjana Gericke et al. "Adiabatic loading of a Bose–Einstein condensate in a 3D optical lattice". In: *Journal of Modern Optics* 54.5 (2007), pp. 735–743.

[28] Markus Greiner. "Ultracold quantum gases in three-dimensional optical lattice potentials". PhD thesis. lmu, 2003.

[29] Markus Greiner et al. "Magnetic transport of trapped cold atoms over a large distance". In: *Physical Review A* 63.3 (2001), p. 031401.

[30] Markus Greiner et al. "Quantum phase transition from a superfluid to a Mott insulator in a gas of ultracold atoms". In: *nature* 415.6867 (2002), p. 39.

[31] Rudolf Grimm, Matthias Weidemüller, and Yurii B Ovchinnikov. "Optical dipole traps for neutral atoms". In: *Advances in atomic, molecular, and optical physics*. Vol. 42. Elsevier, 2000, pp. 95–170.

[32] Jennie Sara Guzman. "Explorations of Magnetic Phases in F= 1 87Rb Spinor Condensates". PhD thesis. UC Berkeley, 2012.

[33] DM Harber et al. "Effect of cold collisions on spin coherence and resonance shifts in a magnetically trapped ultracold gas". In: *Physical Review A* 66.5 (2002), p. 053616.

[34] John Hubbard. "Electron correlations in narrow energy bands". In: *Proceedings of the Royal Society of London. Series A, mathematical and physical sciences* (1963), pp. 238–257.

[35] Chen-Lung Hung et al. "Accelerating evaporative cooling of atoms into Bose-Einstein condensation in optical traps". In: *Physical Review A* 78.1 (2008), p. 011604.

[36] Chen-Lung Hung et al. "Slow mass transport and statistical evolution of an atomic gas across the superfluid–mott-insulator transition". In: *Physical Review Letters* 104.16 (2010), p. 160403.

[37] Cisco Global Cloud Index. "Forecast and methodology, 2016-2021 white paper". In: (2016).

[38] Dieter Jaksch et al. "Cold bosonic atoms in optical lattices". In: *Physical Review Letters* 81.15 (1998), p. 3108.

[39] Gyu-Boong Jo et al. "Ultracold atoms in a tunable optical kagome lattice". In: *Physical review letters* 108.4 (2012), p. 045305.

[40] T Johnson, S Clark, and G Cotugno. "Wannier states for optical lattices (2013)". In: *URL http://ccpforge. cse. rl. ac. uk/gf/project/mlgws* ().

[41] Robert Jördens et al. "A Mott insulator of fermionic atoms in an optical lattice". In: *Nature* 455.7210 (2008), p. 204.

[42] Ole Jürgensen and Dirk-Sören Lühmann. "Dimerized Mott insulators in hexagonal optical lattices". In: *New Journal of Physics* 16.9 (2014), p. 093023.

[43] VA Kashurnikov, NV Prokof'ev, and BV Svistunov. "Revealing the superfluid–Mott-insulator transition in an optical lattice". In: *Physical Review A* 66.3 (2002), p. 031601.

[44] Junru Li et al. "Spin-orbit coupling and spin textures in optical superlattices". In: *Physical review letters* 117.18 (2016), p. 185301.

[45] Tracy Li. "Probing Bloch band geometry with ultracold atoms in optical lattices". PhD thesis. Ludwig Maximilians Universität München, 2016.

[46] Y-J Lin et al. "Rapid production of an ^{87}Rb Bose-Einstein condensates in a combined magnetic and optical potential". In: *Physical Review A* 79.6 (2009), p. 063631.

[47] Th A Maier et al. "Systematic study of d-wave superconductivity in the 2d repulsive hubbard model". In: *Physical review letters* 95.23 (2005), p. 237001.

[48] George Edward Marti. "Scalar and Spinor Excitations in a Ferromagnetic Bose-Einstein Condensate". PhD thesis. UC Berkeley, 2014.

[49] Andreas Mielke. "Ferromagnetic ground states for the Hubbard model on line graphs". In: *Journal of Physics A: Mathematical and General* 24.2 (1991), p. L73.

[50] Frederic Mila. "Low-energy sector of the S= 1/2 Kagome antiferromagnet". In: *Physical review letters* 81.11 (1998), p. 2356.

[51] Sylvain Nascimbène et al. "Experimental realization of plaquette resonating valence-bond states with ultracold atoms in optical superlattices". In: *Physical review letters* 108.20 (2012), p. 205301.

[52] Garth Nash. "Phase-locked loop design fundamentals". In: *New York* (1994).

[53] Stefan S Natu, Kaden RA Hazzard, and Erich J Mueller. "Local versus global equilibration near the bosonic Mott-insulator–superfluid transition". In: *Physical review letters* 106.12 (2011), p. 125301.

[54] Wolfgang Petrich et al. "Behavior of atoms in a compressed magneto-optical trap". In: *JOSA B* 11.8 (1994), pp. 1332–1335.

[55] William D Phillips and Harold Metcalf. "Laser deceleration of an atomic beam". In: *Physical Review Letters* 48.9 (1982), p. 596.

[56] AP Ramirez. "Strongly geometrically frustrated magnets". In: *Annual Review of Materials Science* 24.1 (1994), pp. 453–480.

[57] Jan N Reimers and AJ Berlinsky. "Order by disorder in the classical Heisenberg kagomé antiferromagnet". In: *Physical Review B* 48.13 (1993), p. 9539.

[58] Subir Sachdev. "Kagomé-and triangular-lattice Heisenberg antiferromagnets: Ordering from quantum fluctuations and quantum-disordered ground states with unconfined bosonic spinons". In: *Physical Review B* 45.21 (1992), p. 12377.

[59] Robert Schaffer et al. "Quantum spin liquid in a breathing kagome lattice". In: *Physical Review B* 95.5 (2017), p. 054410.

[60] Ian B Spielman, William D Phillips, and James V Porto. "Mott-insulator transition in a two-dimensional atomic bose gas". In: *Physical Review Letters* 98.8 (2007), p. 080404.

[61] National Institute of Standards and Technology. *Refractive index of air calculator*. 2000. URL: `https://emtoolbox.nist.gov/Wavelength/Edlen.asp` (visited on 12/08/2018).

[62] Daniel A Steck. *Rubidium 87 D line data*. 2001.

[63] Minoru Takahashi. "Half-filled Hubbard model at low temperature". In: *Journal of Physics C: Solid State Physics* 10.8 (1977), p. 1289.

[64] H Tasaki. "Hubbard model and the origin of ferromagnetism". In: *The European Physical Journal B* 64.3-4 (2008), pp. 365–372.

[65] Hal Tasaki. "From Nagaoka's ferromagnetism to flat-band ferromagnetism and beyond: An introduction to ferromagnetism in the Hubbard model". In: *Progress of Theoretical Physics* 99.4 (1998), pp. 489–548.

[66] Claire K Thomas. "Quantum Simulation of Triangular, Honeycomb and Kagome Crystal Structures using Ultracold Atoms in Lattices of Laser Light". PhD thesis. UC Berkeley, 2017.

[67] Claire K Thomas et al. "Mean-field scaling of the superfluid to Mott insulator transition in a 2D optical superlattice". In: *Physical review letters* 119.10 (2017), p. 100402.

[68] Claire K Thomas et al. "Signatures of spatial inversion asymmetry of an optical lattice observed in matter-wave diffraction". In: *Physical Review A* 93.6 (2016), p. 063613.

[69] E Toth and PB Blakie. "Thermally induced coherence in a Mott insulator of bosonic atoms". In: *Physical Review A* 83.2 (2011), p. 021601.

[70] CG Townsend et al. "Phase-space density in the magneto-optical trap". In: *Physical Review A* 52.2 (1995), p. 1423.

[71] Stefan Trotzky et al. "Controlling and detecting spin correlations of ultracold atoms in optical lattices". In: *Physical Review Letters* 105.26 (2010), p. 265303.

[72] Stefan Trotzky et al. "Time-resolved observation and control of superexchange interactions with ultracold atoms in optical lattices". In: *Science* 319.5861 (2008), pp. 295–299.

[73] D Van Oosten, Peter van der Straten, and HTC Stoof. "Quantum phases in an optical lattice". In: *Physical Review A* 63.5 (2001), p. 053601.

[74] G Vandegrift. "Accelerating wave packet solution to Schrödinger's equation". In: *American Journal of Physics* 68.6 (2000), pp. 576–577.

[75] R Walters et al. "Ab initio derivation of Hubbard models for cold atoms in optical lattices". In: *Physical Review A* 87.4 (2013), p. 043613.

[76] John Weiner et al. "Experiments and theory in cold and ultracold collisions". In: *Reviews of Modern Physics* 71.1 (1999), p. 1.

[77] Stefan Wessel et al. "Quantum monte carlo simulations of confined bosonic atoms in optical lattices". In: *Physical Review A* 70.5 (2004), p. 053615.